

Nottingham Geospatial Institute

Validation of the Intermittent SBAS (ISBAS) DInSAR algorithm over the gas reservoirs of North Holland, The Netherlands

By

David Gee BSc (Hons.)

Thesis submitted to the University of Nottingham for the degree of Masters of Science by Research

September 2015

Abstract

Ground motion as a consequence of natural geological processes or due to anthropogenic influences, is a considerable problem and concern to a variety of people and groups. These include the mining industry, insurance companies, government and not least the general population. Increased knowledge of subsidence patterns would benefit all parties involved; however, often techniques used such as levelling and GPS have spatial or temporal shortfalls. Utilizing remotely sensed data and Differential Interferometric Synthetic Aperture Radar (DInSAR), the shortcomings of traditional measurement can be overcome, producing precise maps over wide expanses and over many years. DInSAR utilizes stacks of Synthetic Aperture Radar (SAR) imagery of the same area to derive ground motion rates with millimetric precision. A significant limitation of these techniques, be it utilizing small baseline or persistent scatterer methods, is the density of coverage it can achieve over dynamic rural environments. Interferometric analysis is not possible over large sections of the scene which can inhibit the identification of subsidence patterns, impeding the techniques efficacy. The Intermittent Small Baseline Subset (ISBAS) is an improved version of the established SBAS algorithm, designed to improve coverage over rural settings by considering intermittent coherence. 52 ERS-2 (SAR) C-band images (1995-2000) and 75 ENVISAT (ASAR) C-band images (2003-2010) of North Holland were processed using the ISBAS technique. Up to 15 times as many point velocities were returned than when using the conventional SBAS analysis. The measurement of linear velocities in rural areas enabled a more complete identification subsidence, offering an improvement over the original SBAS technique. The dominant feature was an area of subsidence in the area to the West of Alkmaar, attributed to natural gas production with subsidence rates in the region of 3 mm/year. Linear displacement velocities were validated with respect to the first order system of levelling benchmarks which form the Dutch ordinance level. It established that ISBAS products were accurate to within 1.29 mm/year and 1.42 mm/year for the ERS and ENVISAT data sets respectively. These error budgets were comparable to results found in the Terrafirma validation project, where the same site was studied using conventional persistent scatterer approaches.

Acknowledgements

I would like to thank my supervisor Dr Andrew Sowter for his guidance, help and problem solving abilities throughout the project, as well as Dr Doreen Boyd and Dr Jeremy Morley for their support in the process. I would also like to thank my parents, John and Louise, who have made the last year possible and supported me throughout the last five years at university.

Contents List

Acronyms and Abbreviations ..... **xii**

1 Introduction **1**

1.1 Background 1

1.2 Land Movement in the Netherlands 1

1.3 Natural Gas 3

1.4 Detection and Measurement of Subsidence 5

1.5 Aim and Objectives 6

1.6 Thesis Overview 6

1.7 Summary 7

2 Literature Review **8**

2.1 Remote Sensing 8

2.2 Radio Detection And Ranging (Radar) 8

2.2.1 History 9

2.2.2 Side Looking Airborne Radar (SLAR) 9

2.3 Synthetic Aperture Radar (SAR) 10

2.3.1 Coherent Imaging 11

2.3.2 Electromagnetic Wave Properties 12

2.3.3 Wavelength 13

2.3.4 Polarization 14

2.3.5 Imaging Geometry 15

2.3.6 Resolution 16

2.3.7 Range 17

2.3.8 Azimuth 17

2.3.9 SAR Image Properties 18

2.3.10 Geometric Distortion 19

2.3.10.1 Foreshortening 19
2.3.10.2 Layover 20
2.3.10.3 Shadow 20
2.3.11 Image Speckle 21
2.3.12 Satellites 21
2.3.12.1 ERS 21
2.3.12.2 ENVISAT 22
2.3.12.3 Sentinel-1 22
2.4 Interferometric Synthetic Aperture Radar (InSAR) 23
2.4.1 Interferometry 23
2.4.2 Interferometric Phase 24
2.4.3 Configurations 26
2.4.3.1 Single-Pass 26
2.4.3.2 Repeat-Pass 26
2.4.4 Repeat-Pass Geometry 27
2.4.5 Limitations of InSAR 28
2.4.5.1 Data Availability 28
2.4.5.2 Noise Effects 29
2.4.5.3 Orbital Inaccuracies 30
2.4.5.4 Atmospheric Effects 30
2.5 Differential Interferometric Synthetic Aperture Radar 30
2.5.1 DInSAR Limitations 31
2.5.1.1 Double Differencing 31
2.5.1.2 Atmospheric Artefacts 31
2.5.1.3 Phase Unwrapping 32
2.5.2 DInSAR Philosophies 33
2.5.2.1 Persistent Scatterer 33
2.5.2.2 Small Baseline 34
2.6 Small Baseline Subset (SBAS) 35

2.6.1 Methodology 36
2.7 Intermittent Small Baseline Subset (ISBAS) 37
2.7.1 Methodology 37
2.8 Research Motivations 38
2.8.1 ISBAS Proficiency 38
2.8.2 Terrafirma Validation Project 39
2.9 Summary 40
3 North Holland 41
3.1 Geography 41
3.2 Land Cover 41
3.3 Geological Setting 43
3.4 Gas Production 44
3.5 Subsidence 46
3.5.1 Reservoir Compaction 46
3.6 Induced Seismicity 48
3.6.1 Fluid Injection 49
3.6.2 Fluid Extraction 51
3.6.3 Fault Reactivation 51
3.7 Seismic Events in North Holland 52
3.7.1 Bergermeer 53
3.7.1.1 Reservoir Geology 54
3.7.1.2 Earthquake Focal Mechanism 55
3.7.1.3 Underground Storage Facility 57
3.7.2 Bergen 58
3.8 Summary 58
4 Processing Requisites 59
4.1 Data Sources 59
4.1.1 SAR 59
4.1.2 DEM 59

4.1.3 Shapefiles 59
4.1.4 Geodetic Levelling 59
4.2 Software 60
4.2.1 Punnet 60
4.2.2 ArcGIS 61
4.3 Summary 61
5 SAR Analysis 62
5.1 Interferogram Processing Flow 62
5.1.1 SLC Data 62
5.1.2 Coregistration 62
5.1.3 Resampling and Interpolation 62
5.1.4 Interferogram Generation 62
5.1.5 Multilooking 63
5.1.6 Coherence 64
5.1.7 Filtering 65
5.2 ERS 65
5.2.1 Processing 65
5.2.2 Results 67
5.3 ENVISAT 71
5.3.1 Processing 71
5.3.2 Results 73
5.4 Sentinel 78
5.4.1 Processing 78
5.4.2 Results 80
5.5 Summary 81
6 Product Validation 82
6.1 Levelling Benchmarks 82
6.1.1 ERS 83
6.1.2 ENVISAT 84

6.2 Spatial Validation - Kriging 85
6.3 Measurement Validation - Linear Displacement Velocities 88
6.3.1 ERS 88
6.3.2 ENVISAT 90
6.3.3 Point Quality Correlations 92
6.4 Comparisons with the Terrafirma Validation Project 94
6.4.1 Subsidence Patterns 95
6.4.2 Linear Displacement Velocities 96
6.4.3 Displacement Time Series 97
6.5 Summary 99
7 Discussion 100
7.1 DInSAR Performance 100
7.1.1 SBAS 100
7.1.2 ISBAS 100
7.2 Limitations 102
7.2.1 SAR Data Continuity 102
7.2.2 Reference Data 102
7.2.3 Limited Deformation 104
7.3 Recommendations for Further Research 105
7.3.1 Rural ISBAS Validation 105
7.3.2 Sentinel-1 Time Series 105
7.4 Summary 106
8 Conclusions 107
8.1 Review of Aim and Objectives 107
8.1.1 North Holland 107
8.1.2 ISBAS Analysis 107
8.1.3 Product Validation 108
8.1.4 Comparisons with the Terrafirma Validation Project 108
8.1.5 Limitations and Further Research 108

8.2 Outlook 108
8.3 Summary 109
References 110

List of Figures

Figure 1.1: Subsidence evident in North Holland 2
Figure 1.2: Natural gas well categories 4
Figure 2.1: Relationship between real and synthetic aperture radar 11
Figure 2.2: Properties of an electromagnetic wave 12
Figure 2.3: The electromagnetic spectrum 13
Figure 2.4: Linearly polarized radiation 15
Figure 2.5: Imaging geometry of a SAR acquisition 16
Figure 2.6: Argand diagram of a SLC pixel 18
Figure 2.7: Foreshortening 19
Figure 2.8: Layover 20
Figure 2.9: Shadow 20
Figure 2.10: Constructive and destructive interference 24
Figure 2.11: Phase difference between sin (x) and sin (x + π/2) 25
Figure 2.12: Repeat-pass geometry. 28
Figure 2.13: Relationship between modulo phase and absolute phase 32
Figure 2.14: Block diagram of the SBAS algorithm 36
Figure 3.1: The Netherlands and North Holland province 41
Figure 3.2: Land cover classification of North Holland 42
Figure 3.3: Geological time scale of the Netherlands and Continental Shelf 43
Figure 3.4: Location and status of reservoirs in the North Holland 44
Figure 3.5: Induced seismicity along a normal fault 50
Figure 3.6: Mohr diagram for a fault plane 50
Figure 3.7: The epicentre locations of the five earthquakes in North Holland 52
Figure 3.8: Overview of damage reports following the September 2001 earthquakes 53
Figure 3.9: A SW-NE geological cross section of the Bergermeer reservoir 54
Figure 3.10: A schematic representation of the Bergermeer central reservoir fault 56
Figure 4.1: Locations of the zonal divisions of levelling benchmarks. 60
Figure 5.1: Interferogram of North Holland 63
Figure 5.2: Coherence and Amplitude images of North Holland 64
Figure 5.3: Temporal and perpendicular baselines of the ERS-2 SAR image pairs 66
Figure 5.4: Land cover and SBAS point velocities from ERS-2 time series. 68
Figure 5.5: ISBAS and SBAS vertical velocities from ERS-2 time series 69
Figure 5.6: Coherent pixels per point and standard deviation of velocities (ERS) 69
Figure 5.7: ISBAS and SBAS velocities around the Bergen region (ERS) 70

Figure 5.8: Temporal and perpendicular baselines of the ENVISAT ASAR image pairs..73
Figure 5.9: Land cover and SBAS point velocities from ENVISAT time series.....74
Figure 5.10: ISBAS and SBAS vertical velocities from ENVISAT time series 75
Figure 5.11: Coherent pixels per point and standard deviation of velocities (ENVISAT)..75
Figure 5.12: ISBAS and SBAS velocities around the Bergen region (ENVISAT).....76
Figure 5.13: Time series of five selected ENVISAT ISBAS non-linear points 78
Figure 5.14: Locations of the five selected ENVISAT ISBAS non-linear points.....77
Figure 5.15: Temporal and perpendicular baselines of the Sentinel-1 SAR image pairs. 79
Figure 5.16: Two Sentinel-1 interferograms of North Holland.....80
Figure 6.1: The linear displacement model estimated for Benchmark ID:019A0137.....82
Figure 6.2: Linear velocities from levelling benchmarks (ERS).....83
Figure 6.3: Linear velocities from levelling benchmarks (ENVISAT).....84
Figure 6.4: A comparison of kriging and ISBAS analysis (ERS) 86
Figure 6.5: A comparison of kriging and ISBAS analysis (ENVISAT). 87
Figure 6.6: Scatter plot of ERS ISBAS/SBAS and levelling velocities.....88
Figure 6.7: ERS ISBAS and levelling velocities.....89
Figure 6.8: ERS SBAS and levelling velocities.....89
Figure 6.9: Scatter plot of ENVISAT ISBAS/SBAS and levelling velocities.....90
Figure 6.10: ENVISAT ISBAS and levelling velocities.....91
Figure 6.11: ENVISAT SBAS and levelling velocities.....91
Figure 6.12: Correlation between m_{ij} and the RMSE (ERS).....93
Figure 6.13: Correlation between m_{ij} and the RMSE (ENVISAT).....93
Figure 6.14: Comparison of ERS ISBAS/SBAS and TVP PSI results.....95
Figure 6.15: Comparison of ENVISAT ISBAS/SBAS and TVP PSI results.....96
Figure 6.16: ERS displacement time series published in TVP.....97
Figure 6.17: ERS ISBAS time series for points near to Benchmark 019A0115.....98
Figure 7.1: Ground movement of the Netherlands 103
Figure 7.2: The distribution of settlement prone locations in the Netherlands.....104

List of Tables

Table 2.1: Radar band designations....14
Table 3.1: Gas reservoirs in North Holland....45
Table 3.2: Seismic events in North Holland....52
Table 3.3: Geological units of the Bergermeer reservoir....55
Table 5.1: ERS-2 SAR image dates and perpendicular baselines B⊥ (m)....66
Table 5.2: ENVISAT ASAR image dates and perpendicular baselines B⊥ (m)....72
Table 5.3: Sentinel-1a SAR image dates and perpendicular baselines B⊥ (m)....79
Table 6.1: Levelling campaigns in the ERS validation with over 200 benchmarks....83
Table 6.2: Levelling campaigns in the ENVISAT validation with over 200 benchmarks. ..84
Table 6.3: A comparison between kriging and ISBAS analyses....85
Table 6.4: A summary of the RMSE between SAR and levelling....92
Table 6.5: RMSE between ISBAS-levelling based on coherent layers....92
Table 6.6: Correlation between land cover and the RMSE....94
Table 6.7: A comparison of ISBAS and PSI from the TVP....97

Acronyms and Abbreviations

Almaz-1	Russian radar satellite
ALOS	Advanced Land Observation Satellite
AMI	Active Microwave Instrumentation
AOI	Area of Interest
ASAR	Advanced Synthetic Aperture Radar
BBL	Balgzand Bacton Line
CGIAR-CSI	Consultative Group for International Agricultural Research – Consortium for Spatial Information
DEM	Digital Elevation Model
DInSAR	Differential Interferometric Synthetic Aperture Radar
EC	European Commission
ENVISAT	Environmental Satellite
EO	Earth Observation
ERS	European Remote Sensing Satellite
ESA	European Space Agency
Esri	Environmental Systems Research Institute
ETM+	Enhanced Thematic Mapper Plus
FM	Frequency Modulated
GIS	Geographic Information Systems
GMES	Global Monitoring for Environment and Security
GPS	Global Positioning Systems
InSAR	Interferometric Synthetic Aperture Radar
IPTA	Interferometric Point Target Analysis
ISBAS	Intermittent Small Baseline Subset
JERS-1	Japanese Earth Resources Satellite
KMNI	Royal Netherlands Meteorological Institute
Landsat	NASA's EO program
LOS	Line of Sight
MERIS	Medium Resolution Imaging Spectrometer
MIT	Massachusetts Institute of Technology
MODIS	Moderate Resolution Imaging Spectroradiometer
NASA	National Aeronautics and Space Administration
NLOG	Netherlands Oil and Gas Portal

OSP	Operational Service Provider
PALSAR	Phased Array Type L-band Synthetic Aperture Radar
PPI	Plan Position Indicator
PS	Persistent Scatterer
PSI	Persistent Scatterer Interferometry
PVW	Product Validation Workgroup
Radar	Radio Detection And Ranging
Radarsat-1	Canadian radar satellite
RMSE	Root Mean Square Error
SAR	Synthetic Aperture Radar
SB	Small Baseline
SBAS	Small Baseline Subset
SDFP	Slowly-Decorrelating Filtered Phase
Sentinel-1	ESA radar satellite
SLAR	Side Looking Airborne Radar
SLC	Single Look Complex
SNAPHU	Statistical-Cost, Network-Flow Algorithm for Phase Unwrapping
STRM	Shuttle Radar Topography Mission
STUN	Spatio-Temporal Unwrapping Network
TNO	Netherlands Organisation for Applied Scientific Research
TOPSAR	Topographic Synthetic Aperture Radar
TVP	Terrafirma Validation Project
UGS	Underground Gas Storage
WGS	World Geodetic System

1 Introduction

1.1 Background

The monitoring of mining induced subsidence is vital for hazard and geological analysis, especially as populations continue to rise and urban regions expand into areas of increased potential natural and anthropogenic hazards (Bamler & Hartl, 1998). Europe, along with many other regions of the world, has been affected by subsidence (or uplift) due to the extraction of oil, salt, water, gas or other mineral resources. The recovery of hydrocarbons has resulted in underground reservoir compaction, induced seismicity and surface subsidence in the Netherlands. The exploitation of large on-land reservoirs has meant that Dutch law now requires a risk estimate and seismic hazard study for every concession. Mining legislation was introduced in 2002 (Staatsblad 542, 2002) whereby approval for exploitation licences requires risk / hazard analysis along with a strategy to detect earth movements because of increases in observed subsidence and induced seismicity (van Eck *et al.,* 2006). This is an expensive process and therefore tools and practices that can influence decision making are in ever increasing demand. Traditional surveying techniques are useful although they are constrained by the limited coverage they can provide. With the emergence of Interferometric Synthetic Aperture Radar (InSAR), it has been demonstrated that the technique has the capability to generate large scale surface deformation maps on a much denser spatial grid than traditional surveying techniques. In addition it is less restricted by personnel, field reconnaissance or geographic factors and can therefore produce deformation maps at a relatively cheap cost; however, it is not without its limitations.

1.2 Land Movement in the Netherlands

Surface subsidence has significant social ramifications because of the associated risks that damage to infrastructure and buildings can create (Figure 1.1). It is approximated that subsidence in the Netherlands costs every resident €250 extra per year for the maintenance of housing and infrastructure. Infrastructure is the most significantly affected, this is because the land subsides but the structures constructed on foundations do not. Over time this produces huge levels of damage above the surface to roads, buildings, fencing and pavements, and below the surface to gas pipelines, underground electricity networks and sewers (Deltrares, 2015).



Figure 1.1: *Subsidence evident in buildings in North Holland (Chisholm, 2015).*

In addition the Netherlands is a country heavily protected by Dykes, 60% of the country is below sea level and therefore land subsidence is particularly significant and of great concern to the populace as it increases the risk of flooding, in addition to creating implications for groundwater management (Bremmer *et al.,* 2003). These concerns are amplified by a variety of factors such as sea level rise, urbanization, the intensification of subsurface use and an increase in intensive rainstorms. Consequentially, subsidence in the order of centimetres, or even millimetres, can have destructive social, environmental and economic ramifications (Nagel, 2001).

In a modern age of heightened environmental awareness, quantifying movement is at the vanguard of planning and risk mitigation. Insurance companies, developers, planners, government and oil & gas companies will all benefit from more accurate quantifications of movements and a better understanding of their underlying causes. The impacts of subsidence in the Netherlands are not just correlated with the magnitude of the surface motion, but are most often of concern when it impacts on a person's safety or it causes a detrimental monetary consequence. It is not uncommon for ground motion to go

undetected and only come to the attention of engineers and planners when it is manifest in structural damage at the surface, which can range from minor to catastrophic. Of interest to the scientific community, amongst others, is discerning and monitoring the temporal evolution of detected deformations (Berardino *et al.,* 2002). New techniques and better methods of detection and measurement are therefore invaluable to engineers and planners.

1.3 Natural Gas

Natural gas, a subcategory of petroleum, is a naturally occurring complex mixture of hydrocarbons that contains a minor quantity of inorganic compounds. It is universally recognised by chemists and geologists that petroleum is derived from animal and plant remains that accrue on lake or sea floors alongside sediments that comprise sedimentary rocks. The procedure by which parent organic material is altered into petroleum is not fully understood but contributing factors are believed to be: the shearing pressure during compaction, heating and natural distillation at depth; bacterial action; the presence of catalysts; the potential introduction of hydrogen from deep-seated sources; and time (Allison & Palmer, 1980). Natural gas accumulates in geological traps called reservoirs, a permeable and porous underground formation encompassing an individual bank of hydrocarbons surrounded by water barriers or impermeable rock, that are characterised by a single natural pressure system. A field is where a group of more than one reservoir exists which are all related to the same structural feature (Guo & Ghalambor, 2014).

Natural gas in its raw form it comes from one of three varieties of wells: crude oil wells; condensate wells and gas wells (Figure 1.2). Associated gas is the term given to gas extracted from crude oil wells, where it can exist in the formation in a gas cap directly above the crude oil (free gas) or dissolved in the crude oil (dissolved gas). Non-associated gas originates from condensate wells or gas wells where there is no (or minimal) crude oil. Condensate wells produce free natural gas, together with a semi-liquid hydrocarbon condensate, while gas wells, such as those in North Holland, produce only natural gas. Natural gas that arrives at the well head is primarily composed of methane, although processing is required before transportation to separate it from other hydrocarbons such as butane, propane, ethane and pentanes; and compounds such as carbon dioxide, water vapour, nitrogen, helium and hydrogen sulphide (NaturalGas.org, 2013).

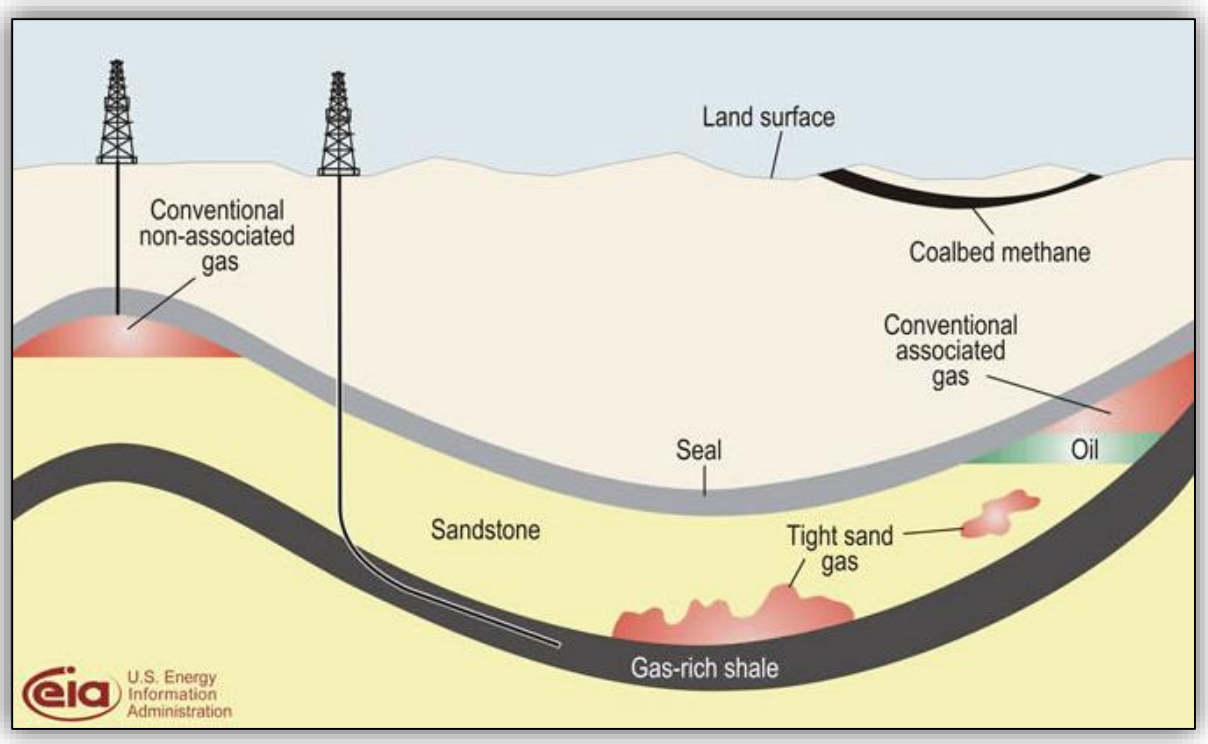


Figure 1.2: *Natural gas well categories (U.S. Energy Information Administration, 2015).*

During the primary recovery of natural gas, a borehole is drilled kilometres underground, which is subsequently encased in cement. When it reaches the targeted gas reservoir the pipe is perforated. Since sub-surface reservoirs exist at depths kilometres below the surface, they are subject to high geostatic pressures. As a result, when the pipe is perforated the natural pressurization of the reservoir causes the gas to flow upwards towards the surface from high to low pressure. Production can continue until the naturally occurring pressurization is effectively exhausted. At this point the well becomes uneconomical and the reservoir can be termed depleted. Secondary recovery is a term given to a collection of techniques aimed at extracting hydrocarbons from reservoirs where the natural pressurization has been exhausted. This can be achieved by injecting a fluid (i.e. a gas or liquid) into the subsurface to re-pressurize the reservoir. Pressurized fluids enter the reservoir via an injection well, which displace and in turn drive gas towards producing wells. Intelligent positioning of injection wells can help to further increase the yield and capacity of the reservoir (Talwani *et al.,* 2002).

Natural gas is the cleanest fossil fuel available, superior to coal and oil, both in economic attractiveness and environmental concerns. It is well acknowledged that the nineteenth century was driven by coal which provided the platform for the European industrial revolution; while the twentieth century was propelled by oil that drove the growth of the global economy. With the ever increasing demand of the world's economy for energy, it is

important to move towards sustainable methods of energy production, from oil, to gas, and eventually to hydrogen. Natural gas surpassed coal as the number two energy source behind oil at the latter end of the last century. Moving forward through the 21st century it is plausible that natural gas production could overtake oil production as the primary source of energy, stirred not only by environmental concerns but technological innovations and refinements (Economides *et al.,* 2002).

The Netherlands has a vast reserve of hydrocarbons; the discovered natural gas resources of the Netherlands are estimated to be 1130 billion Sm^3, with the total output production from onshore gas fields measuring 59.3 billion Sm^3 in 2012 (TNO, 2012). Consequently, exploration and extraction is on the increase with new gas fields being exploited (Guo & Ghalambor, 2014). Additionally, a common and strategic practice in many areas of the globe, including the Netherlands, is the use of depleted hydrocarbon reservoirs for underground gas storage (UGS). The interest surrounding the implementation of the practise is continuing to increase worldwide because of the significance of natural gas for energy production. UGS is conventionally used to ensure a smooth distribution from reservoirs to match the gas consumption pattern governed by both daily and seasonal fluctuations. Techniques to help monitor activity and consequent environmental impacts resultant from gas production, such as subsidence and induced seismicity, are therefore becoming ever increasingly more necessary.

1.4 Detection and Measurement of Subsidence

The four most prevalent techniques to estimate surface displacements over a time period are via Global Positioning Systems (GPS) surveys, optical levelling instruments, tiltmeter based surface deformation monitoring and Interferometric Synthetic Aperture Radar (InSAR). Synthetic Aperture Radar (SAR) was proven to accurately and reliably map the earth's surface in the late 1970s. Information could be deduced about earth surface properties including morphology, roughness and topography. Since the initial surveillance of ground movements over agricultural fields (Gabriel *et al.,* 1989) a plethora of Differential Interferometric Synthetic Aperture Radar (DInSAR) applications have been developed, with accuracies on the order of millimetres (Hanssen, 2001). DInSAR is a technique that has widely been applied to many areas of the globe, mapping deformation time series following the temporal and spatial evolution of deformation phenomena by employing advanced techniques such as the Small Baseline Subset (SBAS) (Berardino *et al.,* 2002). The feasibility of DInSAR detecting these events depends on a number of

factors including the deformation gradient, in combination with the effect of atmospheric signal within the interferograms and the influence of decorrelation (Hanssen, 2001). The implementation of DInSAR for subsidence monitoring is set to continue to rise as the number of operational SAR sensors increases, allowing swift data acquisition over large expanses of the earth's surface. In tandem innovative InSAR techniques are continuing to develop, with new algorithms emerging, such as the Intermittent SBAS (ISBAS) (Sowter *et al.,* 2013).

1.5 Aim and Objectives

Aim

- To provide a quantitative validation of the Intermittent SBAS algorithm.

Objectives

- Identify a suitable study site that has been subjected to ground motion where SAR and validation data are available.
- Use Punnet to process data sets, computing linear velocity deformation maps.
- Compare the point densities of SBAS and ISBAS products.
- Validate ISBAS products with levelling benchmarks.
- Test conclusions and compare the results to published literature.
- Explore the limitations of the project and suggest areas for further research.

1.6 Thesis Overview

This thesis is organized into eight chapters. Following the opening chapter, chapter 2 describes the fundamental philosophies and techniques that are applicable to this thesis. The literature review starts with a brief introduction to remote sensing, followed by an overview of the foundational developments of Radio Detection And Ranging (Radar) and Side Looking Airborne Radar (SLAR). This leads into a discussion of the pertinent concepts of SAR, which logically progress to an overview of InSAR and DInSAR. A detailed description of the Small Baseline Subset (SBAS) and Intermittent Small Baseline Subset (ISBAS) is then provided and the chapter concludes by identifying a research gap that would benefit from further investigation. Chapter 3 introduces the study site providing justification as to why it was chosen; this includes background on the geography, land cover, geology, and gas production. Geohazards anticipated to cause ground movement are identified, with the mechanisms communicated in detail. Chapter 4 outlines the

processing underpinning the study, detailing what data was required, where those data were sourced and what software was used in the course of processing. Chapter 5 details the process and results of the SAR analysis. It starts with an archetypal interferogram formation flow, which is followed by the specifics from the ERS, ENVISAT and Sentinel processing. Comparisons are made between the coverage of ISBAS and SBAS products and areas of ground motion are identified. Chapter 6 starts with a description of the composition of levelling benchmarks and a validation of ISBAS products follows. An initial exploratory spatial comparison is followed by a quantitative validation of linear displacement velocities. The performance of ISBAS products is then compared with PSI products from the Terrafirma Validation Project. Chapter 7 provides a discussion on all aspects of the study. Products are scrutinised and reflective comment is given on the limitations of the study. Additionally, recommendations for future research are established. Chapter 8 concludes the thesis by exploring what has been achieved. A short summary of each aim and objective is given, specifying how and to what extent they have been realised.

1.7 Summary

This opening chapter has delivered a contextual background to the significance of monitoring land motion associated with gas production. The process of natural gas extraction has been explained and benefits of using remote measurement and DInSAR to monitor the consequences of production have been introduced. It finishes with an overview of the thesis, with a description of every chapter in turn.

2 Literature Review

2.1 Remote Sensing

"The science of remote sensing comprises the analysis and interpretation of measurements of electromagnetic radiation that is reflected from or emitted by a target and observed or recorded from a vantage point by an observer or instrument that is not in contact with the target." (Mather, 2004).

Scientific information used to capture and delineate the earth can contribute to reducing the loss of property and life during disasters, managing resources and amplify our quality of life (U.S. Geological Survey, 2013). There has been significant progress in the development of innovative and pioneering applications of Earth Observation (EO) technology and data in recent years, primarily in Europe due to research initiatives funded by the European Space Agency (ESA), the European Commission (EC) and independent national agencies (Del Ventisette *et al.,* 2013). The development and progress of remote sensing, satellites and GIS enables efficient mapping, achievable at relatively low costs. Furthermore, data can be acquired across a broader spectrum than the human eye can sense. Due to these reasons remotely sensed data has been a growing source for monitoring and observing environmental change over the last few decades (Lu *et al.,* 2004).

2.2 Radio Detection And Ranging (Radar)

Radar is a remote sensing device, capable of capturing information and data about a target in the microwave section of the electromagnetic spectrum (at wavelengths longer than 1mm) where solar irradiance is insignificant (even if the Earth does emit some microwave radiation). Imaging sensor systems fall into two broad categories, either passive or active sensors. Passive sensors benefit and utilize natural radiation emitted or reflected by the earth (or another planet's) surface, whereas the latter transmit and then receive the backscattered signal (Franceschetti & Lanari, 1999). The advantage of imaging radars is that they transmit and receive electromagnetic signals that disseminate through the atmosphere without sizable signal degradation, regardless of the presence of artefacts such as fog, clouds, smoke and aerosols. Thus, imaging radars have night-time and all weather capabilities, which give them significant advantages over optical techniques. They enable the rapid and continuous monitoring of ground movement phenomena as well as data acquisition in cloudy regions (Massonnet & Feigl, 1998).

2.2.1 History

The preliminary concept of measuring distant targets by radio waves was a notion formed and patented by a German Scientist, Huelsmayer, at the start of the twentieth century. It was rediscovered by Taylor and Young, two Americans, in 1922 but again nothing came of it. The catalyst for radar research and development was World War II, as it was a vital tool for the British and American navies for the detection of surfaced submarines and enemy vessels. Additionally it was also used by aircraft, becoming a crucial component of the air defence system (Mather, 2004). Radar has evolved vastly since it first appeared as predominantly a military system used to detect ground, sea and air targets; today there are many more applications from important research in earth and planetary science to commercial aviation (Curlander & McDonough, 1991).

The initial notion of imaging the earth via radar ascended towards the end of the 1950s. Early images of ground echoes were considered unwelcomed noise, as radar was primarily developed to measure the distance of objects (hence the acronym 'Radio Detecting And Ranging') but they later became a valuable signal to investigate large areas when installed on planes and satellites (Massonnet & Feigl, 1998). When the Seasat satellite was launched in 1978, radar remote sensing from space arose, from which scientific applications developed. But it was not until the 1990's that there was a wide range of radar acquisitions, which intensified in 1991 with the launch of three satellites; Almaz-1, ERS-1 and JERS-1. Development continued with Radarsat-1 being launched in 1995 and many more commencing operations in the new millennium. Today radar remote sensing from space is characterised by rapid technological developments, diverse sources of data and high levels of international collaboration and involvement (Lillesand, Keifer & Chipman, 2008).

2.2.2 Side Looking Airborne Radar (SLAR)

Initial airborne systems were similar in principle to ground-based radars; the antenna was mounted along the top or side of the aircraft, pointed to the side at 90 degrees to the course of forward momentum. The antenna emitted a pulse of electromagnetic energy and the backscattered radiation from the target was received and detected by the same antenna, imprinting the result on a cathode ray tube. A substantial drawback of this technique was the spatial resolution achievable, as the resolution achieved is proportional to the length of the antenna. For airborne sensors this is less problematic but for spaceborne antennas it presents a significant practical difficulty; for example to achieve a

spatial resolution of 30m at an orbital height of 700km, the width of the antenna would have to be several kilometres (Mather, 2004).

2.3 Synthetic Aperture Radar (SAR)

Synthetic Aperture Radar permits the acquisition of data at acceptable spatial resolution from spaceborne platforms. It achieves this by moving small distances along the orbital path, recording the backscatter at each point. By recording at small increments it is possible to simulate an antenna of several kilometres and therefore achieve a higher resolution. To produce and generate a SAR image, millions of pulsations of microwave energy are transmitted and received by an antenna. Similarly to SLAR, the transmitted pulses are scattered by the ground target and the backscattered return pulse is then received by the same antenna. The distance to the ground target can be calculated from the time span between the initial transmission and the reappearance of the pulse because microwave radiation transfers at the speed of light, whilst the azimuth direction is defined by the direction of satellite movement. A radar image is produced when the magnitudes of the processed signal (related to the strength of the backscattered signal) are exhibited in both range and azimuth (Mather, 2004).

Rather than recording localities relative to each conceivable target, to work out whether it is moving away, passing or approaching a target; SAR processing techniques allow the measurement of both the intensity and phase of the reflected radar signal. From the returns of the intensity and phase it is then possible to calculate the location of the target relative to the antenna via the Doppler principle. The basic concept is best explained by an everyday example. The siren on emergency services vehicles is of a different pitch depending on whether it is moving towards us or away from us. When approaching the pitch seems to rise; while moving away the pitch drops. This principle can permit the calculation of motion of a satellite antenna in relation to a target, as well as the absolute distance (in the range of kilometres) between the target and satellite, known as range (Mather, 2004). Figure 2.1 demonstrates the relationship between real and synthetic aperture radar.

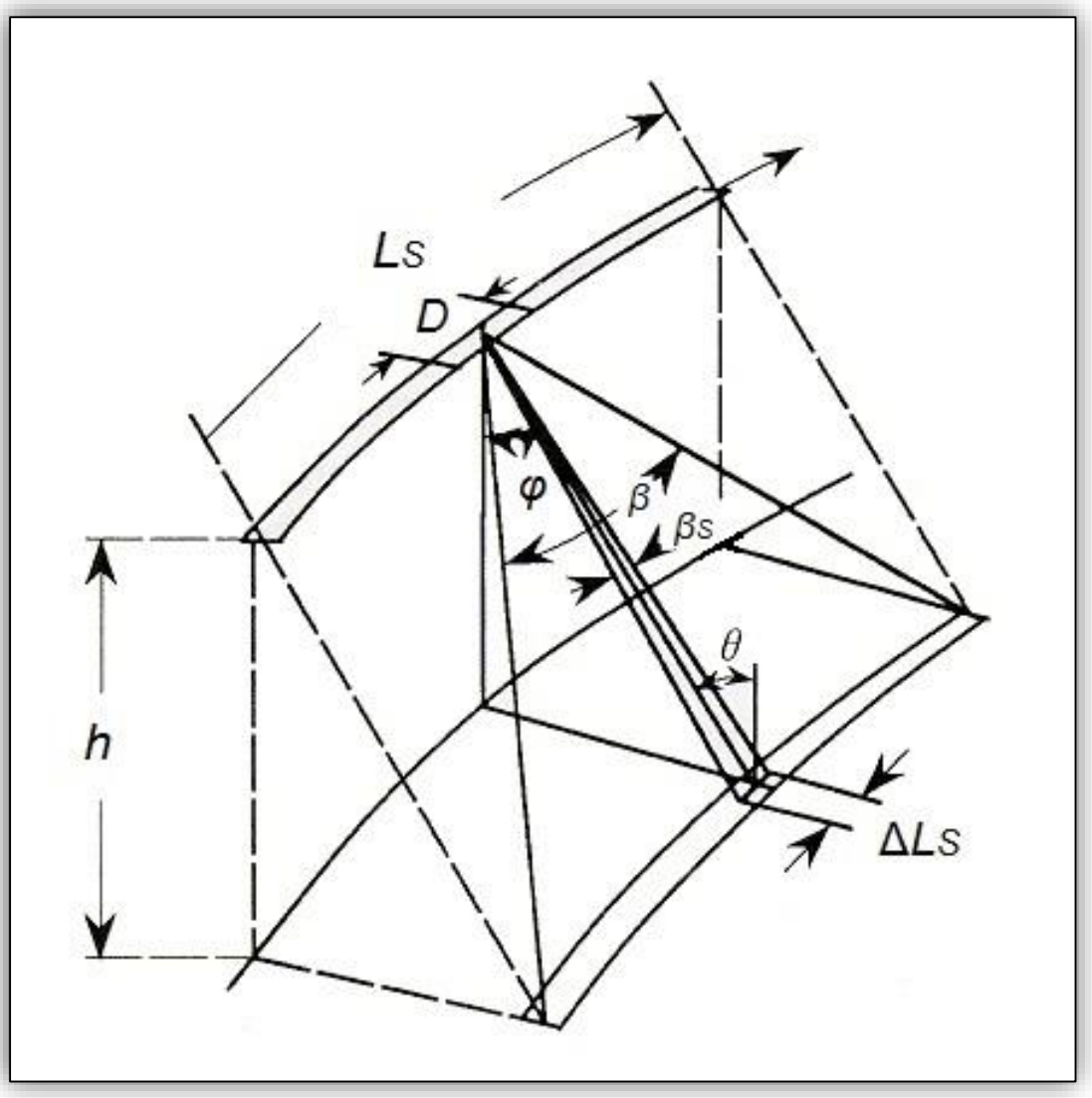


Figure 2.1: *Relationship between real and synthetic aperture radar where: Ls represents the synthetic aperture, D real aperture, β real beam width, βs synthetic beam width, h height, ΔLs azimuth direction, φ off nadir angle and θ incident angle (adapted from JARS, 1999).*

2.3.1 Coherent Imaging

SAR, an active imaging system, measures both the intensity and phase of the returned pulses, and is therefore termed as coherent. The intensity (or amplitude) is predominantly determined by surface roughness, terrain slope and dielectric constants, whereas the phase is determined primarily by the distance spanning the ground target and satellite antenna (Lu *et al.,* 2007). It is the preservation of the phase that gives coherent systems a unique advantage over optical systems, which are not capable of preserving the phase of the suns natural light; therefore data can be exploited in unique ways that are not available with optical imagery.

2.3.2 Electromagnetic Wave Properties

An electromagnetic wave is a self-propagating wave comprising of magnetic and electrical fields that are perpendicular to each other whilst in phase, outlined in Figure 2.2.

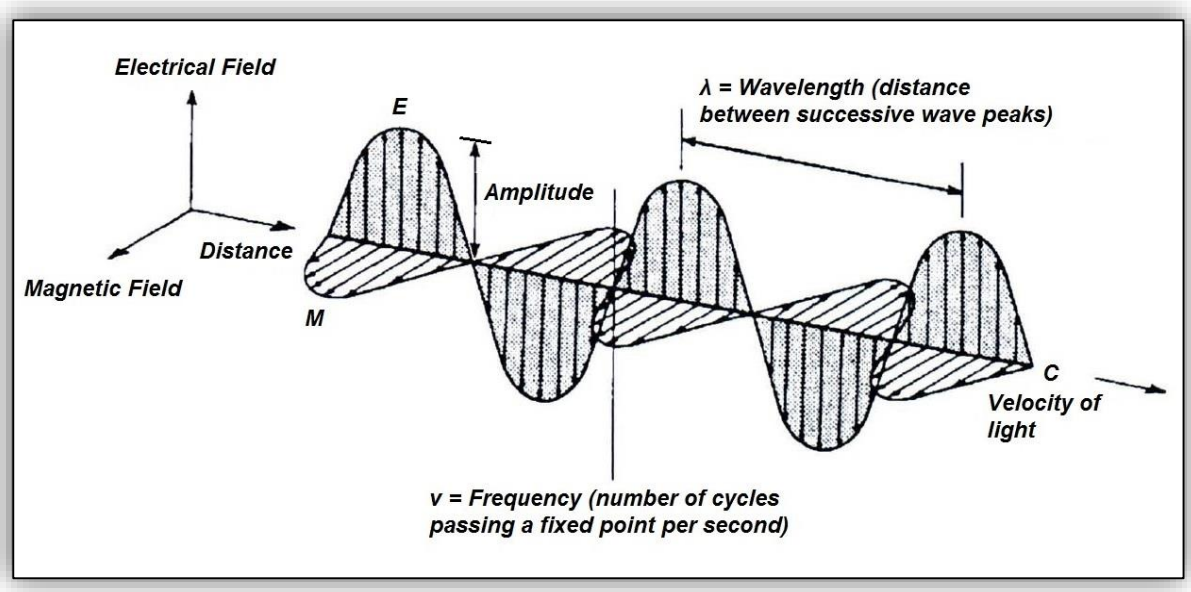


Figure 2.2: *The properties of an electromagnetic wave (adapted from Lillesand, Kiefer & Chipman, 2008).*

The microwave sector of the electromagnetic spectrum is an extremely useful portion from which to obtain valuable data that can assist in environmental monitoring for deformation. Microwave sensors operate at wavelengths that range from 1 millimetre to 1 metre and can therefore be two and a half million times longer in length than the shortest light waves (Figure 2.3). Microwave energy characteristically has two primary qualities that make it well-suited to remote sensing. Firstly, microwave signals can penetrate the atmosphere under virtually all conditions, regardless of clouds, smoke, haze, light rain and snow. Secondly, the reflections from earth's materials at microwave wavelengths have little correlation with the responses from energy in other parts of the spectrum, for example thermal or visible energy. Surfaces may be seen as smooth when imaged from microwave energy, whereas they may appear rough in the visible section, therefore this produces an alternative useful perspective of the environment. The wavelength and the polarization of the energy pulse are two primary elements that influence the transmitted radar signals (Lillesand, Kiefer & Chipman, 2008).

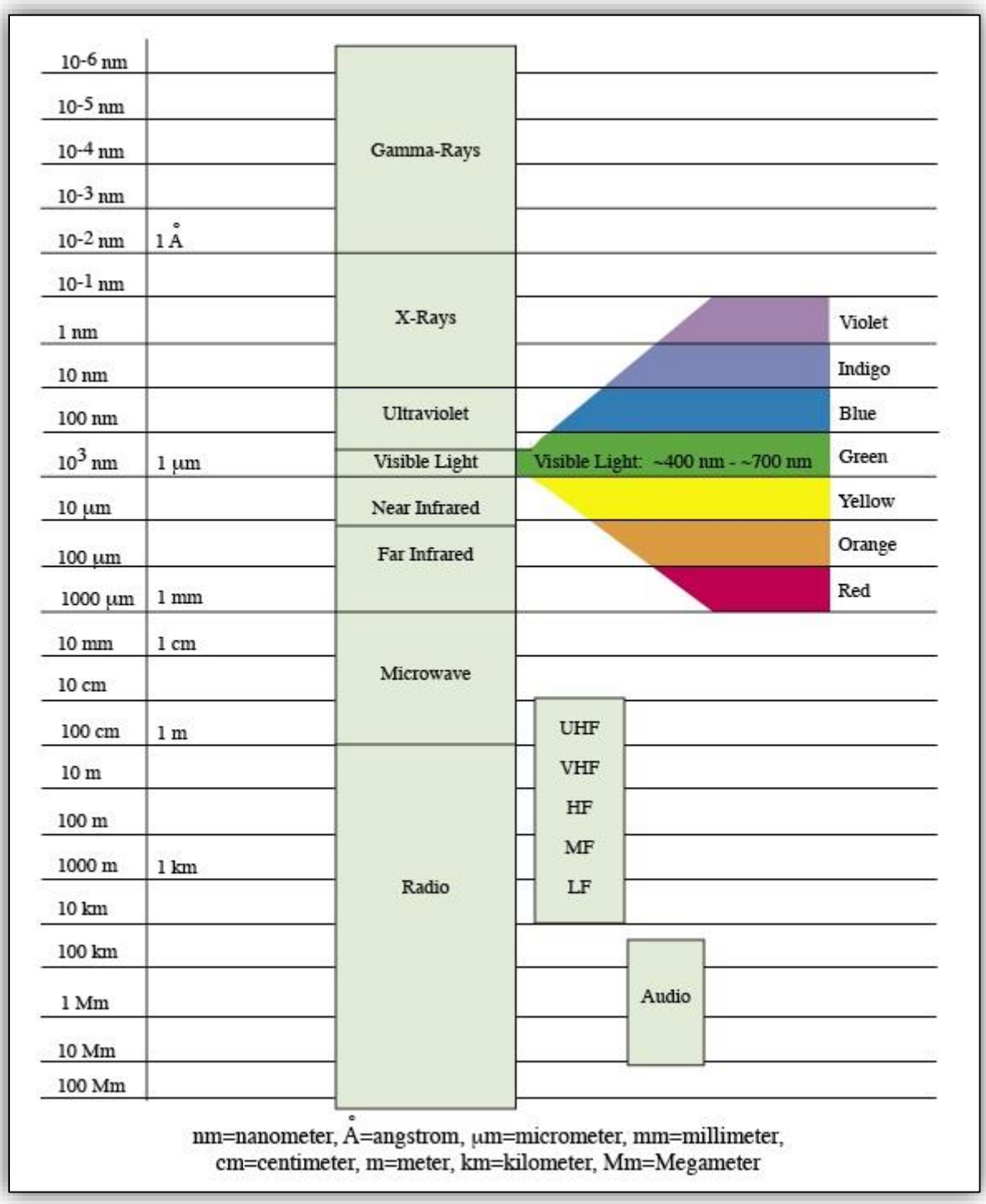


Figure 2.3: *The electromagnetic spectrum (Adapted from University of Colorado Boulder, 2012).*

2.3.3 Wavelength

Wavelength bands are denoted by letter codes, originally arbitrarily designated to guarantee military security during early radar development but have remained implemented due to practicality (Table 2.1). These range from K_a with wavelengths

Band Designation	***Wavelength λ (cm)***	***Frequency $v=c\lambda^{-1}$ [MHz (10^6 cycles sec^{-1})]***
K_a	0.75 – 1.1	40 000 – 26 500
K	1.1 – 1.67	26 500 – 18 000
K_u	1.67 – 2.4	18 000 – 12 500
X	2.4 – 3.75	12 500 – 8000
C	3.75 – 7.5	8000 – 4000
S	7.5 – 15	4000 – 2000
L	15 – 30	2000 – 1000
P	30 - 100	1000 – 300

Table 2.1: *Radar band designations.*

ranging from 0.75 -1.1cm (frequency 40 000 – 26 500 MHz) to P band ranging from 30-100cm (frequency 1000-300 MHz). The wavelength dictates the extent to which it is mitigated and / or disseminated by the atmosphere. Radar signals are affected by the atmosphere most seriously at shorter operational wavelengths (under approximately 4cm) and increasingly as wavelength decreases although, under the majority of operational conditions, minimal attenuation occurs. The influence of rain and clouds can be variable, but habitual cloud cover has a relatively small effect on a radar signal, whereas the consequential echoes from precipitation can be significant. For example some echoes of shorter wavelengths can be significant enough to distinguish expanses of precipitation in plan position indicator (PPI) systems. Rainfall can diminish the incident radar energy, which can either completely inhibit the illumination of the target area or partially inhibit the illumination, whereby some energy penetrates but the signal is diminished after backscatter. In either case far less energy is returned to the antenna. A secondary effect of rainfall is the alteration caused to the terrain which in turn changes the dielectric and physical properties of the vegetation and soil.

The SAR sensors aboard ERS-1 and ERS-2 both operated in the C-band frequency at 5.30 GHz (producing an equivalent wavelength of 5.66cm), while the ASAR sensor aboard ENVISAT also operated within the C-band, similarly at 5.33 GHz (Lillesand, Kiefer & Chipman, 2008).

2.3.4 Polarization

Electromagnetic radar signals are transmitted and received in different polarization modes. The polarization of a radar signal delineates the geometric plane in which its electrical field is oscillating. Unpolarized energy oscillates in all directions at 90^o to the

direction of travel, whereas multipolarization radar systems enable the filtering of the signal to restrict vibrations to a single plane perpendicular to the wave path direction. Conventionally, radar signal is transmitted in a plane that is either perpendicular (vertical polarization, V) or parallel (horizontal, H) to the antenna axis (Figure 2.4) and equally may only receive signals with a specified polarization. Like-polarized signals refer to when the transmitted and received signals are the same (eg. HH or VV), whereas cross-polarized indicates that the sent and received signals are different (eg. HV or VH). (Lillesand, Kiefer & Chipman, 2008). ERS-1 and ERS-2 SAR sensors operated in a VV polarisation, while ENVISAT offered a choice of five different polarisations (VV, HH, VV/HH, HV/HH, or VH/VV) (ESA, 2015a).

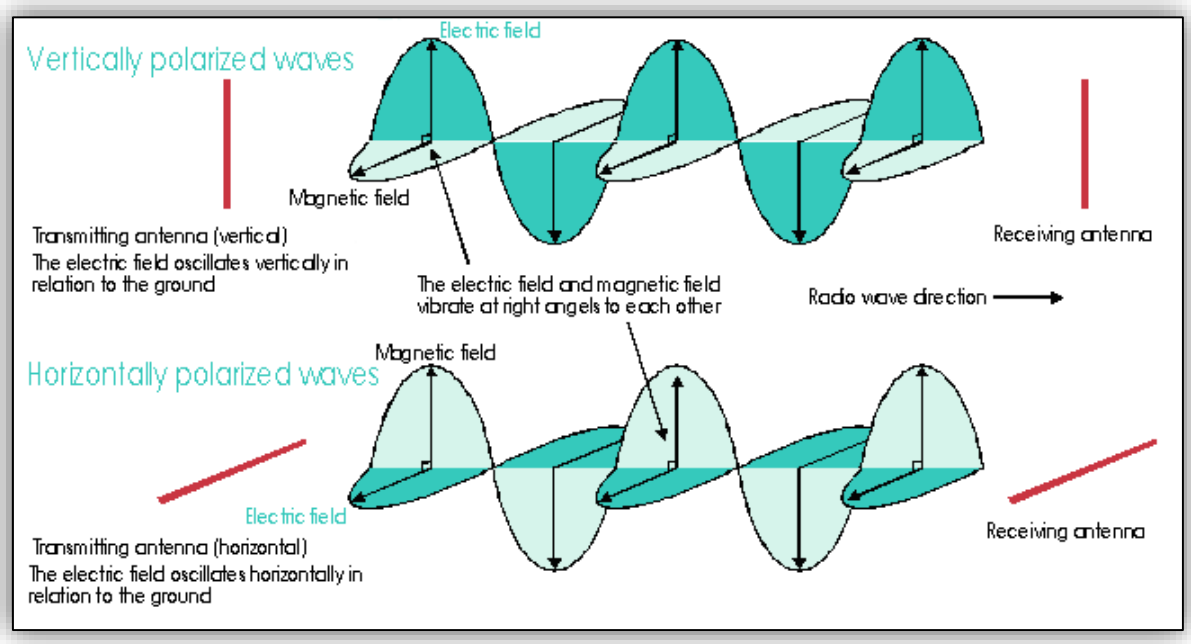


Figure 2.4: *Linearly polarized radiation (Circuit Design Inc., n.d.).*

2.3.5 Imaging Geometry

The ERS SAR sensors were located at 90° degrees to the satellites flight path and 20.3° to the right of nadir, which directs the narrow beam downwards and sideways onto the earth's surface. Figure 2.5 displays a typical SAR imaging geometry. The electromagnetic pulses irradiate a swath parallel to the satellite track due to the spacecraft velocity. The footprint of an individual pulse is demarcated by the dark shaded area. The complete SAR image initiates in azimuth at the 'early azimuth' period and lasts until the 'late azimuth' period. In range direction, it covers the interval from 'near range' to 'far range', which

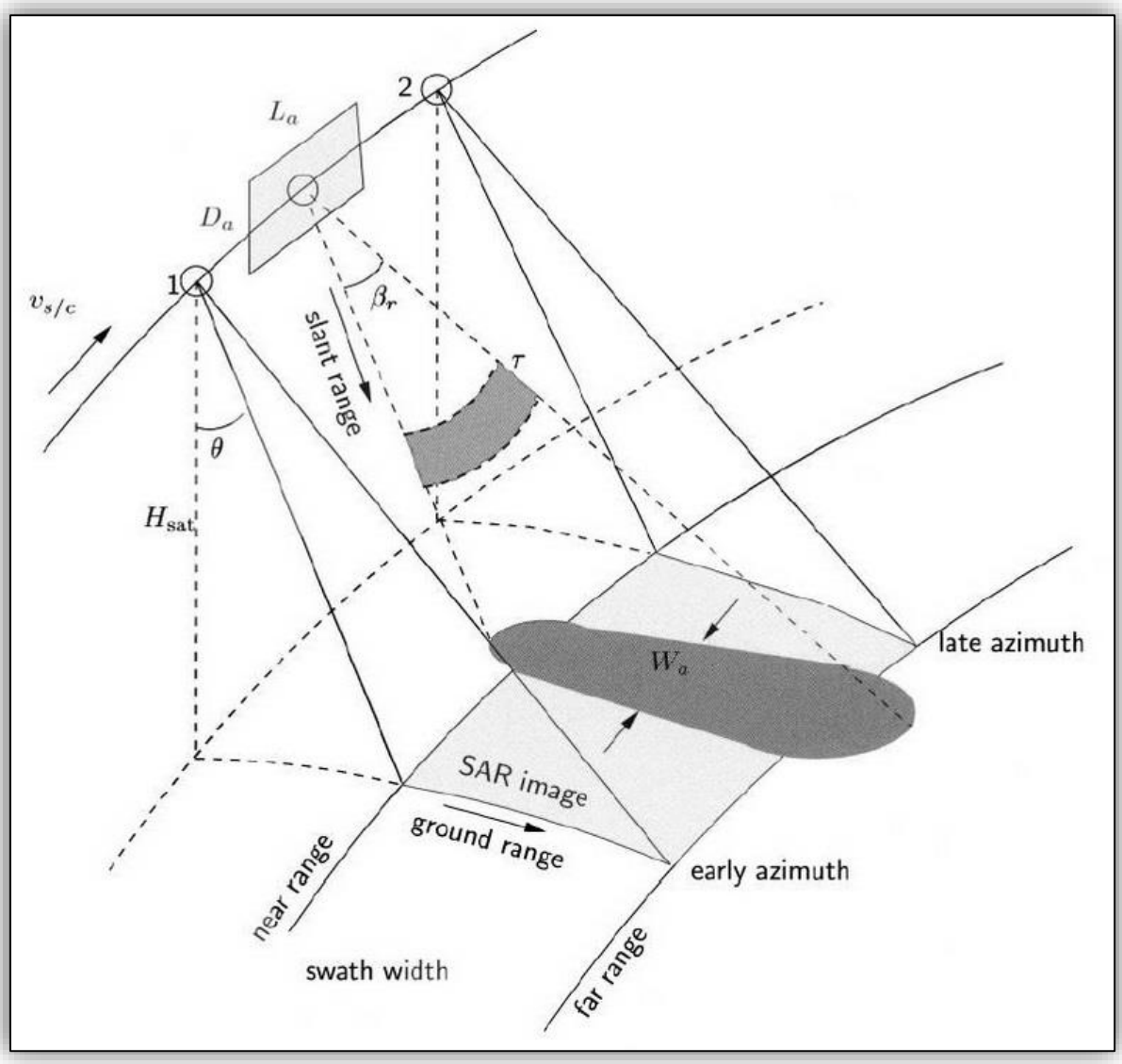


Figure 2.5: *Imaging geometry of a SAR acquisition where: $v_{s/c}$ represents spacecraft velocity, L_a antenna length, D_a antenna width, τ pulse width, θ look angle, βr beam width, H_{sat} satellite altitude and W_a radar footprint width (Hanssen, 2001)*

relates to the light shaded area in ground range. The ERS satellites had an approximate swath width of 5km in azimuth direction and 100km in range direction. Strips of imagery are built up from the processing of the return signals.

2.3.6 Resolution

Resolution is defined by Born & Wolf (1959) as the minimal distance at which two individual scatterers with an identical brightness can be uniquely distinguished as distinct signals. Regardless of the system, the fundamental resolution equates to one over the system bandwidth, which is related with the width of the impulse response. These time

measurements are simply converted into spatial measures. The illuminated region accountable for the radar reflection data mapped to a solitary pixel, defines a resolution cell; consequently the resolution in azimuth and range defines the resolution cell size. Aberrantly, pixel size is an unclear measure as habitually it is used in the same context as resolution. A pixel by characterisation does not have a physical size; it is an arbitrary (small) point where the digitized signal value associated with a resolution cell is centred. Posting is a suitable alternate for pixel size, as it relates to the spatial distance between two given pixel-nodes. Where sampling frequency and bandwidth are identical, resolution cell size and posting have equal values; however for the majority of SAR systems the signal processing algorithms necessitate oversampling amongst neighbouring pixel values. For ERS SAR images there is a 50% overlay amongst adjacent resolution cells, which corresponds to an oversampling ratio of approximately 1.223 (Hanssen, 2001).

2.3.7 Range

To distinguish between two ground features in close proximity in the range direction, a SLAR antenna must receive all parts the return radar pulse separately. It is a prerequisite that the features must be separated, in slant range, by a distance exceeding half the physical dimension of the pulse. If this does not occur and there is a time overlap between the signals, features will be blurred together in the radar image (Lillesand, Kiefer & Chipman, 2008). Chirping, where the pulse is Frequency Modulated (FM), is applied prior to the radar wave's transmission. The pulse is transmitted and subsequently received, with the echoes of the pulse gathered at different times (directly proportional to their ranges). The significance of chirping is that a matched filter can be implemented to the received signal to individually delay differing frequency constituents of the signal so they are all received at the same time. The shorter the pulse, the closer in proximity the two targets can lie before their echoes overlap and therefore the higher the resolution (Woodhouse, 2005).

2.3.8 Azimuth

To resolve two ground features in the azimuth direction, the spatial separation must be greater than the focused beam width on the ground. The resolution is contingent on the synthetic aperture of the radar antennae. The motion of the satellite induces the Doppler effect which prompts a frequency modification of the returned pulse. From the moment of first azimuth of an object, to the moment of last azimuth, an abundance of backscattered echoes are received by the sensor. The footprint on the ground is the real aperture, which for ENVISAT is a few kilometres. Azimuth compression, where numerous returns from a

singular object are resolved into a single response, in essence reduces the azimuth resolution from the order of kilometres to the order of metres, via natural Doppler chirp (Hanssen, 2001).

2.3.9 SAR Image Properties

SAR images are essentially a two dimensional matrix of complex values, where each pixel is allied to a resolution cell, an area on the Earth's surface. These pixels each store a complex number, which enable the derivation of the phase and amplitude of the backscattered signal. The complex value has an inphase component (R_e) in addition to an imaginary quadrature element (I_m) (Figure 2.6). By converting from a Cartesian coordinate system into a polar coordinate system the phase and amplitude values for every pixel can be attained. For a pixel in a given array with coordinate *(a,b)* the phase *(φ)* and amplitude *(α)* values can be calculated by the following equations:

$$\varphi = \tan^{-1}(b / a) \qquad (2.1)$$

$$\alpha = \sqrt{a^2 + b^2} \qquad (2.2)$$

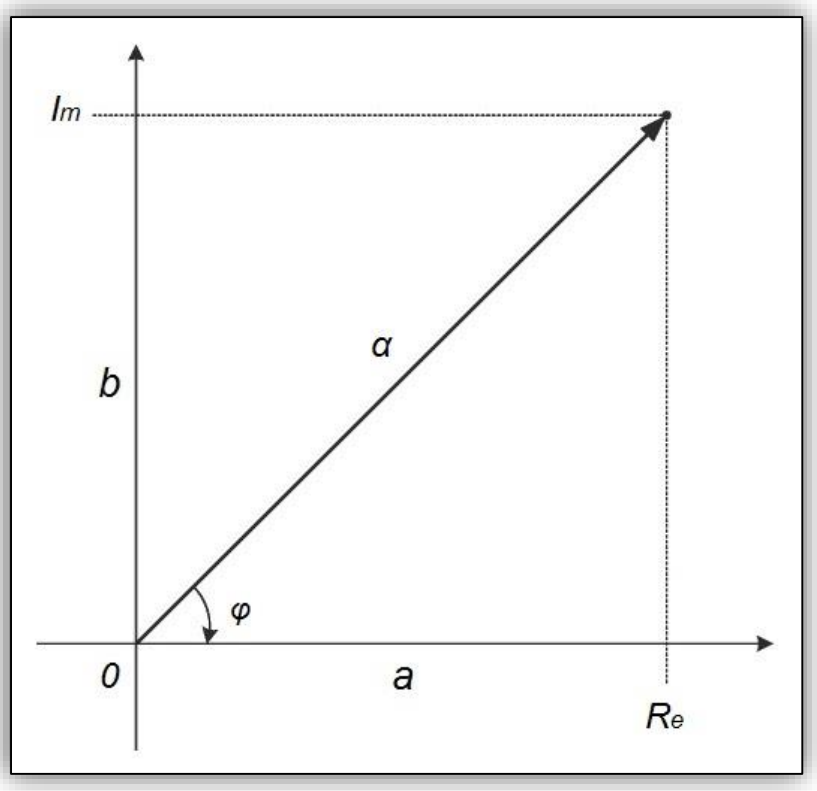


Figure 2.6: *Argand diagram of a Single Look Complex pixel.*

The size and locality of the resolution cell are dependent of the sensors characteristics. The ERS and ENVISAT sensors have a ground range of approximately 25m and 30m respectively. They acquire data in strip-map mode where rows comprise azimuth locations and columns comprise slant range locations on the ground; the strip is scanned in range direction, resulting in a 100km by 100km area. These radar amplitude images display the intensity of the backscattered signal which can be visualised in greyscale (Adamska, 2012).

2.3.10 Geometric Distortion

Geometric distortions to the radar image occur due to the side looking nature and operational parameters of SAR. These distortions are generated by topographic relief features and manifest in three distinct ways: foreshortening, layover and shadow.

2.3.10.1 Foreshortening

When topographic features, such as hillsides, face towards the look direction of the SAR sensor, foreshortening occurs (Figure 2.7). For example, for the slope AB (base A, summit B) the pulses returned back to the sensor will arrive at similar times because of the similar slant range, regardless of the genuine ground range between them. As a consequence in the SAR image they will appear much closer together.

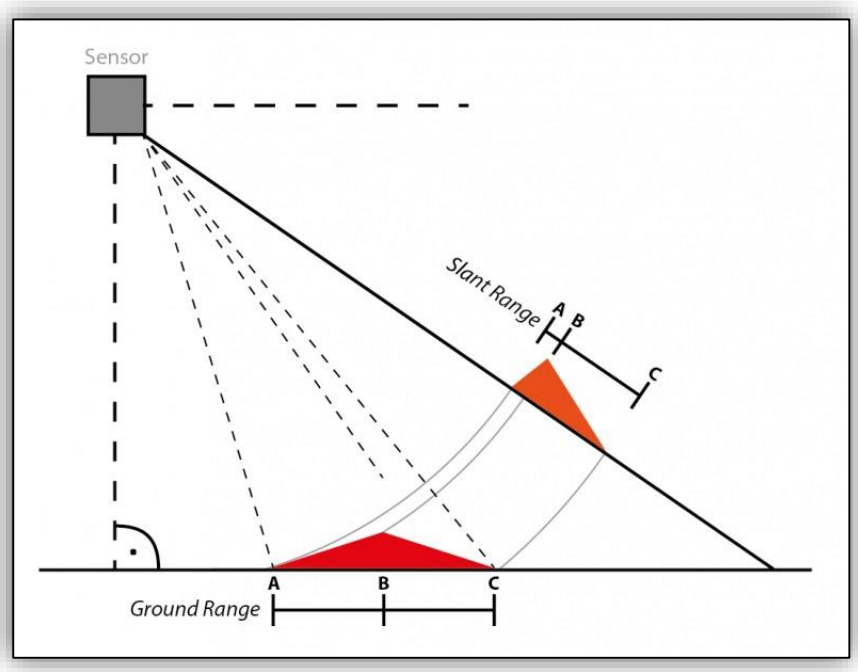


Figure 2.7: *Foreshortening (GISwiki, 2015).*

2.3.10.2 Layover

Layover is essentially a more extreme variety of foreshortening, whereby the slant range of B is less than the slant range from A (Figure 2.8). The return echo from B will reach the sensor before A, therefore being located in the incorrect range bin and consequently B will be laid over A in the SAR image.

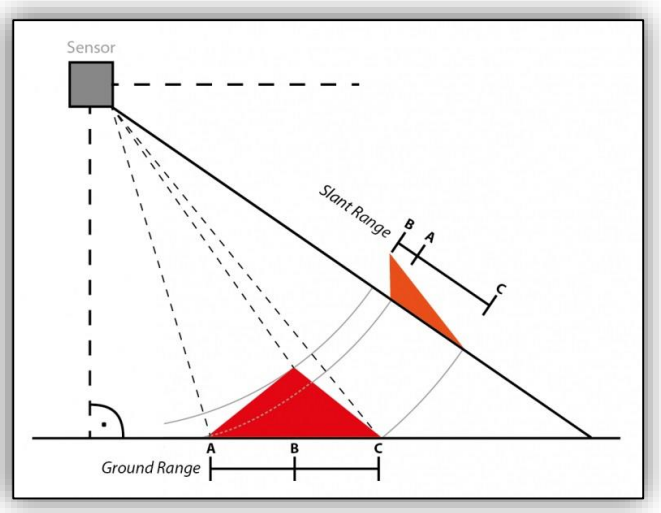


Figure 2.8: *Layover (GISwiki, 2015).*

2.3.10.3 Shadow

Shadow occurs when a feature being imaged is too steep for the SAR sensor to illuminate both sides of it (Figure 2.9). The slope facing the opposite direction from the look angle cannot be imaged which creates a shadow of no data and therefore no information can be discerned about the area (B to D). This shadow effect is exacerbated with lower elevation angles.

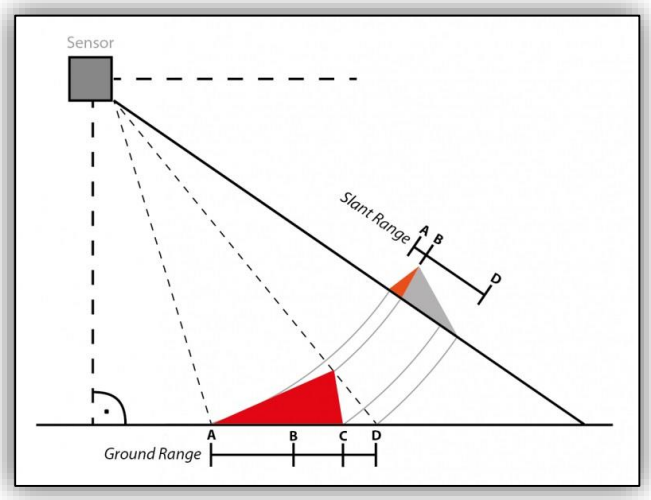


Figure 2.9: *Shadow (GISwiki, 2015).*

2.3.11 Image Speckle

Radar speckle is the ostensibly random pattern of lighter and darker pixels within the image and is contained within every radar image to a certain degree. As previously mentioned, radar pulses are emitted coherently, whereby the transmitted waves are oscillating in phase. Within a single pixel or ground resolution cell the signal will travel marginally different distances from leaving the antenna, to reaching the surface and returning back to the antenna. As a consequence these waves will be to some degree in or out of phase on return to the antenna; when in phase the intensity of the signal is amplified (due to constructive interference) and conversely when out of phase the combined signal intensity will be reduced (due to destructive interference). This constructive and destructive interference gives radar imagery a characteristically grainy appearance. However, it is important to note that this is a result of sub-pixel-scale geometry of the radar illumination conditions and not simply random. Speckle will be highly correlated if images are acquired from an identical locality, with the same polarization and wavelength along with equal ground surface conditions. Processing techniques can be employed to reduce speckle, for example multi-look processing and speckle filters, although there is always a compromise between speckle reduction and spatial resolution (Lillesand, Kiefer & Chipman, 2008).

2.3.12 Satellites

The ERS-1, ERS-2 and ENVISAT satellites are suited to deformation mapping due to their regular revisit time of 35 days. In addition there is a large historical archive of imagery of over two decades, from 1991 to 2012, which enables long deformation time series to be created. This data archive has been extensively used in studies of deformation induced by activities such as mineral extraction in the past including Cao *et al.* (2008), Del Ventisette *et al.* (2013), Sowter *et al.* (2013) and Bateson *et al.* (2015); to name but a few.

2.3.12.1 ERS

ERS-1 was launched by the European Space Agency (ESA) on July 17th 1991, with its successor ERS-2 launched four years later on April 21st 1995. The predicted lifespan of the satellites was at a minimum of three years but they managed to function for far longer, with ERS-1 withdrawn from operation on March 10th 2000 and ERS-2 withdrawn on September 5th 2011 (ESA, 2015b). Both systems had sun-synchronous orbits at a nominal altitude of 785km at an inclination of 98.5°. Both satellites carried three primary sensors; a Ku-band radar altimeter, an along-track scanning radiometer and a C-band active

microwave instrumentation (AMI) module. The AMI contained a SAR system, operational in either Wave or Image Mode, and a microwave scatterometer that functioned in Wind Mode. In Image mode SAR data was produced over a 100km right-looking swath with a VV polarisation, four-look resolution in the vicinity of 30m and a 23° look angle (beam centre). The system was only functional when in line-of-sight communication with an ERS ground station due to the high data and power rates. The ERS radar systems functioned at a shorter wavelength than various other operational spaceborne systems at the time (Lillesand, Keifer & Chipman, 2008).

2.3.12.2 ENVISAT

ENVISAT was launched by ESA on March 1st 2002 and manoeuvred into an orbit that emulated ERS-2's covering an identical ground track (to within 1km). The Advanced Synthetic Aperture Radar (ASAR) system functioned in the C-band, at similar wavelengths to the SAR system on board ERS-1 and ERS-2. The sensor could be operated in a variety of modes including Wide Swath Mode, Global Monitoring Mode and Alternating Polarization Mode. Crucially for uniformity between ERS-1 and ERS-2 it retains the Image and Wave modes operational on the previous satellites. Image mode produces four-look high resolution images (30m) and has the capability to function in one of seven programmed swath alignments, with swath widths spanning from 58 to 109km and look angles extending from 14° to 45°, in either VV or HH polarizations (Lillesand, Keifer & Chipman, 2008). Connection with the satellite was lost on April 8th 2012, just after the tenth anniversary of its launch (ESA, 2015a).

2.3.12.3 Sentinel-1

Sentinel-1 is ESA's latest satellite mission, founded and established on the legacy of ERS and ENVISAT. Sentinel-1A was launched on 3rd April 2014, carrying a 12 metre long C-band SAR sensor operating at 5.405GHz, following a polar, sun-synchronous orbit at an altitude of 693km. The Sentinel-1 mission has been devised as a two-satellite constellation, with Sentinel-1B launching in 2016. The identical satellites will orbit 180° apart, which will produce a global revisit time of six days, but in many areas will be even better, for example at the equator (3 days) and the Artic (less than a day). The SAR sensor can operate in four different modes: interferometric wide-swath mode at (5m x 20m spatial resolution); wave-mode (5m x 5m); strip map mode (5m x 5m) and extra wide-swath mode (20m x 40m) (ESA, 2015c).

2.4 Interferometric Synthetic Aperture Radar (InSAR)

Interferometric Synthetic Aperture Radar (InSAR) is one of the most rapidly evolving fields within remote sensing and Earth science. Each year better tools are developed to assist in answering and discovering solutions to scientific questions posed by natural resource management and hazard monitoring. Following on from SAR, InSAR was developed to overcome some of the limitations of traditional SAR systems most significantly by measuring in a three dimensional coordinate system rather than two. Its application to monitor ground motion associated with geophysical and anthropogenically induced events has evolved rapidly since the use of single interferograms during the 1990s and is now an established technique (Ramsey *et al.,* 2013). The development of InSAR techniques and implementations significantly expanded in 1991 with the launch of the ERS-1 satellite from which three strands of predominant research trends became apparent: digital elevation model (DEM) generation; landscape characterization; and deformation mapping.

2.4.1 Interferometry

Interferometry is the name given to a group of techniques where information about waves is deduced via their superposition. The interferometry principle of electromagnetic signals is based on the wave front concept that was developed in the 1960s. It firstly discerns that intersecting light beams from two sources do not rebound off each other as would be predicted if they were assembled from particles; and secondly that a growing sphere of light acts as if each locality on the wave front were a new source of radiation of equivalent phase and frequency (Hanssen, 2001).

The superposition principle enunciates that for every linear system the net aggregate at a particular time and place, initiated by two or more stimuli, is the total summation of the responses which would have been produced by each stimulus independently. For example say stimuli *A* results in outcome *X* and stimuli *B* results in outcome *Y*, then *(A + B)* consequently results in outcome *(X + Y)*. The phenomenon of interference concerning electromagnetic waves is established on this notion. When electromagnetic waves traverse in the same locality, the resultant amplitude at each point is the summation of the individual wave amplitudes; resulting in either constructive or destructive interference. Destructive interference occurs where the summed variation has a lesser amplitude than the component variations, alternatively when the summed variation has a greater amplitude than the component variations, constructive interference occurs (Figure 2.10). For a comprehensive explanation of interferometry please refer to Hariharan (2010).

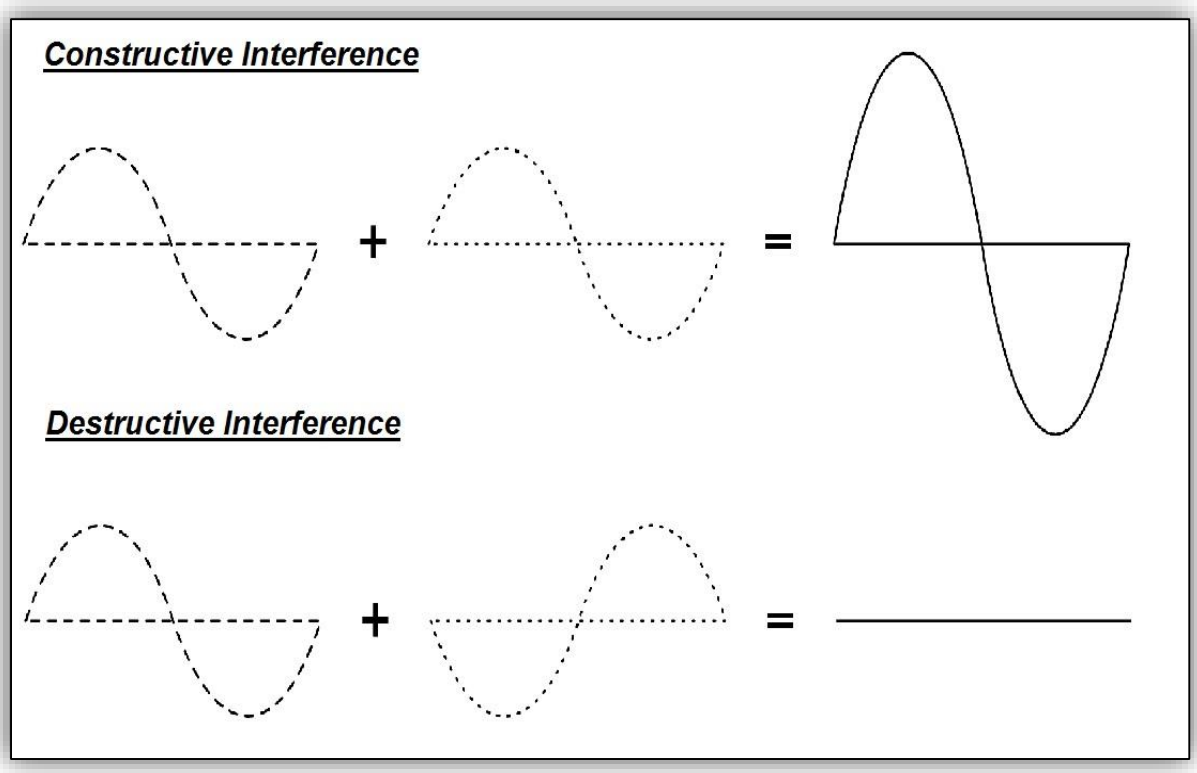


Figure 2.10: *Constructive and destructive interference (Discovery Center of Idaho, 2015).*

Multiplicative interferometry is capable of measuring the interferometric phase, achievable by coherent cross-multiplication of the two input signals. Consequently the phase data produce a higher degree of accuracy because it is far easier to decipher the fraction of the phase cycle. For two dimensional applications, a 2π phase-cycle is generally referred to as a fringe (Hanssen, 2001).

2.4.2 Interferometric Phase

When two radar signals are combined or 'interfered' from two temporally or spatially separated antennas, InSAR is formed. It utilizes the interference of electromagnetic waves to derive precise alterations in elevation. An interferogram, or InSAR image, is generated firstly by co-registering the two SAR images, followed by calculating the difference in phase between the images on a pixel-by-pixel basis (Lu *et al.,* 2007). Two functions are displayed in Figure 2.11, firstly *sin(x)* and secondly *sin(x + π/2).* The *sin(x)* curve has a phase equal to zero (as at zero *sin(0) = 0*) whereas the second curve subsequently trails the *sin(x)* curve by *π/2* radians, which is visible at *x=6.28* radians. Envisaging that the *sin(x)* curve is a typical microwave SAR pulse and *sin(x + π/2)* denotes the return pulse, the difference between the sent and received signal is *π/2* radians. The shift of the peaks,

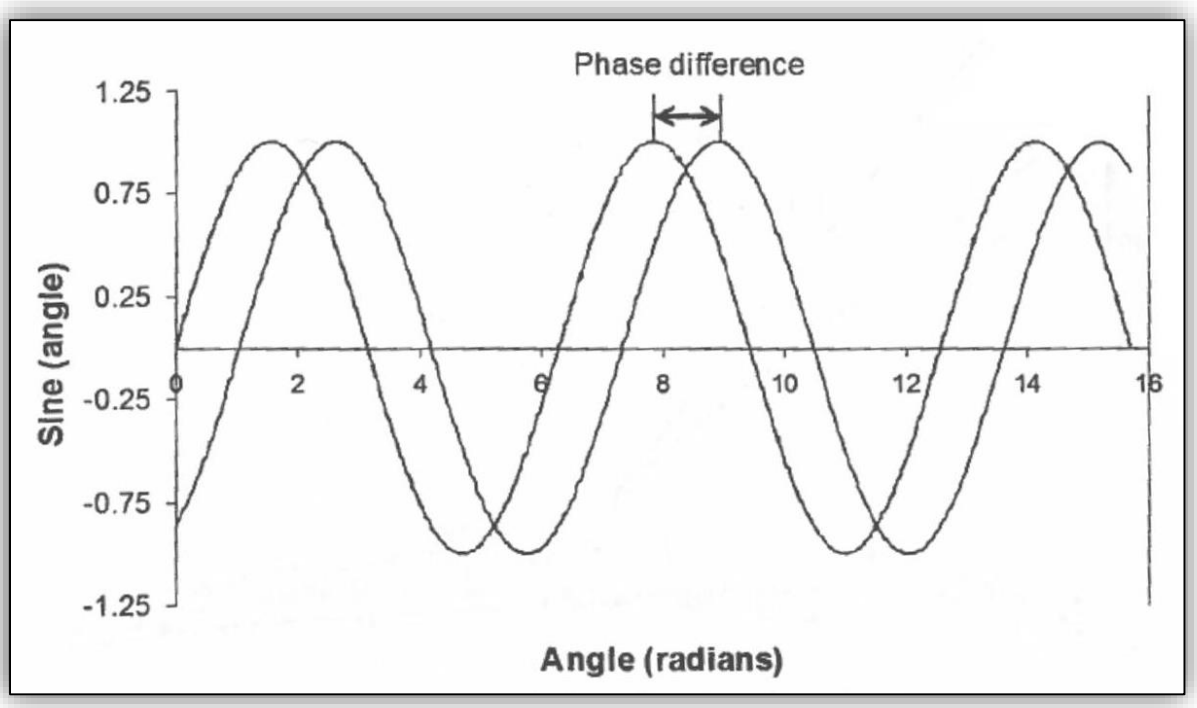


Figure 2.11: *Phase difference between sin (x) and sin (x + π/2) (Mather, 2004).*

from the first wave to the second, is the shift in phase angle, which in this example equals *π/2* radians. It is important to note that phase angle cannot be equal to or exceed *2π* radians. For each pixel in a SAR image the phase change in relation to transmitted and received energy along with the magnitude of the return signal is recorded. Magnitude data can be attained in the arrangement of single-look complex images (SLC). Whilst the phase data for a solitary individual image is of little applicability, the interferometry technique with the operation of two or more SLC images of the same area enables the retrieval of phase differences between the images (Mather, 2004).

The resultant phase change between the two images is caused by predominantly five effects: landscape topography, satellite orbital differences, ground surface deformation, environmental and systematic noises and atmospheric propagation delays. The objective of interferometric processing is to identify and isolate these effects, by inputting information to reduce the amount of unknowns in the phase contribution. For example topographic contributions can be eliminated via a DEM and knowledge of the InSAR imaging geometry. Satellite orbital discrepancies can be removed with information of the satellites position and attitude (Lu *et al.,* 2007). Once necessary components have been separated, phase associated with ground movement can be recognized and elevations of the pixels above a datum can be computed (Blanco-Sanchez *et al.,* 2008).

2.4.3 Configurations

2.4.3.1 Single-Pass

The configuration of satellites with SAR payloads varies, depending on the product desired. To acquire high resolution DEMs, two antennas may be mounted upon a single platform, therefore having a fixed and known spatial baseline. The Shuttle Radar Topography Mission (SRTM) and Topographic SAR (TOPSAR) used these configurations and have successfully obtained highly precise DEMs over vast expanses. InSAR was initially used to measure the Earth's topography in the form of DEMs, which could be employed to monitor features such as ground surface deformations. DEMs can be produced by interferograms, manufactured by the minor dissimilarities in observational location between the two images (Lu *et al.,* 2007).

The single-pass configuration has some advantages over a repeat-pass configuration. Firstly, the images are highly correlated because the conditions under which the area was imaged are equivalent, therefore the backscattered electromagnetic radiation from the target to the antennae are practically identical. High coherence is a necessity for efficacious interferometry as it means that the characteristics of backscattering from each pair of equivalent points in the two images are equal. With repeat pass-interferometry the backscattering properties of the target area may have changed between the two dates of data acquisition, therefore reducing the level of correlation. Secondly, when the single pass-approach is implemented the atmospheric conditions are akin from the antennae locations. The incidence of water vapour as well as tropospheric effects can affect microwave energy propagation through the atmosphere. These effects are imperfectly understood but can result in substantial discrepancies in phase determination from SAR images. These effects are also negated by employing single-pass interferometry rather than repeat-pass interferometry (Mather, 2004).

2.4.3.2 Repeat-Pass

Alternatively, InSAR can be generated by a single antenna mounted upon a space or airborne platform with a near identical flight orbit for repeat-pass interferometry. Via this method InSAR is proficient in measuring sub-centimetre ground surface deformation over large regions with a spatial resolution of tens of metres. Whilst antennas do not illuminate the section of Earth at the same time, the two data sets received during the two passes can be highly correlated if the scattering properties of the target surface remain largely unaltered between recordings (Massonet & Feigl, 1998).

The repeat-pass configuration has a significant advantage over the single-pass arrangement. Single-pass interferometry is constricted in the spatial baseline that can be realized. Baseline length is fundamental as it influences the sensitivity of the connection concerning phase and height; as height sensitivity (the rate of height change with phase difference) is directly proportional to baseline length. Therefore, when all else is consistent, lesser alterations in phase angle yield comparatively large changes in calculated ground elevations when the baseline is short. Aptly for longer baselines the opposite applies. The separation between two orbits is often in the order of several hundred metres, whereas for a fixed mast serving as the second antenna it's far less, with for example the SRTM having a 60m baseline. The critical baseline, where decorrelation occurs because the baseline becomes too long for the phase differences to be calculated, is of the order of 1 kilometre for ERS satellites (Mather, 2004).

2.4.4 Repeat-Pass Geometry

The phase ϕ of a radar wave is directly proportional to the two way travel of the signal; the path from the sensor to the ground and the ground back to the sensor. As the two satellites are different distances away from the target, they receive marginally different phase values; the phase difference can be utilized to calculate the topographic height of *h* on the ground. Referring to Figure 2.12, *SAR 2* is further away from *SAR 1* by the amount of ΔR (therefore $R_{S,2} = R_{S,1} + \Delta R$):

$$\phi 1 = -\frac{4\pi}{\lambda} Rs + \phi scatt\ 1 \qquad (2.3)$$

$$\phi 2 = -\frac{4\pi}{\lambda} (Rs + \Delta R) + \phi scatt\ 2 \qquad (2.4)$$

ΔR is dependent on $B\perp$, the perpendicular baseline between the two SAR antennae, and φ the angle between absolute and perpendicular baseline:

$$\Delta R = B\perp \tan \varphi \qquad (2.5)$$

Holding the assumption that backscattering properties are consistent at both acquisition times (i.e. $\phi\ scatt1 = \phi scatt2$) then interferometric phase is:

$$\phi int = \phi 1 - \phi 2 = \frac{4\pi}{\lambda} \Delta R \qquad (2.6)$$

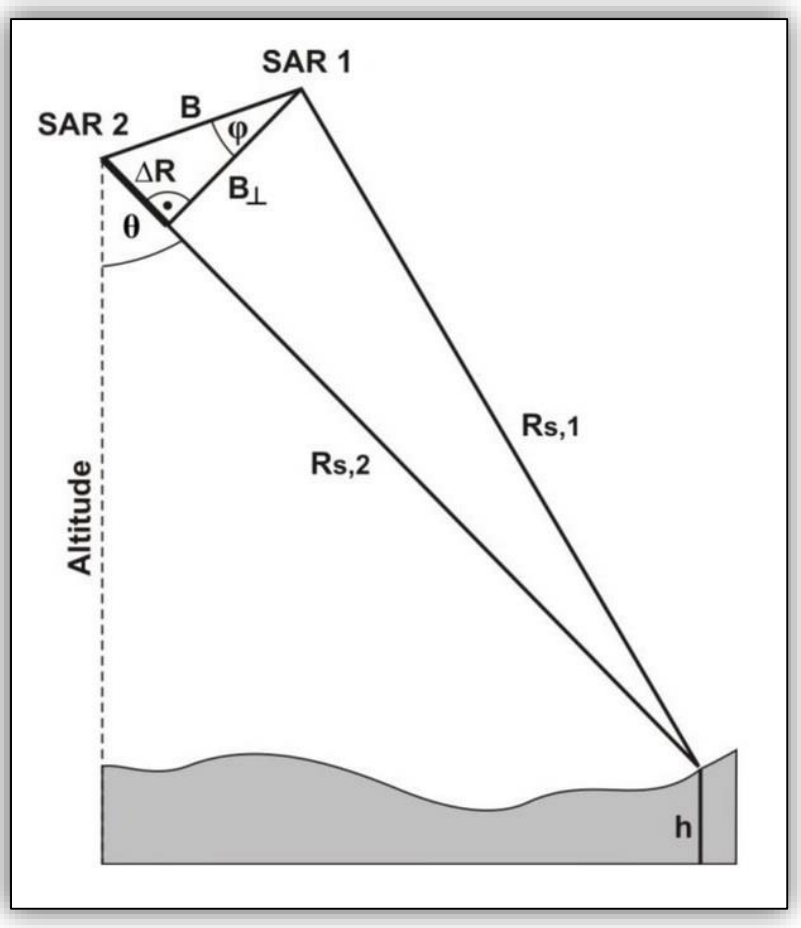


Figure 2.12: *Repeat-pass radar geometry where: SAR 1 and SAR 2 are the two image localities, Rs,1 and Rs,2 distances to antennas SAR 1 and SAR 2 respectively, B spatial baseline, $B_\perp$ perpendicular baseline, θ look angel, φ angle between absolute and perpendicular baseline, ΔR distance difference between $R_S,1$ and $R_S,2$ and h height of object on surface (Plank, 2014).*

2.4.5 Limitations of InSAR

2.4.5.1 Data Availability

SAR data coverage is predominantly sparse. The majority of SAR satellites carry other sensors aboard which means that they do not acquire data constantly. Often there are conflicts between data users, for example between academic and commercial sectors. The required coverage of SAR data needed for successful InSAR and DInSAR of a specific event is often not met. For example deformation events, such as an earthquakes induced by mineral extraction, require that the imagery firstly spans the event and secondly that the data is as uncontaminated as possible from sources such as unrelated motion and temporal decorrelation. ERS and ENVISAT satellites had a repeat pass of 35 days, but there is a demand for shorter revisit times.

2.4.5.2 Noise Effects

Noise effects on the interferograms, denoted as the decorrelation phenomena, are perhaps the biggest limitation of InSAR (Zebker & Villasenor, 1992). Noise can ensue due to any effect that results in variations in the 'radar observation' of the imaged region, for what attains its electromagnetic response (reflectivity).

Decorrelation can occur on two domains, spatial and temporal. Spatial decorrelation transpires when the imaging direction is different due to the spatial separation between two acquisition orbits. The spatial separation amongst orbits is commonly referred to as baseline; keeping this to a minimum can help to reduce topographic errors and spatial decorrelation. The length of the geometric baseline determines the height sensitivity, with large spatial baselines more sensitive to height changes. If the perpendicular baseline exceeds the critical baseline, the distance by which the images decorrelate, interferometric analysis is not possible (Berardino *et al.,* 2002).

Temporal decorrelation is the phenomena when relative movements of scatterers within a resolution pixel cause the scatterer contribution to sum differently. It occurs when the reflectivity of the targeted area changes between sensor observations and can transpire in a matter of minutes for some land cover types (Lanari *et al.,* 2007a). Even at very high resolutions, the value of each pixel remains the sum of many scatterers on the surface. If and when these scatterers relocate with regards to each other between satellite passes (common amongst vegetation), then the phase of the return signal will differ arbitrarily, which results in decorrelation (Hooper *et al.,* 2007). For example in forested areas, leaf orientations can alter with respect to the direction of SAR illumination due to wind action, while water bodies can also decorrelate quickly due to waves. Agricultural areas experience moderate levels of decorrelation that are amplified the longer the time epoch.

Temporal decorrelation can vary with radar wavelength in vegetated areas, with short wavelengths often scattered, while longer wavelengths are able to penetrate leaves and reach deeper into the canopy (Askne *et al.,* 1997). Sensors operating in the C-Band (5.3GHz; 5.6cm wavelength) typically experience relatively low levels of decorrelation with spatial baselines in the range of 0-2km and revisit times of approximately 20-40 days. In view of that, low decorrelation is to be expected in urban and rocky environments, whilst expanses distinguished by water, snow, agricultural fields or vegetation are habitually hampered by noise (Rosen *et al.,* 2000).

2.4.5.3 Orbital Inaccuracies

The predicted orbits (state vectors) of a satellite platform are commonly accurate to a few meters. However, even these relatively small inaccuracies can result in errors in the image, which appear in the form of a phase slope (Zebker *et al.,* 1994). Precise orbit determination utilizes satellite tracking data and models in addition to dynamical and gravity models to reduce the error to the order of a few centimetres to try and negate orbital effects. Precise orbit information is available for ERS and ENVISAT satellites from ESA.

2.4.5.4 Atmospheric Effects

Atmospheric effects are difficult to prevent, especially when utilizing repeat-pass interferometry. The two SAR images have not been attained concurrently, but on two different satellite passes, and as a result the condition of the atmosphere will be different. Consequently, the change in atmosphere between the two images can have a significant effect on phase that can transmit through the interferogram. Phase bias is spatially correlated but its magnitude of which does not correlate with the temporal baseline (Zebker *et al.,* 1997).

2.5 Differential Interferometric Synthetic Aperture Radar

Differential interferometric synthetic aperture radar (DInSAR) is an acknowledged remote sensing technique for measuring subtle land movement arising between two radar satellite acquisitions (Sowter *et al.,* 2013). A successful way of investigating and monitoring the temporal and spatial evolution of deformations is via an interferometry time series (Lu *et al.,* 2007). A time-series allows the study of the temporal behaviour of identified phenomena; for this to be achievable the information presented from each data pair must be associated with other acquisitions by the generation of a chronological arrangement of DInSAR interferograms (Berardino *et al.,* 2002). It has been proven as a successful and efficacious tool for the surface monitoring of mineral extracted areas over wide spatial and temporal scales (Bateson *et al.,* 2015).

DInSAR estimates the transformation in surface location (both height and plan position) from interferometry and is an expansion on conventional InSAR, developed to eliminate contributions of topographic phase. Within the interferogram, signal due to deformation and topography are present, DInSAR enables the subtraction of topographic phase from the interferogram. It is implemented as either two-pass or three-pass interferometry; two-

pass involves a single SAR interferogram and a replicated interferogram produced from a DEM, whereas three-pass involves two SAR interferograms. Two-pass DInSAR has some advantages over three-pass: explicitly, phase noise associated with differencing is minimized; atmospheric phase error is eradicated for the topographic interferogram; there is no potential for unknown deformation events polluting the topographic interferogram; possible decorrelation problems are lessened; and only a singular interferogram requires unwrapping (Leighton, 2010). DInSAR is implemented by differencing coherent combinations of interferograms (Massonnet *et al.,* 1993).

2.5.1 DInSAR Limitations

Differential InSAR has become a significant operational tool for the monitoring and analysis of surface displacements; nevertheless it still has some noteworthy limitations. Many of the limitations of DInSAR are associated with the limitations of conventional InSAR (Chapter 2.4.5) because noise effects present in the interferogram still remain in differential phase.

2.5.1.1 Double Differencing

Differential InSAR is effectively a double-differencing procedure; specifically, interferograms are created by the difference of SAR phase, from which differential interferograms are formed via the difference of two interferograms. Differencing techniques suffer as there are a variety of noise sources present; any error apparent in each interferogram is amassed and transmitted onto the differential phase.

2.5.1.2 Atmospheric Artefacts

It has been postulated that atmospheric contributions are the largest source of error (Massonnet & Rabaute, 1993; Hanssen & Feijt, 1997). Pressure, temperature and humidity can all vary spanning the period of SAR acquisitions, which can increase or delay the radar signal's velocity. This results in noise or phase screens which exhibit as a phase ramp in the interferogram. Consequently when differential phase is transformed into height, the additional fringes produced can result in an unquantifiable elevation error.

The atmospheric layers that cause the largest sources of error are those at the top and bottom, the ionosphere and troposphere respectively. When a radar signal propagates through the ionosphere, velocity tends to be accelerated. Electron density across the ionosphere can fluctuate extensively and the zenith ionospheric range error is

proportionate to the total electron content (Ding *et al.,* 2008). Phase error can be up to 28mm for C-band sensors (up to half a radar wavelength in magnitude) (Hanssen, 2001). Signal propagation through the troposphere is delayed owing to humidity, temperature and pressure. The phase error is spatially variable and can be correlated with topographic height. The errors associated with water vapour are considerably bigger in magnitude to those artefacts caused by fluctuations in pressure and temperature (Zebker *et al.,* 1997). There have been a number of attempts to mitigate atmospheric effects, for example utilizing external data such as satellite water vapour products (such as those from MERIS and MODIS), ground meteorological observations, GPS data and results from numerical meteorological modelling (Ding *et al*., 2008). Progress has been made in this area but more research is necessary to develop more effective techniques.

2.5.1.3 Phase Unwrapping

To utilize phase measurements in both InSAR and DInSAR, unwrapping is required at some stage. Figure 2.13 displays the relationship between the modulo wrapped phase and the absolute unwrapped phase. Interferometric phase is only known in modulo 2π, consequentially to determine absolute phase an integer of 2π cycles has to be added. Figure 2.13a displays the wrapped phase in a set interferogram, with 'sawtooth' jumps of 2π being evident, while Figure 2.13b (assuming no sources of discontinuities or noise) shows the smooth reconstructed phase once unwrapped.

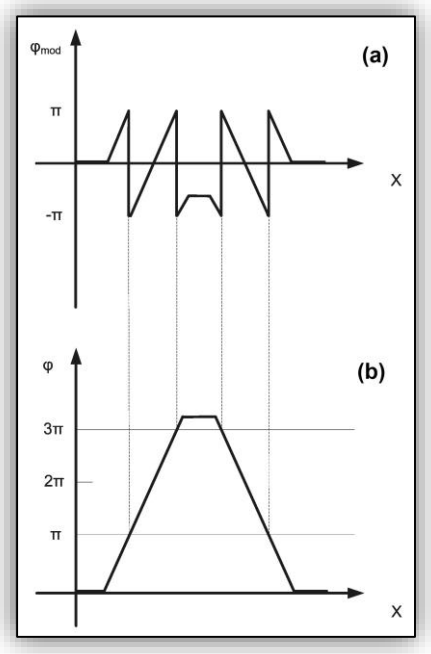


Figure 2.13: *Relationship between modulo phase and absolute phase where (a) represents wrapped modulo 2π interferometric phase and (b) unwrapped reconstructed unambiguous phase (Leighton, 2010).*

Unwrapping is computationally the most problematic task during DInSAR processing which stems from general complications in signal processing. Continuous, real signals have to be sampled and transformed to digital signals for computational purposes and an adequate sampling rate is mandatory if the original signal is to be characterised satisfactorily. When signals are reconstructed back to the original continuous data form from the discrete samples, reconstruction will be successful providing there are no errors, the data is complete and the sampling rate was high enough. However, in reality the signal cannot be precisely reconstructed resulting in erroneous phase unwrapping in some interferograms (Ghiglia & Pritt, 1998). The successful execution of phase unwrapping algorithms depends on two facets; the interferometric fringe spacing and the signal to noise ratio of the interferogram. Furthermore, poor coherence, temporal decorrelation, large perpendicular baselines, discontinuities and atmospheric phase all exacerbate phase unwrapping complications (Zebker *et al.,* 1994).

2.5.2 DInSAR Philosophies

There are at present two central categories of multi-temporal DInSAR techniques, persistent scatterer and small baseline methods. The naming of these categories is somewhat inconsistent with persistent scatterer referring to the nature of pixel identified, whereas small baseline denotes the interferogram formation procedure.

2.5.2.1 Persistent Scatterer

Orthodox InSAR has been proven to be an effective method for monitoring ground deformation over a variety of landscapes and terrains. However in many scenes, especially over expansive areas, there are large portions where the signal decorrelates, therefore making measurement impossible. Persistent Scatterer Interferometry (PSI) negates this impediment by detecting resolution elements whose echo is dictated by a singular scatterer in a series of interferograms. If this return is dominated by a singular scatterer that is brighter than the background scatterers, the variance of the echo is potentially small enough to enable the effective extraction of the causal deformation signal. Additionally, discrepancies in squint or look angle has little effect on this variation. This type of pixel is the target of persistent scatterer techniques (Hooper *et al.,* 2007).

It has been established that small man-made structures remain highly correlated over extended periods of time; utilizing this information, the persistent scatterers technique (Ferretti *et al.,* 2001) proposes a method to maximise the number of acquisitions used. It allows the inception of a DInSAR interferogram for every data acquisition (pertaining to a

common master image) regardless of whether the baseline is large, or bigger than the critical baseline. As a result, it overcomes baseline decorrelation effects by using all of the available data; however, it comes with the sacrifice of imaged pixel density. For these interferograms only pointwise information can be presented because only the targets that exhibited high coherence values are utilized and their density can be low in many regions, particularly in non-urban areas (Usai, 2000).

PS analyses are based on phase dispersion, conducted on full resolution stable scatterers to disseminate the topographic, atmospheric and deformation components; with the stability of the radar response being a necessary assumption. PS techniques, such as Interferometric Point Target Analysis (IPTA) (Werner *et al.,* 2003) and Spatio-Temporal Unwrapping Network (STUN) (Kampes & Adam, 2006), are particularly suited to deformation mapping on full resolution data, i.e. to single look data because they assume a predominant scattering mechanism and are dependent on deformation measurements on a spatial grid of amplitude stable points. Consequently, PS techniques are effective for monitoring local regions where the movement of individual buildings can be identified (Casu, 2009).

2.5.2.2 Small Baseline

For pixels that do not encompass a dominant scatterer, frequently the deformation signal is concealed by the phase variation due to decorrelation. To overcome this limitation interferograms can be formed over short temporal ranges, on top of restricting the spatial baseline and deviations in squint and look angle. Effective control of these elements minimizes decorrelation so that the fundamental signal is still detectable. In addition, discarding non-overlapping Doppler frequencies in azimuth and spectral filtering in range helps to further negate decorrelation (Gatelli *et al.,* 1994). The targets of small baseline methods are those that when filtered, minimally decorrelate and can be denoted to as slowly-decorrelating filtered phase pixels (SDFP) (Hooper, 2008).

Small Baseline techniques, conversely to PS, are not appropriate for the recognition of small scale local deformation, for example buildings enduring structural stress (Berardino *et al.,* 2002). The scattering is postulated to be disseminated within the resolution pixel with spatial multilooking executed to intensify phase stability. As a result, the spatial resolution is degraded in comparison to PS analysis and consequently small baseline approaches are more suited to analysis of spatially correlated deformation over wider expanses (Cascini *et al.,* 2010).

2.6 Small Baseline Subset (SBAS)

The Small Baseline Subset (SBAS) algorithm was developed and established by Berardino *et al.* (2002) and has since shown a proficiency to identify and scrutinise deformation phenomena in a multiplicity of application areas. A substantial amount of this work has taken advantage of the wide-ranging European Remote Sensing (ERS) SAR data (Lanari *et al.,* 2007a). The elementary SBAS algorithm is tuned for the analysis of broad spatial scale displacements, with a comparatively low spatial resolution by the use of multi-look (low-pass filtered) DInSAR interferograms (Rosen *et al.,* 2000).

The European Remote Sensing satellites SAR acquisitions are frequently distributed in Small Baseline Subsets, which are separated by larger baselines and therefore only a single time series can be computed for each subset (Lundgren *et al.,* 2001). In addition, the spatial coverage of areas is poorly temporally sampled and so differing subsets cannot be directly linked. These amalgamate in a constraining limitation that the exploitation of all the available acquisitions into a singular overall deformation time series cannot be fabricated (Berardino *et al.,* 2002). The SBAS approach extend the work of Lundgren *et al.* (2001) and Usai (2001) to the case of several small baseline acquisition subsets by means of an effective combination of all the available small baseline interferograms. The algorithm initially identifies a selection of pixels that remain coherent throughout the stack of images, in which noise effects on these pixels can supposed to be negligible. Once identified, the deformation signal component can be sequestered away from detrimental signal constituents, such as atmospheric and topographic artefacts. To achieve this, the characteristics of these patterns are exploited. More specifically the interferometric phase element associated with topographic artefacts is correlated with the spatial baseline vector of the interferogram arrangement (explicitly the perpendicular baseline component pertaining to the radar line of sight). In addition, atmospheric phase signals are poorly correlated in time but highly correlated in space (Ferretti *et al.,* 2000). Considering and utilizing these characteristics, the SBAS algorithm implements an estimation of the unwanted signals, which are then filtered out from the quantified interferometric phase, consequently permitting the construction of the deformation time series (Lanari *et al.,* 2007a).

The SBAS technique meets two fundamental requirements: to proliferate the temporal sampling rate by utilizing all of the data attained in the different small baseline subsets and to safeguard the competences of the system to deliver spatially dense deformation outputs, the latter being a fundamental issue of conventional DInSAR interferometry.

2.6.1 Methodology

The initial SBAS procedure entails the selection of SAR image pairs utilized to produce the interferograms; they are characterized by low temporal and spatial separation (baseline) between orbital revisits to negate the noise effects (decorrelation) (Zebker & Villasenor, 1992). Consequently, this allows for the preservation of the temporal and spatial coherence characteristics of the computed interferograms by means of a complex multilooking (averaging) procedure, from the designated SAR data pairs. Phase unwrapping is computed via the minimum cost flow algorithm (Costantini & Rosen, 1999) that is incorporated with a regional growing process to ameliorate the performance in expanses with a low signal to noise ratio. Phase unwrapping retrieves the unwrapped (original) phase signals from the modulo-2π wrapped (restricted) phases computed directly from the interferograms. The fundamental component of the SBAS methodology is the inversion of the unwrapped interferograms to retrieve the deformation time series; this is achieved by implementing the Singular Value Decomposition method.

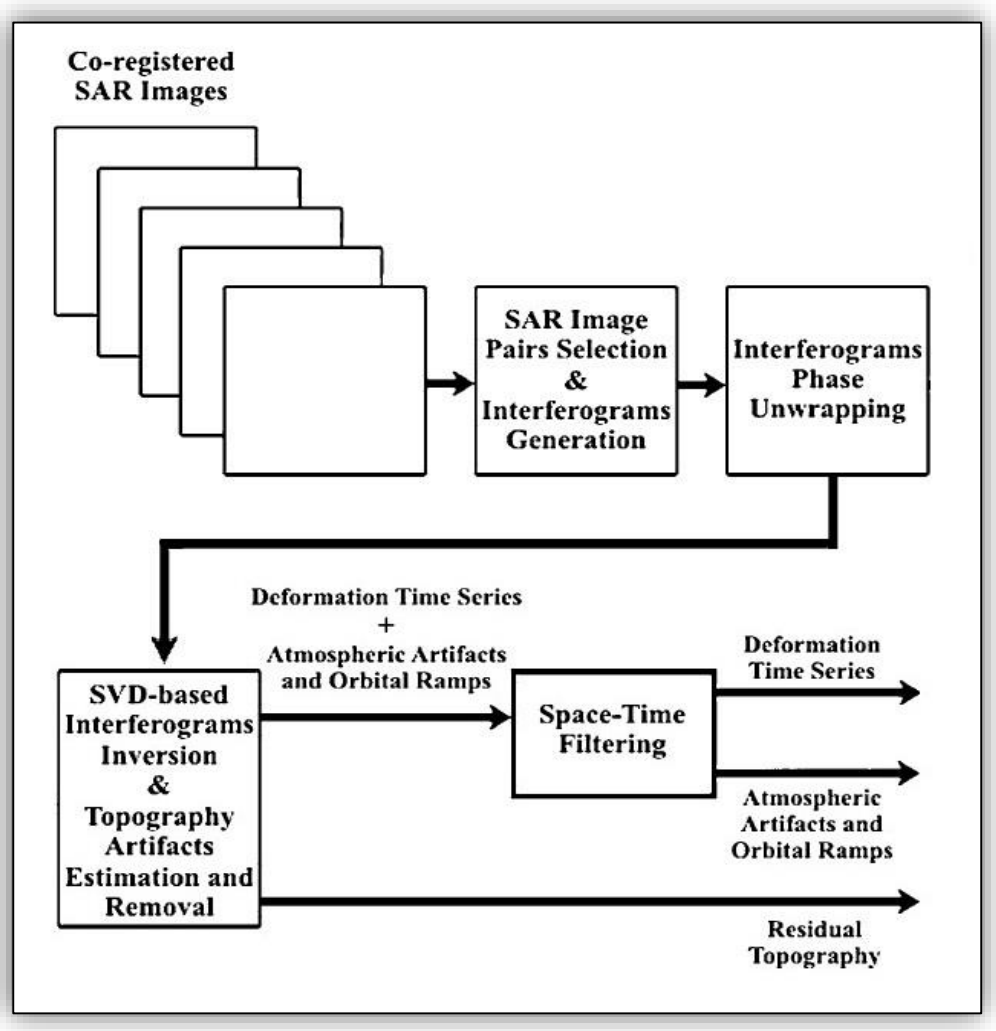


Figure 2.14: *Block diagram of the SBAS algorithm (Lanari et al., 2007a).*

This enables the information available to be easily merged through the computed interferograms. The final stage of the algorithm involves the identification and consequential filtering of atmospheric artefacts. They are removed by a two part process; an initial low-pass filter is applied in the two-dimensional spatial domain, which is followed by a temporal high-pass filter. Additionally, this allows for the detection of orbital ramps resulting due to imprecisions in the SAR sensors orbital information (Lanari *et al.,* 2007b). Figure 2.14 shows a block diagram of the SBAS algorithm. For further discussion on the SBAS technique please refer to Berardino *et al.* (2002) and Lanari *et al.* (2007a).

2.7 Intermittent Small Baseline Subset (ISBAS)

The Intermittent Small Baseline Subset (ISBAS) (Sowter *et al.,* 2013) is an amended variant of the SBAS processing algorithm, developed at the Nottingham Geospatial Institute of the University of Nottingham. The modification is designed to increase the point density of velocity outputs to address a significant limitation of DInSAR time series. DInSAR time series that span an extended period of time are limited to localities that unfailingly display high coherence for the length of the time period. Consequently, the spatial dissemination of points is frequently insufficient to depict a large-scale feature that continues over dissimilar land covers (Sowter *et al.,* 2013). As a result, only sections of subsidence patterns may be identified or they may be missed all together, which can lead to the misconception of results.

As previously mentioned the SBAS algorithm initiates with multi-looked low-resolution interferograms. Points are subsequently independently phase unwrapped on a pixel by pixel basis where the average coherence is above a fixed threshold for all of the interferograms. The ISBAS technique differs by examining each interferogram discretely, subsequently unwrapping pixels if the coherence is high in that layer only. Therefore the algorithm not only processes pixels that are coherent for the length of the time period but also pixels that are only coherent for a subset of that time epoch. As a result, it allows for a greater spatial coverage and can improve the monitoring of ground motion especially in rural localities (Bateson *et al.,* 2015).

2.7.1 Methodology

As detailed by Sowter *et al.* (2013), equation 2.7 displays the calculation solved at each locality in the multi-looked master image. If *(i,j)* are the row and column coordinates of the

point in the image, the linear velocity V_{ij} and height error δh_{ij} at each point can be estimated:

$$\Phi_{ij} = \frac{4\pi}{\lambda}\left(\delta t_k V_{ij} + \frac{B_{\perp}^{ijk}}{R_{ij} sin\theta_{ij}}\delta h_{ij}\right) \quad (2.7)$$

where Φ_{ijk} is the unwrapped interferogram phase for the kth interferogram, λ is the radar wavelength, δt_k is the time difference, $B^{ijk}{}_{\perp}$ is the perpendicular baseline, R_{ij} is the slant-range to the target and θ_{ij} is the incidence angle of the radar with the gravity normal.

There are explicit conditions on the choice of points *(i,j)* and layers *(k)*. For any point only those layers that display high coherence (i.e. have an unwrapped phase) are utilized, the number used, *m*, will fluctuate from point to point. In addition, only point coordinates where $m > M$, when *M* is a set threshold are utilized in the analysis. The value assigned to this threshold is dependent on a trade-off between two criteria: the minimization of *M* to increase the spatial density of points and the maximization of *M* to minimize the uncertainty in the solution. For example, setting a high threshold of *M*, close to the number of differential interferograms would produce a result similar to the original SBAS algorithm and consequently would not increase the density of points. Reducing this threshold improves the count and distribution of points albeit, at the expense of certainty.

2.8 Research Motivations

2.8.1 ISBAS Proficiency

The ISBAS algorithm has shown good results, increasing the point density of ground velocities over regions largely dominated by rural land covers. It has been used to determine surface movements in various application areas including; coal extraction in the UK (Sowter *et al.,* 2013; Novellino *et al.,* 2014a; Bateson *et al.,* 2015), land sliding in Italy (Novellino *et al.,* 2014b) and elevation changes associated with blanket peat in Wales (Cigna *et al.,* 2014). North Holland is largely a rural landscape that contains a mixture of different land covers including dunes, forests, agricultural land and beaches. There are also some expanses of urban land cover making the area an optimal study site in which to further test the density of point velocities an ISBAS analysis can achieve.

Ground truth often poses a significant difficulty in the validation of DInSAR products. Over many locations there is simply no ground truth with which to validate products to within the

desired precision. The ISBAS algorithm has previously been validated with respect to geology, where upward ground motion has aligned with coal measures. However, whilst this provides a spatial validation there is a desire for a more quantitative validation of ISBAS products. A geological validation cannot corroborate the rates of ground motion, observed and therefore there remains ambiguity and uncertainty around the algorithms performance. Data collated from national precision levelling campaigns that construct the Dutch ordinance level are available for North Holland, hereby providing a reference to determine the accuracy of ISBAS products. The processing of North Holland will not only increase the understanding how gas extraction has affected the landscape, but will further confirm the ability of the state-of-the-art ISBAS algorithm for deformation mapping over mineral extracted areas.

2.8.2 Terrafirma Validation Project

DInSAR analysis has been previously been used to monitor land movement in North Holland during the Terrafirma validation project (TVP) (Crosetto *et al.,* 2008). Processing was split into two sites; Amsterdam, investigating subsidence principally induced by tunnelling in the construction of a metro tunnel, and Alkmaar, investigating subsidence triggered by natural gas production. Results were validated with regard to tachymeter data and levelling benchmarks respectively.

Terrafirma was an ESA Global Monitoring for Environment and Security (GMES) service element programme, providing a pan European ground motion hazard information service, based upon PSI. The Terrafirma validation project ran within Terrafirma Stage 2 and was a significant PSI validation exercise of four Operational Service Providers (OSPs). OSPs are commercial companies that produce and provide terrain motion information derived from InSAR. The products delineate surface motion, for example subsidence resulting from tunnelling, crustal deformation or mining. The software used by the companies is frequently developed in-house, the processing algorithms are rarely divulged and end users are often not cognisant of any processing specifics or complications. Products supplied by different OSPs are expected to be at least comparable, if not compatible and technically conformed to established standards. The principle directive of the project was to validate motion data products via a Product Validation Workgroup (PVW) which brought together national geodetic organisations, commercial radar remote sensing companies, government research institutions and end users to examine the consistency and exactitude of PSI motion monitoring. Not only can we compare between ISBAS products

and levelling, the findings of the TVP affords a unique opportunity to compare between ISBAS and PSI products.

2.9 Summary

Several themes pertinent to this thesis have been examined, beginning with Radar, SLAR and SAR. This logically progresses to an overview of InSAR and DInSAR, followed by a detailed description of the Small Baseline Subset (SBAS) and Intermittent Small Baseline Subset (ISBAS) algorithms. The chapter concludes with elucidation of the research motivations for this thesis.

3 North Holland

3.1 Geography

The province of North Holland (Noord-Holland) is located toward the North-West of the Netherlands at 52°40'N 4°50'E (Figure 3.1). It is predominantly a broad peninsula positioned between the North Sea to the West, Wadden Sea to the North and Ijsselmeer and Markermeer lakes, both to the East. More than half of the 2 671 km^2 province is situated below sea level on reclaimed polder land. North Holland is one of 12 provinces that make up the Netherlands and has a population of 2,725,500 with a population density of 1020 people/km^2, the second highest in the Netherlands (Noord-Holland, 2015).

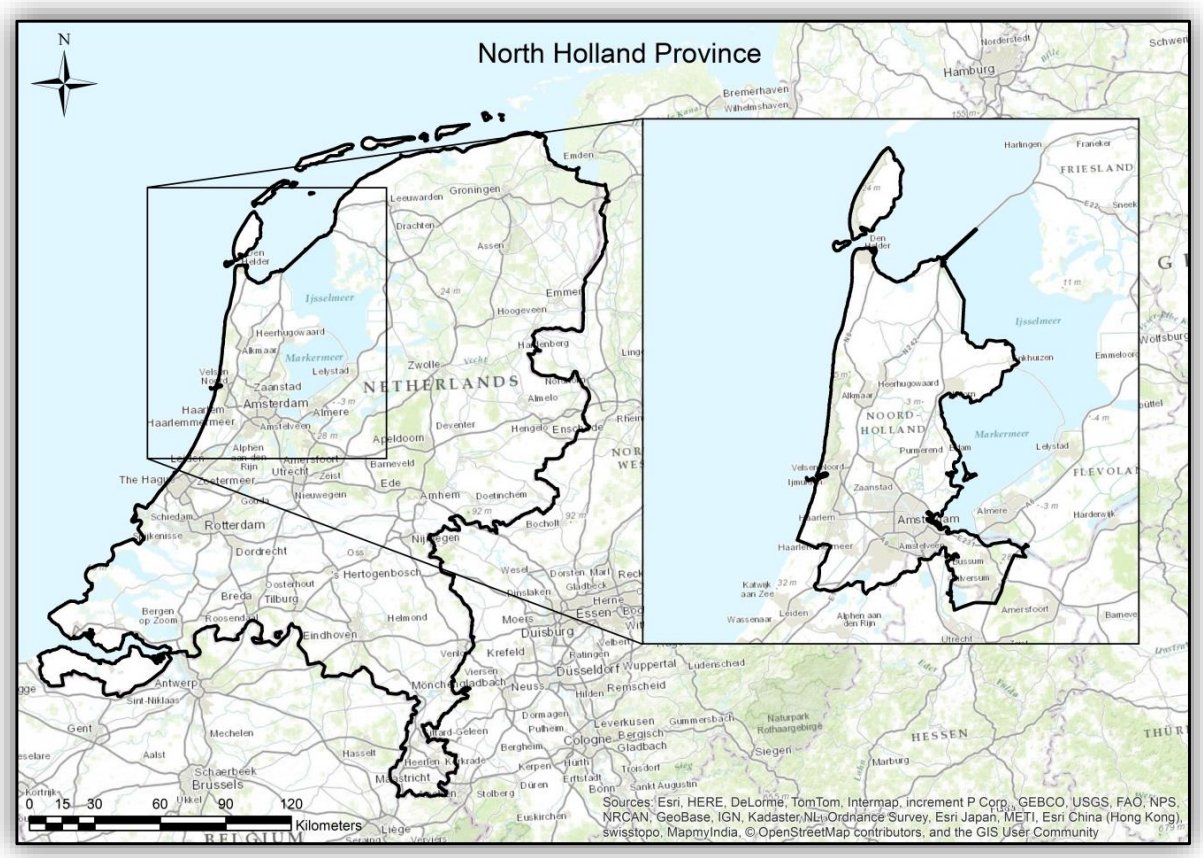


Figure 3.1: *The Netherlands and North Holland province.*

3.2 Land Cover

North Holland contains a mixture of land covers including agricultural land, sand dunes, urban districts, water bodies and woodland (Figure 3.2). Agriculture dominates the land cover in the province, with the total utilised agricultural area amounting to 1284km^2. Of this

area 55% is utilized for livestock grazing, 21% for crop cultivation and 17% for specialist horticulture. The best agricultural land is found in reclaimed polders, with much of the other land comprised of poor soils where only grass is economically viable to grow. The principle crops grown are potatoes, rye, barley, sugar beets and triticale (Statistics Netherlands, 2015). The West coast is characterised by a long thin belt of sand dunes and beaches that protect the province from the North Sea. Woodland cover exists behind sections of sand dunes on the West coast, to the West of Bergen and Castricum.
The area has some pockets of urban cover, notably with the cities of Amsterdam, Alkmaar, Bergen, Purmerend and Heerhugowaard and the towns of Hoorn and Heiloo.

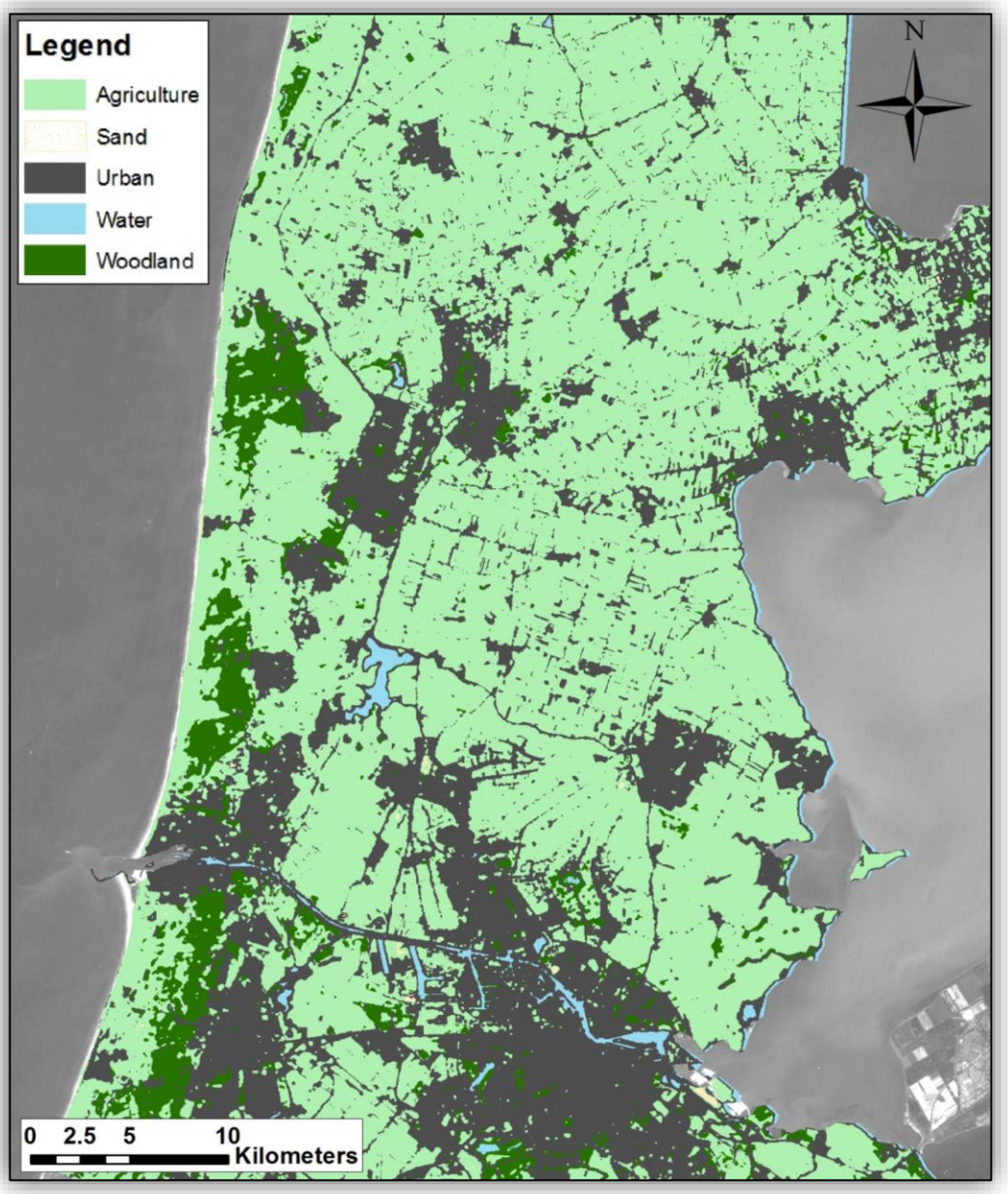


Figure 3.2: *Land cover classification of North Holland, derived from Landsat 7 ETM+ imagery (24th August 2000).*

3.3 Geological Setting

The oldest rocks that exist in North Holland form the base rock of the province, which stem from the Carboniferous period approximately 355 million years ago, the depth of which can be greater than 6000m (Duin *et al.,* 2006). The succeeding layer above this is from the Permian era, approximately 250 million years ago, which is known for its natural gas reserves, with rock units from the Trias era, which also include natural gas, successively laid overlaid. Figure 3.3 displays the geological time scale of the Netherlands and adjacent continental shelf indicating the presence of hydrocarbons (Deltawerken, 2004).

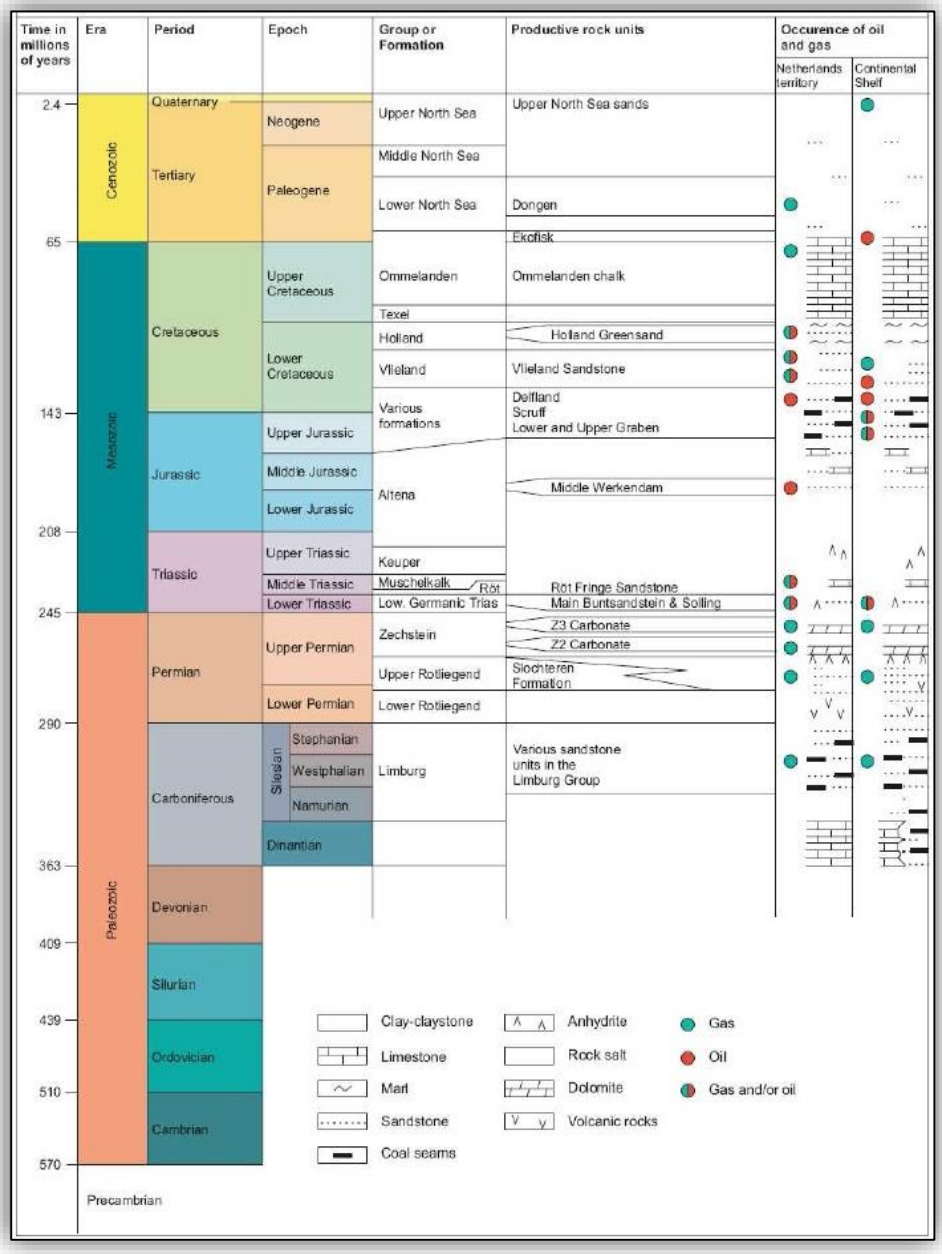


Figure 3.3: *Geological time scale with composite stratigraphic column of the Netherlands and the Continental Shelf (TNO, 2012).*

3.4 Gas Production

Exploration for hydrocarbons began in 1962 when the Amoco Netherlands Petroleum Company commenced drilling. The Amoco group discovered the Heiloo and Schermer reservoirs in 1964; however in November 1965 the Dutch government suspended drilling awaiting an enactment of exploration legislation, which arrived on May 3rd 1967 when the Minerals Exploration Act was published. It was not until September 1972 that the first field, Bergermeer, came on stream due legislative issues and environmental protest groups delaying subsequent hydrocarbon production. This was swiftly followed by Groet in 1974, Bergen in 1978 and Schermer and Alkmaar in 1979 (van Lith, 1983).

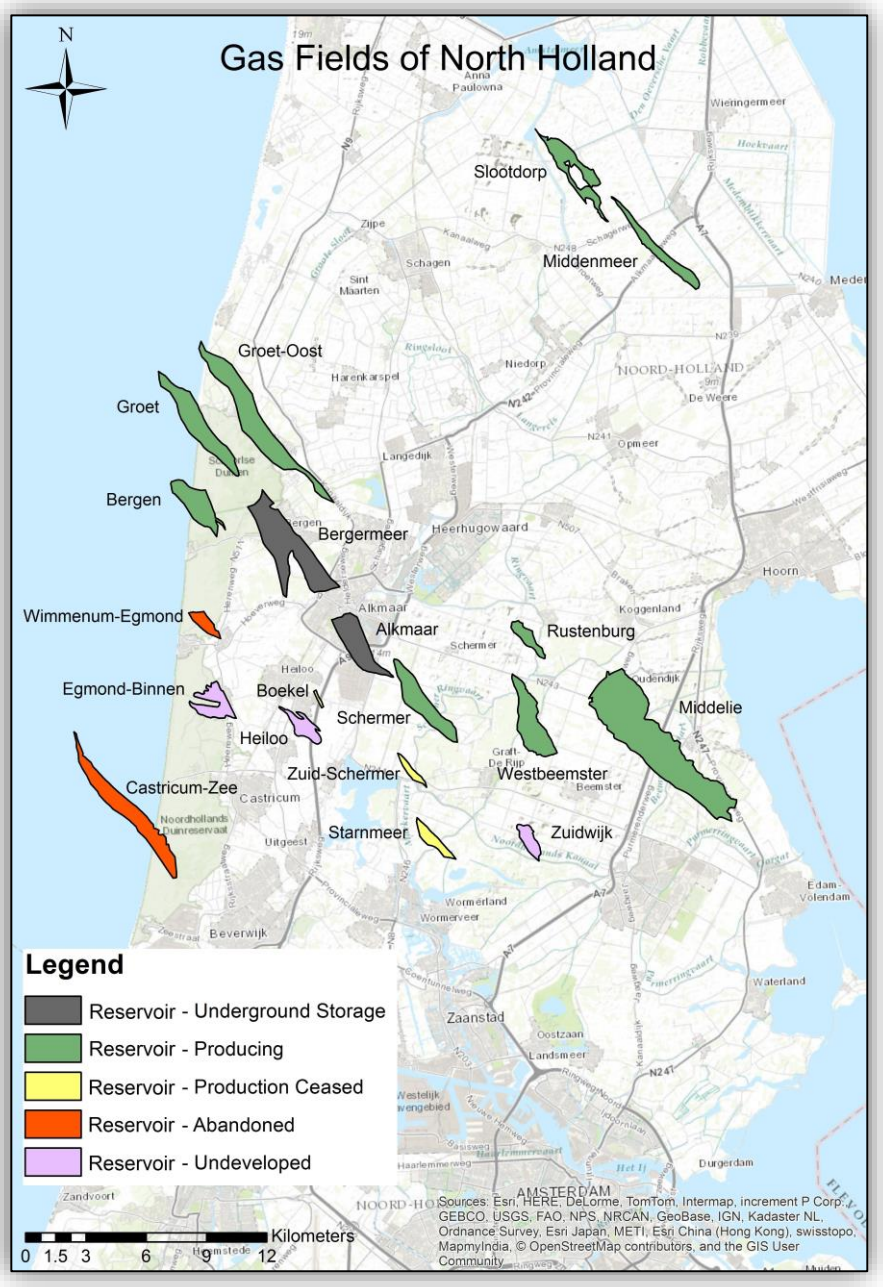


Figure 3.4: *The location and status of reservoirs in the North Holland.*

Reservoir	*Epoch*	*Group or Formation*	*Productive Rock Units*	*Status*	*Discovery Date*	*Production Commenced*
Alkmaar	Upper Permian	Zechstein	Z3 Carbonate Member	Underground Gas Storage	1965	01/09/1979
Bergen	Lower Triassic	Lower Germanic Triassic	Main Buntsandstein Subgroup	Producing	1965	13/10/1978
Bergermeer	Upper Permian	Upper Rotliegend Group	Slochteren Formation	Underground Gas Storage	1969	01/09/1972
Boekel	Lower Triassic	Lower Germanic Triassic	Main Buntsandstein Subgroup	Production Ceased	2006	01/08/2006
Castricum-Zee	Lower Triassic	Lower Germanic Triassic	Main Buntsandstein Subgroup	Abandoned	2000	01/07/2001
Egmond-Binnen	Lower Triassic	Lower Germanic Triassic	Main Buntsandstein Subgroup	Undeveloped	1997	-
Groet	Upper Permian	Upper Rotliegend	Slochteren Formation	Producing	1965	01/01/1974
Groet-Oost	Upper Permian	Upper Rotliegend	Slochteren Formation	Producing	2006	01/02/2006
Heiloo	Lower Triassic	Lower Germanic Triassic	Main Buntsandstein Subgroup	Undeveloped	1965	-
Middelie	Upper Permian	Zechstein	Z3 Carbonate Member	Producing	1964	01/08/1975
Middenmeer	Upper Permian	Zechstein	Z2 Carbonate Member	Producing	1975	01/07/1977
Rustenburg	Lower Triassic	Lower Germanic Triassic	Main Buntsandstein Subgroup	Producing	1977	01/09/2009
Schermer	Upper Permian	Zechstein	Z3 Carbonate Member	Producing	1964	01/09/1979
Slootdorp	Upper Permian	Zechstein Group	Z3 Carbonate Member	Producing	1965	01/07/1977
Starnmeer	Upper Permian	Zechstein	Z3 Carbonate Member	Production Ceased	1975	01/11/2001
Westbeemster	Upper Permian	Upper Rotliegend Group	Slochteren Formation	Producing	1993	01/11/2007
Wimmenum-Egmond	Lower Triassic	Lower Germanic Triassic	Main Buntsandstein Subgroup	Abandoned	1964	01/01/1984
Zuid-Schermer	Upper Permian	Zechstein	Z3 Carbonate Member	Production Ceased	1997	01/11/2001
Zuidwijk				Undeveloped	2012	-

Table 3.1: *Background information of the reservoirs in North Holland (NLOG, 2015).*

Nineteen onshore gas reservoirs are orientated in a North West – South East direction, with the majority (17) located in an approximately 30km stretch. They are of varying status; two are abandoned, production has ceased at three, two have been converted into underground gas storage facilities, while the remaining nine are still producing. Figure 3.4 displays the location and status of all the reservoirs while Table 3.1 provides relevant individual details. Gas is produced from reservoir rocks of the Lower Triassic Main Buntsandstein Subgroup (Bunter), Upper Permian Zechstein 3 Carbonate Member (Platten dolomite) and Upper Permian Rotliegend Slochteren Formation from a depth exceeding 2000m. Perhaps the most important reservoir in North Holland, and elsewhere in the Netherlands, is the Rotliegend formation. The thickness is on the order of 200m to 270m, with a predominantly Aeolian origin. It is often possible to divide up the layer into three sections: a low porosity basal unit, a high porosity middle unit and a low porosity upper unit.

3.5 Subsidence

Gas production over the province has caused some significant effects on the landscape, with subsidence evident at the surface. Subsidence is defined by Nagel (2001:p.3) as the "movement of surface strata in response to a loss of underground support". The diminution of support can be attributed to hydrocarbon removal, which can trigger reservoir compaction. The most prevalent and notable consequence is the downward vertical motion of the surface, although in some cases horizontal motion can be just as significant. The subsidence bowls produced from compaction are generally assumed to extend laterally approximately as far as the depth at which the reservoir is situated (Muntendam-Bos *et al.,* 2008).

3.5.1 Reservoir Compaction

To understand the cause(s) and development of surface subsidence, the geomechanical behaviour of subsurface rocks is of importance. Reservoir rocks are composite materials and therefore include a pore volume, which influences and controls their yield stresses and elastic response. Classical work from Terzaghi (1923) communicated that the application of pore pressure to porous elastic earth constituents prompts an apparent increase of volume similar in magnitude, but inverted in sign, to the volume change produced by a confining pressure. These findings were echoed latter by various other investigators. Biot (1941) pioneered the theory of poroelasticity which, in the context of

hydrocarbon reservoirs, conjectures that reservoir rocks contract when pore pressures decrease. When gas is withdrawn the land shifts horizontally towards and vertically down to the region of maximum pressure decline, habitually at the reservoir gravity centre where the wells are congregated. Reservoirs are in equilibrium preceding to the production of hydrocarbons; for compaction to transpire there must be an alteration in the energy of the collective reservoir and overburden system. Without such an alteration in energy, the reservoir will remain in equilibrium and reservoir compaction does not transpire. An increase in effective stress that acts upon the rock matrix is the energy that triggers compaction. Increases in effective stress are often directly proportional to the reduction of reservoir pore pressure, which transpires during production. The rock compacts until a new state of equilibrium is achieved with a new effective stress (Nagel, 2001).

Reservoir compaction or the thinning of reservoir layers, is regarded as the predominant reason for surface subsidence in such cases. It is governed by three principle parameters (excluding purely chemical effects, for example dissolution or thermal effects) and can be thought of as a function of increasing effective stress, reservoir rock compressibility and reservoir thickness:

$$\Delta t = \Delta \sigma_v^1 \, x \, c \, x \, h \qquad (3.1)$$

where Δt is the change in reservoir thickness, $\Delta \sigma_v^1$ is the change in vertical effective stress, c is compressibility and h is the original reservoir thickness. Whilst effective stress can be altered and changed, reservoir rock compressibility and reservoir thickness are intrinsic facets of the reservoir that generally cannot be changed. They define the limits of maximum reservoir compaction and archetypally work in opposed ways to each other. For example, similar compaction rates can be found from thin reservoirs that are highly compactable and from thick less compactable formations. Reservoir rock compressibility is considered the most challenging of the three primary parameters to measure accurately. It can vary greatly, by on the order of three to four magnitudes, depending on the stratum (Chilingarian *et al.,* 1983). A number of parameters delineate rock compressibility, including the constituent minerals that comprise the rock mass, the degree of mineral alteration or decomposition, the degree of sorting, the cementation and the rock porosity. Porosity is often a significant factor to gauge potential compression, as there is a preponderance of highly compressible reservoirs that have porosities higher than 30% (Nagel, 2001).

3.6 Induced Seismicity

Seismic events are a further consequence of gas production, which is concomitant with reservoir compaction. Rock masses that sustain gradual alterations in stress are putatively seismogenic, i.e. have the potential to generate earthquakes. The primary geological earthquake inducing method is via the continuous and cumulative loading of stress through tectonic plate movements. At fault boundaries this results in intense deformation in the most active earthquake zones on earth. Lower level motion also occurs towards plate interiors as tectonic plates are not entirely rigid and therefore intraplate deformation can transpire in areas such as mainland Europe (Sykes & Sbar, 1973). The cause of seismic activity can be attributed to either natural causes, for example tectonic stresses in the crust, or alternatively human influence (Vos, 2010). The Netherlands is considered an area of low seismic activity and therefore seismic events are brought about by pressure alterations associated with gas production. The causation and process of induced seismicity can frequently be related to existing tectonics and gas exploration (Mutendam-Bos *et al.,* 2008).

Induced seismicity is linked to stress alterations in the reservoir and the contiguous rock, which can be initiated by a variety of mechanisms including geochemical reactions, pore pressure variations, temperature effects and the reactivation or locking of pre-existing faults. As a result, induced seismicity patterns can vary greatly, both between different gas fields or between occurrences within the same field over time and space. Despite this unpredictability, six key tendencies need to be noted.

- *Magnitude Range:* Seismic activity in the majority of hydrocarbon fields has been limited to small and moderate events, those with a magnitude less than 4.5.
- *Production Correlation:* It is often difficult to correlate hydrocarbon production with seismicity. This is partially due to the lack of production pattern data available at many wells, but where data is available a correlation between increased production rates and elevated seismicity is rarely seen. Only a very small proportion of injection and extraction activities result in seismicity, especially events that are noticeable to the public.
- *Location:* Induced seismicity habitually occurs either directly above or directly below the reservoir.
- *Spatial Clustering:* Earthquakes have an evident propensity to form in swarms or clusters, for example around pre-existing fault lines.

- *Temporal Patterns:* Time lapses between production initiation and an increase in seismic levels has been observed in many fields. This can partly be attributed to instrumentation quality being low, as networks often increase after seismicity is observed by other networks or the populous, therefore the potential build-up of seismicity could be missed. However, a time-lapse also aligns with theoretical expectations from poroelastic modelling (Segall, 1985).
- *Faulting:* Faulting within hydrocarbon fields is controlled by the pre-existing stress field, rather than relatively small production associated stress perturbations. Production can result in the activation of existing faults as well as the development of new faults (Suckale, 2009).

It is conjectured that fluids play a pivotal role in inducing seismicity, in a variety of geological settings. Induced seismicity in hydrocarbon fields can generally be categorised as being principally associated to fluid injection or fluid extraction. It needs to be noted that in reality it is difficult to relate instances into one of these categories because of simultaneous fluid extraction (reservoir depletion) and injection (secondary recovery) (Suckale, 2009).

3.6.1 Fluid Injection

Fluid injection occurs on a large scale in hydrocarbon fields for the following reasons: secondary recovery, pressure maintenance, underground storage, to sweep fluids to producing wells or hydraulic fracturing (to provoke production by creating new fractures and thus generating new flow conduits). The artificial injection of fluids into the earth's crust can induce earthquakes and seismic activity because it increases effective stress. Pressurised fluids are inaugurated into existing fault zones which can cause fault slip to transpire that would not have occurred without anthropogenic influences (Davies *et al.,* 2013). The fluid injected moves into a pre-existing fractures and supports a portion of the normal stress equal to the pressure of the fluid. The fluid has no shear strength and as a consequence the effective normal stress and frictional resistance to movement are decreased. Figure 3.5 represents an example of a well drilled vertically into a producing layer of strata (dark grey), offset by a normal tectonic fault (black line). Compressive stresses σ_1, σ_2 and σ_3 are exerted on the fault, with σ_1 being vertical, σ_2 being horizontal (N.B. off the diagram and not shown) and σ_N represents the normal stress exerted on the fault plane. If and when fluids are transmitted towards or into a critically stressed fault (represented by the white arrows) the fault can fail. This eventuates when shear stress (*T*)

is greater than the sum of shear strength *(T_o)* and frictional stress on the fault plane *($\mu\sigma_N$)*, where μ is the coefficient of friction:

$$T > T_o + \mu\sigma_N \qquad (3.2)$$

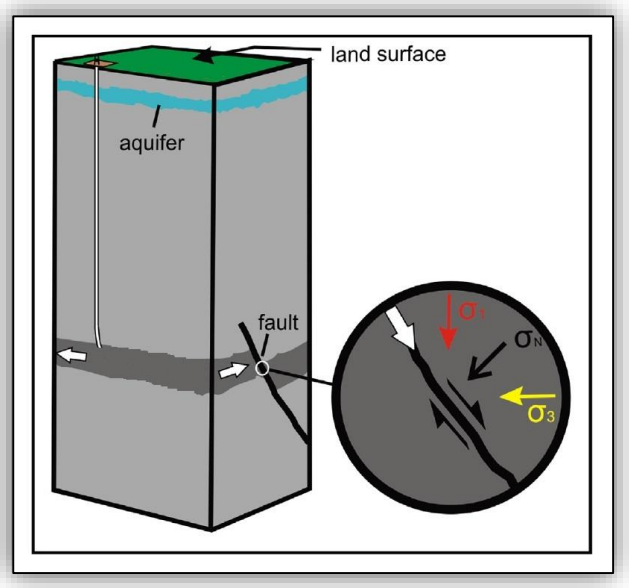


Figure 3.5: *Induced seismicity along normal fault (Davies et al., 2013).*

A Mohr stress diagram for the fault plane is depicted in Figure 3.6. A Mohr stress diagram is a means of plotting two stresses acting on a plane of unknown orientation as components of normal and shear stresses. Mohr circle 1 characterises σ_1 and σ_3 for the critically stressed fault plane preceding fluid injection, which is close to the Mohr failure envelope. During injection, the fluid pressure inside the fault zone might increase, so there is a reduction in compressive stress (σ_1 and σ_3), which shifts the Mohr circle to the left (Mohr circle 2, depicted by the red arrow) and consequently intersects the failure envelope and shear failure occurs. If this ensues over a significant interval of the fault, then felt seismicity can result (Davies *et al.,* 2013).

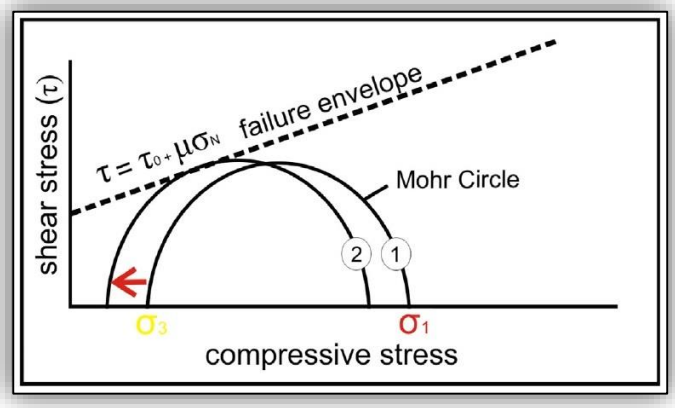


Figure 3.6: *Mohr diagram for the fault plane (Davies et al., 2013).*

3.6.2 Fluid Extraction

While the conjecture that the injection of fluid increases effective stress seems obvious, it would appear counter-intuitive that fluid extraction could result in seismicity because failure should be inhibited, as the decrease of pore pressure should, in turn, decrease effective stress. However, the effect can be significant where pre-existing faults are subjected to spatially disparate reductions in pore pressure (Pennington *et al.,* 1986; Mulders, 2003) or if pore pressure reduction results in a formerly aseismically slipping fault to seize up, whereby the accumulated energy is released in a seismic event. The consequence of fluid extraction is multifaceted and cannot solely be explained by the Mohr circle argument because poroelastic stresses must to be accounted for. As mentioned in Chapter 3.5.1 the theory of poroelasticity suggests that, in the context of hydrocarbon reservoirs, that reservoir rock contracts when pore pressures decrease. The reservoir is elastically coupled to the neighbouring rock, so as contraction occurs it stresses the surrounding crust. Consequently, this triggers the horizontal contraction of the reservoir overhead, and in certain instances induced seismicity (Suckale, 2009).

3.6.3 Fault Reactivation

Stress variations are brought about by two habitually interrelated mechanisms; pore pressure alterations and differential compaction. The consequent stress change both cause can induce seismicity via fault reactivation. A fault within a reservoir is commonly considered a weak zone or weak plane. Deformations are predominantly harboured at the weakest area of the rock matrix, either within fault zones or on fault planes. Depletion during production leads to a reduction in pore pressure which results in compaction and surface subsidence. Due to the arching effect, the overburden load on top of the compressing reservoir is reapportioned to the abutting rock at the reservoir boundary. Consequently, stress can be increased at the confines of the reservoir and the internal dividing faults, which produces rock failure and faulting. Compaction induces the downward movement of the upper confine and upward movement of the lower confine of the reservoir. With pressure differences inhomogeneous across the fault, the reservoir rocks experiencing the largest pressure decline compact more than those experiencing a lower pressure decline. This results in spatially disparate motions across the fault of the reservoir boundaries which can potentially lead to slip (Muntendam-Bos *et al.,* 2008).

3.7 Seismic Events in North Holland

A series of seismic events in the North of the Netherlands began in 1986, associated with the exploitation of a number of on-shore gas fields. Seismic events in the region are often negligible and shallow, although bigger earthquakes with a magnitude > 2.5 infrequently cause damage. There have been five notable events in the study site, four occurring in the Bergermeer reservoir and one in the Bergen reservoir (Figure 3.7 and Table 3.2).

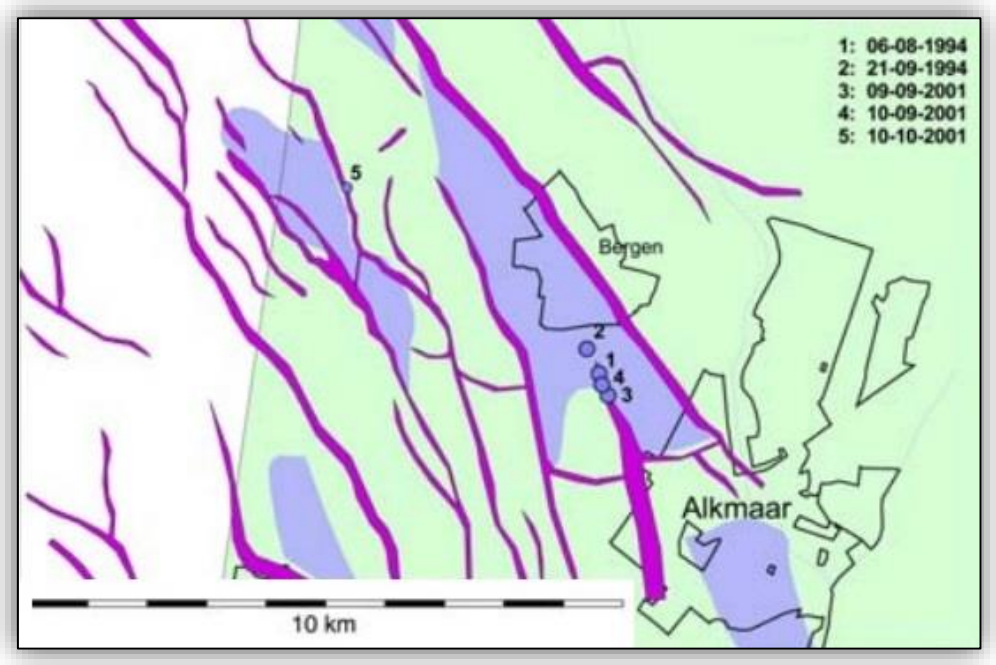


Figure 3.7: *The epicentre locations of the five earthquakes in North Holland (van Eck et al., 2006).*

	Magnitude (M_L)	***Moment (Nm)***	***Radius (m)***	***Displacement (mm)***	***Stress-drop (bar)***	***Mechanism (Strike / Dip / Rake)***
Bergermeer						
06/08/1994	3.0	4.0×10^{13}	-	-	-	-
21/09/1994	3.2	7.0×10^{13}	400	8.0	5	-
09/09/2001	3.5	1.9×10^{14}	680	7.4	2.8	130 / 66 / 73
10/09/2001	3.2	6.3×10^{13}	470	5.0	2.9	130 / 66 / 73
Bergen						
10/10/2001	2.7	1.8×10^{13}	460	1.4	0.8	-

Table 3.2: *Parameters of the seismic events in North Holland (Dost et al., 2012).*

3.7.1 Bergermeer

Four earthquakes can be related to the Bergermeer reservoir, where two events occurred in 1994 and two in 2001. The approximated deformation that occurred was relatively small, in the 5-10mm range, with the stress drop similarly low, in the 1-10 bar range, while the radius of the inferred circular fault was in the 400-800m range (Table 3.2). The four quakes were all located within a small distance from each other, along the same fracture (Figure 3.7). It is estimated that the events of 10th September 2001 were less than 205 metres North West of the quake the previous day (Haak *et al.,* 2001).

After the shocks of 1994, a network consisting of three borehole seismometers was placed in the area around Alkmaar, with a detection threshold of a magnitude 1 shock. The sequence of earthquakes is such that strong quakes are subsequently followed by smaller events, in a common aftershock pattern. For the 2001 events no other shocks were detected in the ensuing month of November and therefore it is supposed that these were separate events. The first of the 2001 events can be associated to other powerful events in the Netherlands, whereby it is noted that gas fields of North Holland are as vulnerable as the larger gas fields in the North East of the Netherlands to induced seismic

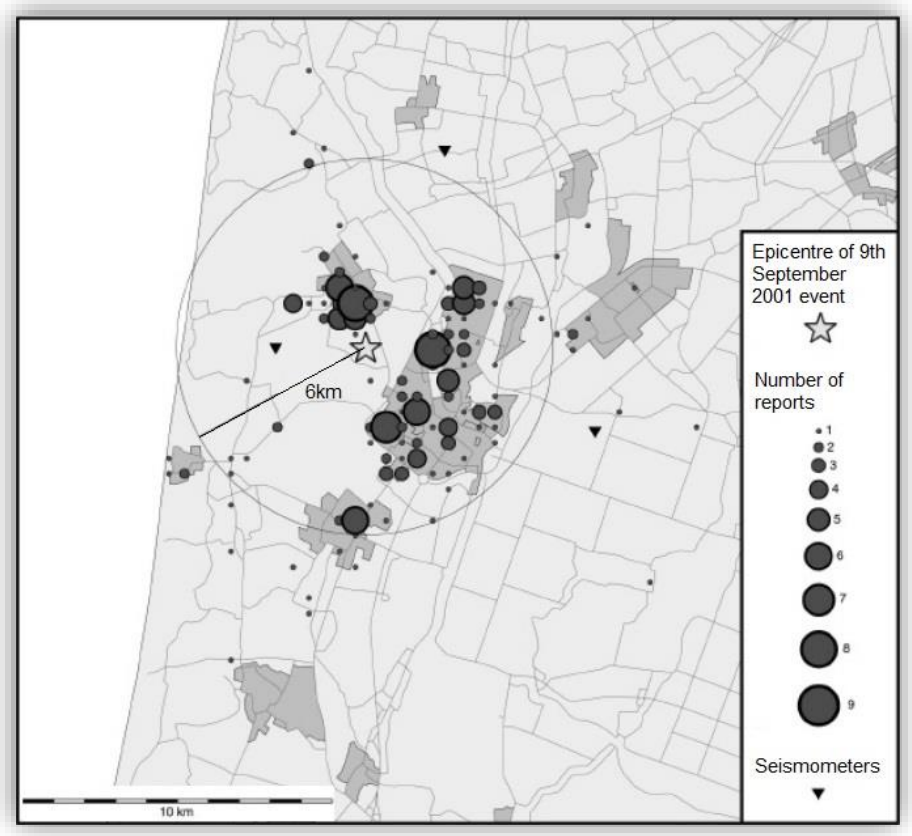


Figure 3.8: *An overview of damage reports following the September 2001 earthquakes near Alkmaar (Haak et al., 2001).*

events. It was the largest recorded in the Northern Netherlands, consequently damage was widely reported, predominantly within a 6km radius of the epicentre location at the surface (Figure 3.8). Most of the accounts of damage came from the South of Bergen and to the West of Alkmaar, closer to the epicentre.

3.7.1.1 Reservoir Geology

The Bergermeer reservoir is relatively small, measuring approximately 8km by 2km at a depth of 2100m. The Permian age, Slochteren Sandstone is a well-sorted, fine-grained aeolian sandstone. The porosity of the reservoir is largely high, that ranging from 15% to 30%, with an average of 23%. The Bergermeer reservoir lies adjacent to the Groet reservoir, on the same North West – South East narrow trending horst block, divided by a low relief saddle. Within the Bergermeer reservoir, the reservoir central fault (b) splits it into two notable fault blocks, the main high block (block 1) and a lower south block (block 2) (Figure 3.9 and Table 3.3). The caprock sealing the reservoir is in the form of Zechstein evaporites (3), which directly above is relatively thin (as shallow as 100m) due to salt flow and fault gaps. A number of listric faults penetrate the overburden (Muntendam-Bos *et al.,* 2008).

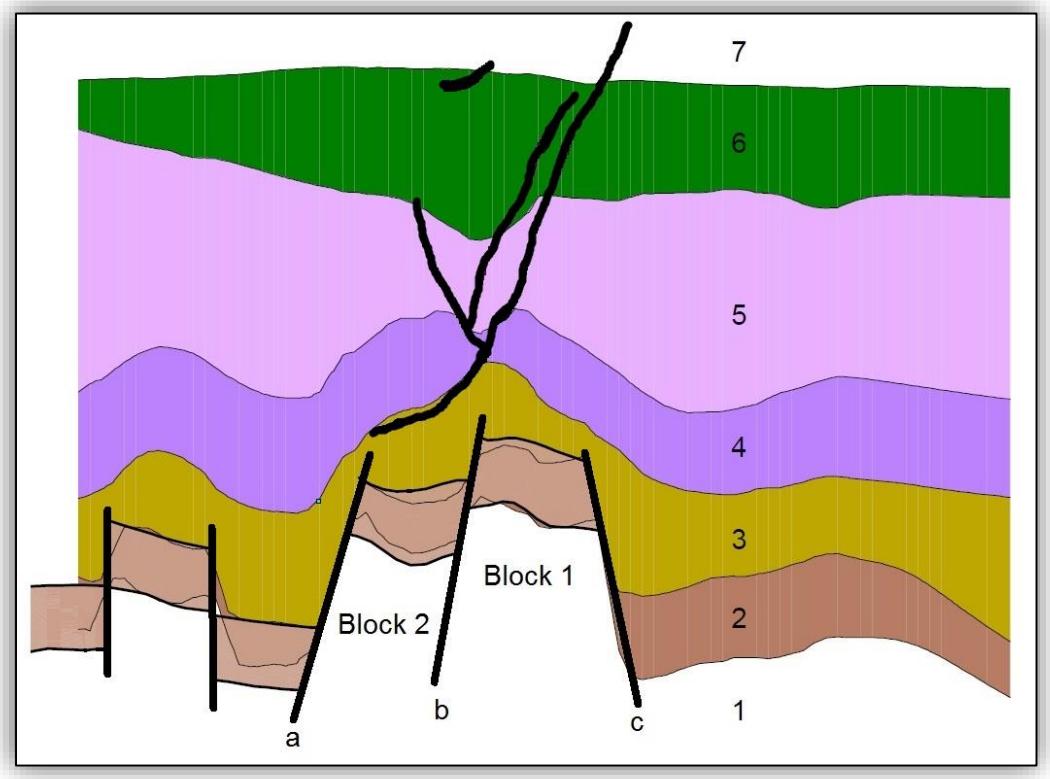


Figure 3.9: *A SW-NE geological cross section of the Bergermeer reservoir, where black lines represent faults. The geological units are defined in Table 3.3 (Muntendam-Bos et al., 2008).*

	Geomechanical Unit	Geological Unit	Average Thickness (m)
1	Base Rock	Carboniferous	-
2	Reservoir Rock	Rotliegend Slochteren Sandstone	271
3	Zechstein	Zechstein Formation	293
4	Overburden 1	Main Claystone	309
5	Overburden 2	Musschelkalk, Bunter & Keuper	525
6	Overburden 3	Vlieland Shales & Holland Marls	424
7	Overburden 4	Tertiary Rocks	838

Table 3.3: *Geological units of the Bergermeer reservoir (Muntendam-Bos et al., 2008).*

3.7.1.2 Earthquake Focal Mechanism

Haak *et al.* (2001) concluded that the focal mechanism was the same for the 1994 and 2001 events. It tallies with the direction of the extent of the fracture where the earthquakes were located. The focal mechanism was identified as a collapse alongside an inclined fracture with a scope of 130°, angle of 66° and 73° evasion. The break, located at the centre of the field, extends down to the Tertiary at an angle of 70° (Figure 3.9). Based on polarity data acquired by Haak *et al.* (2001), it was concluded that the seismic events were generated due to gas extraction because of the location of the earthquakes as well as the focal mechanism. The fracture emanated as a result of normal faulting (shear), but, due to compaction as a result of pressure reduction from gas extraction, the current process is reverse faulting (faulting), which has produced a scissor-shaped fracture. The footwall (block 1) shifts below the hanging wall (block 2), where layers of higher gas field move downward and therefore contribute to surface subsidence (Figure 3.10).

However, there is not universal agreement on the mechanism. TNO conducted a geomechanical analysis of the reservoir in 2008 (Muntendam-Bos *et al.,* 2008). The mechanism concluded by Haak *et al.,* (2001) was questioned because although a reverse re-activation of an existing normal fault is plausibly justified by differential compaction, it creates a difficulty in the geomechanical modelling of the Bergermeer reservoir. Only normal faulting was able to be modelled in an extensional stress regime.

In a more recent review of the aforementioned geomechanical modelling, conducted by Massachusetts Institute of Technology (MIT) (Hager & Toksöz, 2008), the performance of TNO's model was questioned. The TNO model did not predict reverse faulting movement

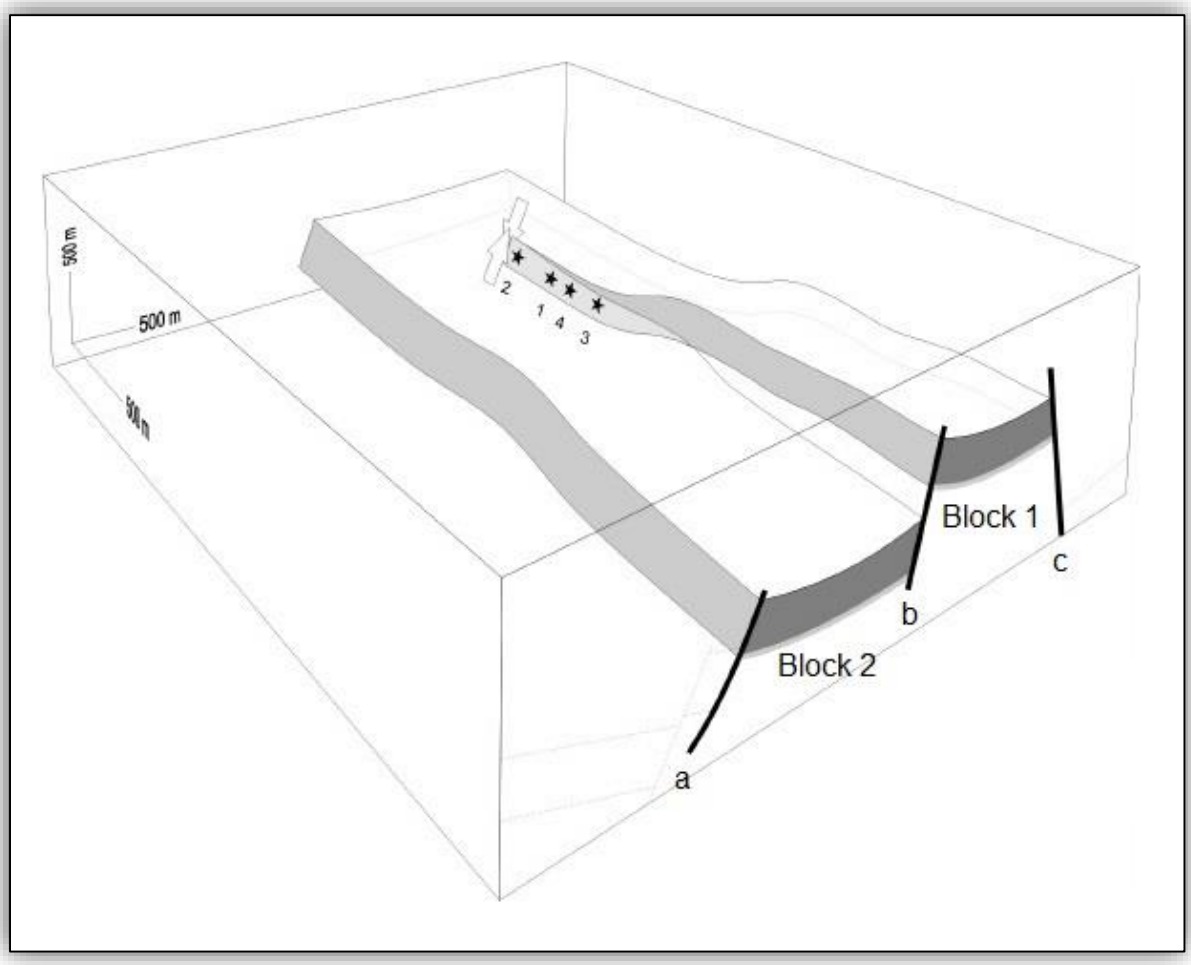


Figure 3.10: *A schematic representation of the Bergermeer central reservoir fault, with epicentre locations of the four seismic events represented by stars (Haak et al., 2001).*

that is related with differential compaction for potentially two reasons. Firstly, the model did not include the faults or other means to account for this movement where it would be anticipated to occur, explicitly the central reservoir fault (b) discontinues shortly above the Block 1 reservoir (Figure 3.9). Roest & Kuilman (1994) communicate that boundary effects are known to be substantial at the upper confine of a reservoir where non-compacting and compacting formations lie adjacent. Differential normal stresses would be generated, while shear stresses would increase on the fault plane that extends into the overlying strata (Zechstein formation), producing circumstances that encourage slip. However, in the TNO model there is an absence of a fault in the locality that is highly likely to have a reserve motion driven by reservoir compaction. Secondly, a ductile area could tolerate compaction induced shearing via the distribution of deformation over a shear zone. The Zechstein formation can be anticipated to deform in this manner because it is an evaporite, although this ductile deformation was only implemented in one out of the seven geomechanical models exhibited. Encompassing a framework (ductile region or fault) to harbour deformation in the model, reservoir compaction could produce reverse motion on

a normal fault. Furthermore, an additional limitation to note is that the geomechanical model employed by TNO presupposes a two-dimensional geometry when the structure of the area varies markedly along strike. Three dimensional disparities could be significant as slip on a particular section of the fault, potentially aseismic, can shift stress to a contiguous section of the fault, therefore magnifying the stress on the fault produced as a result of differential compaction alone.

With respect to the 2001 events, Hager & Toksöz (2008) found little reason to doubt the reverse faulting focal mechanism, but recommended that waveform inversion analysis should be conducted. The recommended study was conducted by T. Dahm and co-workers at Hamburg University. They found that their result concurred with respect to the strike and dip of the fault; however differences arose with respect to movement on the fault plane. It indicated a strike-slip movement incorporating a lesser vertical component (normal or reverse). It was concluded that further modelling would be needed to discover a more certain solution (Dost *et al.,* 2012). Differing reports and reviews may attribute differing mechanisms for the events and results from investigations are not universally conclusive. However importantly, with respect to this report, they all concur unequivocally that seismicity in the reservoir and subsidence above the reservoir can be attributed to gas production.

3.7.1.3 Underground Storage Facility

The reservoir previously contained 17 billion cubic meters of natural gas at a depth of 2100 metres, in the Lower Rotliegend Formation. It was depleted in 2006 and subsequently identified as a potential gas storage facility. The reservoir advantageously has quintessential geological characteristics for gas storage, in addition to being in a logistically ideal location, situated close to industrial centres, major cities, gas transport networks and the 235km BBL pipeline that connects the UK and Dutch gas markets (BBL, 2015).

The hazards and risks are recurrent when a UGS site is planned or proposed. Subsurface consequences are associated with effective intergranular stress alterations within the injected formation and sealing caprock, with a chance of creating new fractures which can advantageously increase the gas injectivity but can detrimentally jeopardize the integrity of the cover (Ferronato *et al.,* 2010). Additionally, existing faults in the reservoir can be reactivated, potentially inducing microseismicity (Segall & Fitzgerald, 1998). Controversially, work on the Bergermeer project was suspended in August 2011 following

a court order filed against the facility by community and environmental groups. Their claims that it would unsettle wildlife patterns, increase noise levels and increase the risk of induced seismicity were dismissed by The Council of State (Natural Gas Europe, 2012). Three independent studies conducted by TNO (Netherlands Organisation for Applied Scientific Research), MIT (Massachusetts Institute of Technology) and KNMI (Royal Netherlands Meteorological Institute) concluded that the risk of felt seismicity would not increase with respect to when gas was previously produced from the facility (TAQA, 2014).

3.7.2 Bergen

One notable seismic event can be associated with the Bergen reservoir, located to the West of Bergermeer (Figure 3.7 and Table 3.2). The quake occurred on 10th October 2001, at a depth of 4km along the North East edge fracture of the Bergveld. No known damage was reported from the quake, but the cause was attributed to gas extraction by Haak *et al.* (2001) who concluded that the depth and location of the 2.7M_L quake meant gas extraction was the most plausible and conceivable trigger.

3.8 Summary

The chapter has introduced the North Holland study site, providing detail on the geography, land cover, geology and gas production in the province. The geohazards resultant from gas production have been identified and mechanisms of ground motion have been considered in detail, including the consequential effects it has on both the surface and subsurface. The land cover characteristics and history of natural gas extraction make it an ideal site for ISBAS analysis. In addition, as noted in Section 2.8.2, this site was used previously to test InSAR algorithms in the Terrafirma Validation Project, and hence provides an ideal test of ISBAS in comparison to previous results.

4 Processing Requisites

4.1 Data Sources

4.1.1 SAR

ESA's ERS-1, ERS-2 and ENVISAT data sets were an obvious choice for interferometry due to the large back catalogue of historical imagery and suitable coverage of North Holland. The area of interest was overlapped by a variety of pass geometries but the most suitable was track 423 on a descending pass, as the AOI was located in the centre of the scenes. 29 ERS-1 SAR images (1992-2000), 55 ERS-2 SAR images (1995-2000) and 76 ENVISAT SAR images (2003-2010) were identified, giving a total of 160 single look complex images covering a 18 year period, ample for valid differential interferometry. A category-1 (Cat-1) proposal, implemented predominantly for non-commercial and academic use, was established with Dr Andrew Sowter as principle investigator to order the archived data. Additionally, 17 Sentinel-1 images were downloaded from the Sentinel Data Hub. These were from orbit 37 on a descending pass, acquired in Interferometric Wide Swath mode.

4.1.2 DEM

A SRTM 90m Digital Elevation Model was sourced from the CGIAR-CSI GeoPortal. The NASA STRM mission has provided DEM's for over 80% of the globe which are available in 5 degree x 5 degree tiles (CGIAR-CSI, 2015).

4.1.3 Shapefiles

Locations of gas fields and mine workings were attained from the Netherlands Oil and Gas Portal (NLOG, 2015) that delivers information about oil, gas and geothermal energy exploration & production within the Netherlands and Dutch segment of the North Sea continental shelf.

4.1.4 Geodetic Levelling

Levelling benchmark data was attained from the Geo-Information and ICT Advisory Department (AGI) of the Directorate-General of Public Works and Water Management (Rijkswaterstaat, RWS), which administers the national ordinance surveys and all precision levelling campaigns. Benchmarks sought were of the 1st order, located approximately 30 metres below the surface, established on Pleistocene sand deposits

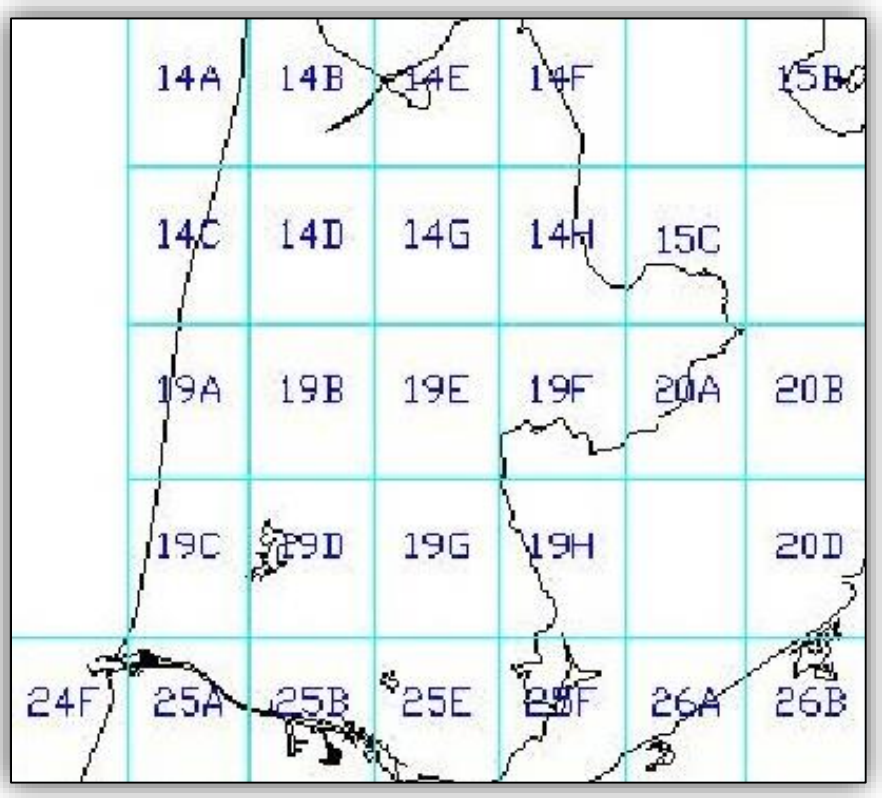


Figure 4.1: *Locations of the zonal divisions of levelling benchmarks.*

which define the Dutch ordnance level. Data was acquired for zones 14C, 14D, 14G, 14H, 19A, 19B, 19E, 19F, 19C, 19D, 19G and 19H from 94 campaigns spanning 1991 to 2012 (Figure 4.1).

4.2 Software

4.2.1 Punnet

Punnet software is an in-house interferometric software developed by Dr Andrew Sowter of the Nottingham Geospatial Institute, University of Nottingham. It is based on the Raspberry software, originally designed to process ALOS PALSAR radar imagery by the conventional two-pass differential technique. Punnet is run inside the MATLAB environment utilizing a modified version of the SNAPHU package (Chen & Zebker, 2001) for phase unwrapping, that facilitates phase unwrapping over sparse grids. Both the SBAS (Berardino *et al.,* 2002) and ISBAS (Sowter *et al.,* 2013) methodologies can be implemented for high and low resolution outputs. Outputs are in the form of .kml files, compatible with Google Earth, and .txt files, which enable analysis in GIS software.

4.2.2 ArcGIS

ArcGIS is a suite of geospatial processing software developed by Esri. It allows for the exploration, manipulation and analysis of data, with the capabilities to produce and export maps.

4.3 Summary

Data required for the investigation has been outlined and data sources have been acknowledged. Additionally, software used in the course of processing has been presented.

5 SAR Analysis

The ERS, ENVISAT and Sentinel data sets were processed separately. The following section provides an example methodology of interferogram formation.

5.1 Interferogram Processing Flow

5.1.1 SLC Data

Raw signal data is dispersed in azimuth and range for a point target, focusing amasses the dispersed energy into an individual pixel. Data received from ESA was in Single Look Complex (SLC) format, and therefore it was ready for coregistration without the need for focusing.

5.1.2 Coregistration

Due to the nature of the repeat pass configuration, SAR imagery is acquired from different orbits at different times that are only imprecisely repeatable. Start times (the initiation of first azimuth line) and the corresponding look angles will vary and thus the scattering features of the target area will be dissimilar. Specifically the size, rotation, area and backscatter of the images will be different. Coregistration is necessary to ascertain an amendment that will map the locality of every slave pixel in the master image. For successful interferometry it is required that images are to be co-registered to within 0.12 of a pixel. At this accuracy, a negligible 4% decrease in coherence occurs (Just & Bamler, 1994).

5.1.3 Resampling and Interpolation

Following coregistration interpolation is necessary to discern the value of slave image pixels at their new locations. The selection of interpolation kernel is a trade-off between computational effort and accuracy. There is not a defined interpolation kernel that is suitable for every SAR resampling situation and the choice is conditional on the correlation properties of the signal (Hanssen & Bamler, 1999).

5.1.4 Interferogram Generation

Following resampling the master and slave images can be considered two equivalently sized complex arrays of values. Interferograms are formed by multiplying every complex

pixel of the master image with the complex conjugate of the corresponding pixel in the slave:

$$p(x,y) = s_1(x,y)s_2^*(x,y) \qquad (5.1)$$

Where *p(x,y)* is the interferogram pixel value at *(x,y)*, s_1 is the master SLC pixel value at *(x,y)* and $s_2^*(x,y)$ is the complex conjugate of the slave SLC pixel value at *(x,y)*. Consequently, the amplitude values are multiplied while the phase values are differenced. The resultant array is complex, comprising of the multiple of the two amplitudes and interferometric phase (InSAR). Figure 5.1 displays an interferogram generated over North Holland, where phase is displayed as a periodic colour cycle. It is evident that areas of noise are consistent with rural areas and water bodies; this is evident along the left hand side of the image where the West coast of the province can be made out.

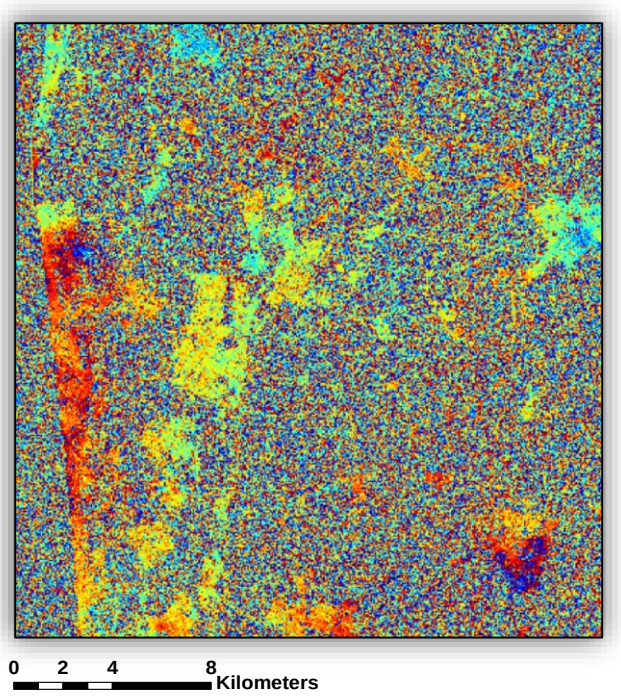


Figure 5.1: *Interferogram of North Holland where phase displayed as a periodic colour cycle. One colour cycle represents 2π radians. From ERS-2 data: 11th September 1996 and 25th December 1996, B⊥ = 23m.*

5.1.5 Multilooking

Multilooking is implemented to decrease noise. The pixel size increases concurrent with an improvement in phase statistics as the standard deviation of phase approximation is

proportional to the square root of the quantity of pixels over which the average was calculated (Lee *et al.,* 1994). Consequentially, the reliability of phase unwrapping is improved by multilooking (Goldstein *et al.,* 1988), whilst the spatial resolution decreases.

5.1.6 Coherence

Coherence is the measure of the phase correlation between two corresponding signals and ranges from zero to one; zero represents no correlation, while one represents perfect correlation. Coherence is a by-product of the interferogram formation process which is very useful in interferometric SAR when considered over a finite interval of space or time (Woodhouse, 2005). The coherence between two numbered SAR scenes (γ_{s1s2}) is expressed as:

$$\gamma_{S_1 S_2} = \left| \frac{\langle S_1 S_2{}^{*2} \rangle}{\sqrt{\langle |S_1|^2 \rangle \langle |S_2|^2 \rangle}} \right| \qquad (5.2)$$

Where S_1 and S_2 denote the complex pixel values for the two scenes and $\langle\ \rangle$ denotes averaging over a neighbourhood. High coherence is generally found in urban areas as, over time, towns and cities alter less than vegetation. An example of this can be seen in Figure 5.2, where coherence and amplitude images of North Holland are displayed side by side demonstrating how low coherence (dark areas) are correlated with rural expanses, while high coherence is associated with urban areas.

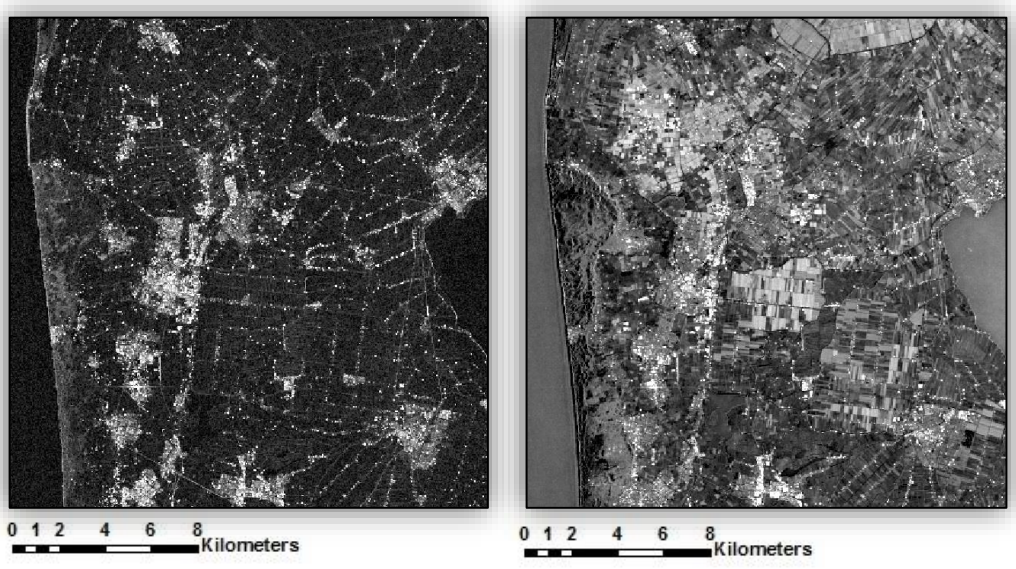


Figure 5.2: *(Left) Coherence Image of North Holland, where brightness represents high coherence. Computed from ERS-2 data: 20.03.1996 and 24.04.1996, B⊥=148.48m. (Right) Amplitude Image of the same area computed from fifty-two scenes.*

5.1.7 Filtering

Filtering is commonly applied to diminish Gaussian noise by attenuating frequencies outside of a particular range in an image. Within InSAR two-dimensional bandpass filters that are specified in terms of normalized centre frequencies are common, although adaptive filtering techniques with no set impulse response width are becoming increasingly popular. Rather than a static impulse response width, it is revised upon data characteristics such as coherence, terrain gradient, fringe rate and signal-to-noise ratio. The purpose is to preserve areas that do not require filtering, while applying a strong filter to those that do (Goldstein & Werner, 1998). It must be noted that no filtering is applied in the linear ISBAS analysis, although it can be useful tool when viewing differential interferograms for non-linear analysis.

5.2 ERS

5.2.1 Processing

There were significant orbital inaccuracies within the ERS-1 dataset, especially of those in the first few years of the satellites operation. In addition, there was a gap in data collection in 1994, therefore due to the ample amount of ERS-2 images the 29 ERS-1 images were not used in the study. 52 SAR images (Table 5.1) between 19th July 1995 and 16th August 2000 were processed, with restrictions of 250m on the perpendicular baseline and four years on the temporal baseline, creating 399 multi-looked differential interferograms (Figure 5.3). Multilooking was implemented using a 4 x 20 window size, producing pixels of 100m x 100m in ground range. Points deemed coherent were those which displayed a coherence greater or equal to 0.25. The quantity of coherent points per row and column coordinate m was computed and a threshold of value of M = 120 established, principally founded on the consideration that this would cover over 95% of the scene. A linear analysis was performed with a reference point at 52°40'16.32"N 4°47'58.92"E chosen for unwrapping, located in the town of Broek op Langedijk approximately 5.5km North East of Alkmaar (marked X in Figure 5.5). The point was chosen based upon the absence of a nearby gas reservoir and the urban nature of the surrounding area, increasing the probability of a dense network of coherent points in every interferogram. It is important that the point chosen for unwrapping is coherent in every interferogram, i.e. m_{ij} = 399 for this data set. Interferograms are unwrapped individually; therefore coherent points will most likely be different in each interferogram. Having a reference point coherent in all 399 layers will ensure that there will be a good reference point in every layer. Finally, to enable a comparison with levelling benchmarks the line of sight (LOS) velocities were

Date	$B_{\perp}$(m)	Date	$B_{\perp}$(m)
27th August 1997	0	25th March 1998	-447
19th July 1995	-424	29th April 1998	-54
23rd August 1995	-429	3rd June 1998	95
27th September 1995	-137	8th July 1998	-1015
1st November 1995	248	12th August 1998	-460
6th December 1995	-566	16th September 1998	-867
10th January 1996	-211	21st October 1998	-722
20th March 1996	-51	25th November 1998	-975
24th April 1996	97	30th December 1998	-1077
29th May 1996	-706	3rd February 1999	-536
3rd July 1996	-158	10th March 1999	-793
7th August 1996	-235	14th April 1999	57
11th September 1996	-709	19th May 1999	-330
16th October 1996	-151	23rd June 1999	-191
20th November 1996	653	28th July 1999	79
25th December 1996	-685	1st September 1999	-1013
29th January 1997	-76	6th October 1999	-660
9th April 1997	174	10th November 1999	-158
14th May 1997	-483	15th December 1999	-282
18th June 1997	-558	19th January 2000	-637
23rd July 1997	-359	23rd February 2000	-1170
1st October 1997	-401	29th March 2000	-437
5th November 1997	-986	3rd May 2000	-477
10th December 1997	-1248	7th June 2000	-774
14th January 1998	-626	12th July 2000	-1330
18th February 1998	-381	16th August 2000	-540

Table 5.1: *ERS-2 SAR image dates and perpendicular baselines B⊥ (m) in reference to the master image on 27th August 1997.*

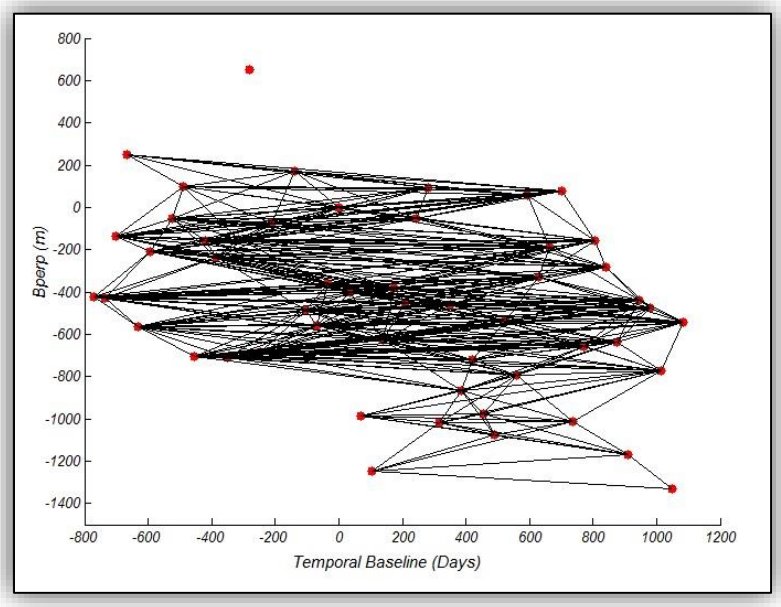


Figure 5.3: *Temporal and perpendicular baselines of the ERS-2 SAR image pairs processed over North Holland.*

converted into vertical velocities for each coherent point. LOS velocities (v_{LOS}), the measure of motion between the satellite and the radar resolution cell on the ground, are converted to vertical velocities (v_{VERT}), the motion along the surface normal from the radar resolution cell on the ground, by:

$$v_{VERT} = \frac{v_{LOS}}{\cos\theta} \qquad (5.3)$$

where θ is the incidence angle from the surface normal, approximately 23° at scene centre for both of the ERS and ENVISAT frames.

5.2.2 Results

The ISBAS algorithm returned 133 317 points on the ground compared with 8574 using the standard SBAS method, a point density factor increase of over fifteen. It is important to note that we have only performed an ISBAS analysis over the study site. When referring to SBAS points throughout the study, these are points extracted from the ISBAS analysis, but which are coherent in every layer (m_{ij} = 399). This is different from performing a separate SBAS analysis. Extracting SBAS points from the ISBAS analysis will return point velocities at the same locations that would be achieved if we performed a separate SBAS analysis. It enables a comparison between the densities of points achieved by both techniques. However, differences would exist in the linear velocities achieved at these points. The ISBAS analysis has the advantage of a dense network of points which therefore improves the accuracy of unwrapping. The problem with large study sites is that unwrapping over large distances can be problematic, as large gaps between point's results in the propagation of errors. This problem is also amplified by changing land covers. The SBAS algorithm, along with other techniques such as PSI, struggle during unwrapping because once they get to the edge of an area dense in points (often at the boundaries of an urban region) it is unable to bridge the gap from urban areas to points far away with an acceptable error budget. With ISBAS, having a dense network of points improves unwrapping so the signal can propagate across the whole image and therefore bridge the gap with less errors. It is for this reason that ISBAS products are suited to deformation analysis over wide areas, as well as for the improved coverage they provide.

As previously mentioned in chapter 5.2.1 the standard SBAS method returns velocities for points where the average coherence is greater than 0.25; while the ISBAS method returns velocities for points where 120 or more coherences are greater than 0.25. The distribution of SBAS points is fairly limited and primarily located in urban areas; 70% of the points

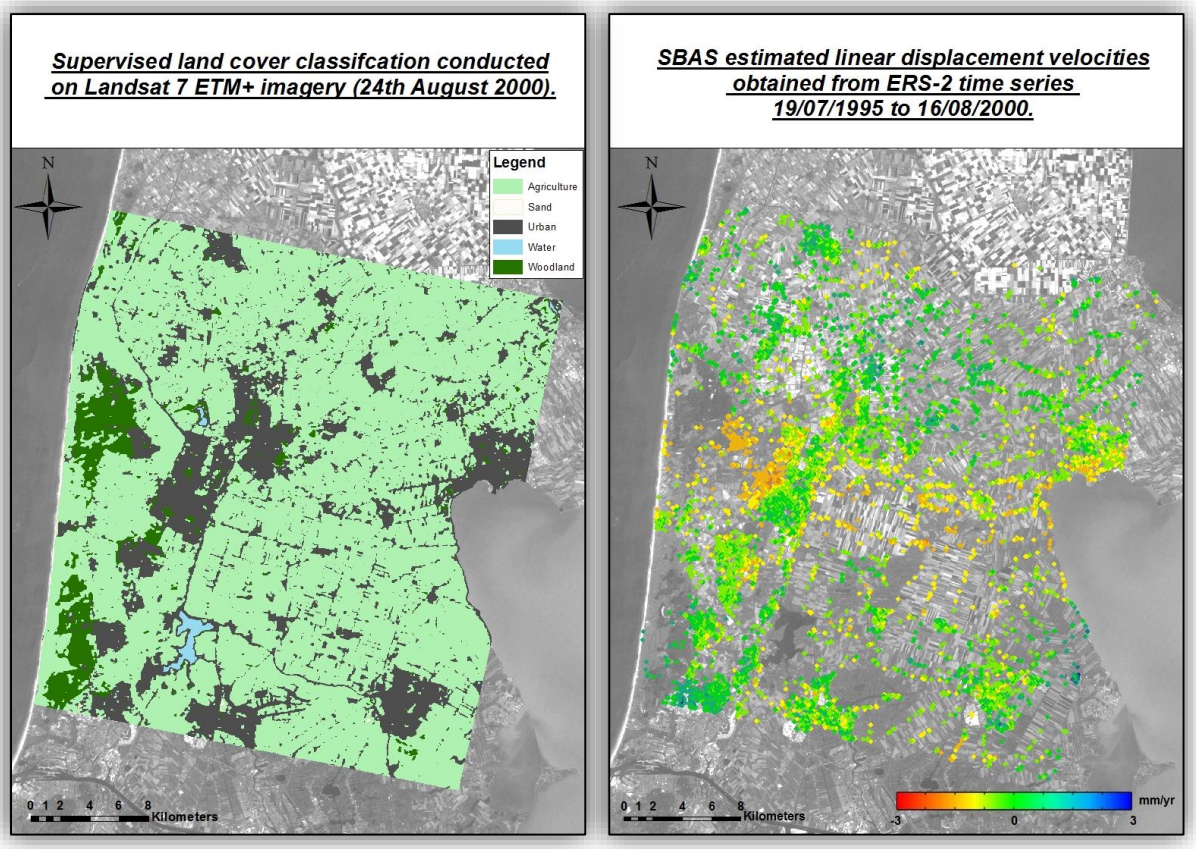


Figure 5.4: *(Left) Supervised land cover classification conducted on Landsat 7 ETM+ imagery (24th August 2000). (Right) SBAS estimated point velocities from ERS-2 time series.*

(5971) are located within urban expanses, Figure 5.4 exhibits the correlation between urban land cover and SBAS point velocities.

The ISBAS point velocities are more widely distributed and much denser, resulting in near complete coverage of the scene. SBAS points are displayed alongside the ISBAS results in Figure 5.5. The mean velocity of SBAS points was -0.19 ± 0.47 mm year which ranged from subsidence of -3.53 ± 0.43 mm year seen over Alkmaar, in the area just outside the boundaries of the Bergermeer gas field, to uplift of 2.16 ± 0.60 mm year. The standard deviation ranged from 0.21 – 0.70 mm/year. The mean point velocity of the ISBAS analysis returned a stronger deformation signal than the SBAS points, at -0.42 mm year. It ranged from subsidence of -4.48 ± 0.91 mm/year observed to the West of Bergen, between the Bergen and Bergermeer gas reservoirs, to uplift of 3.31 ± 0.96 mm year. The standard deviation ranged from 0.21 – 1.63 mm year, exhibiting a high error and a greater

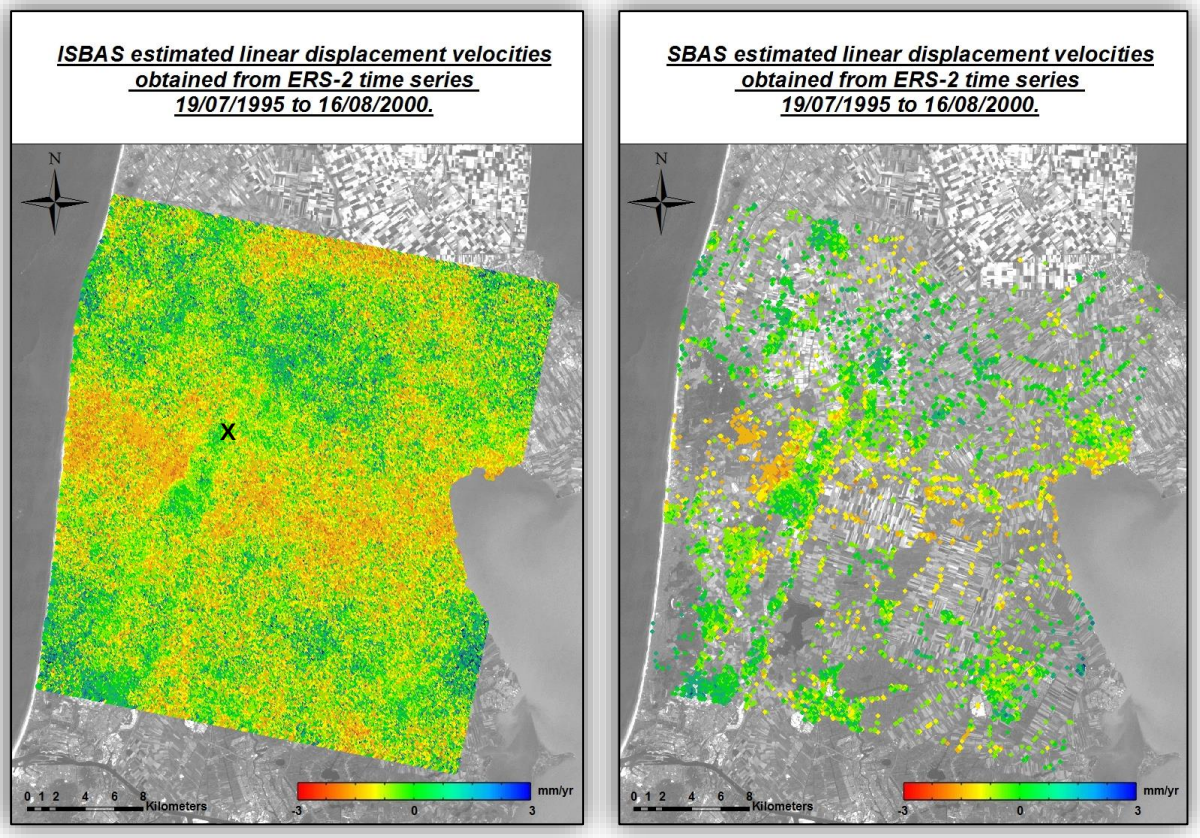


Figure 5.5: *ISBAS (left) and SBAS (right) derived vertical velocities from ERS-2 time series. X marks the unwrapping point.*

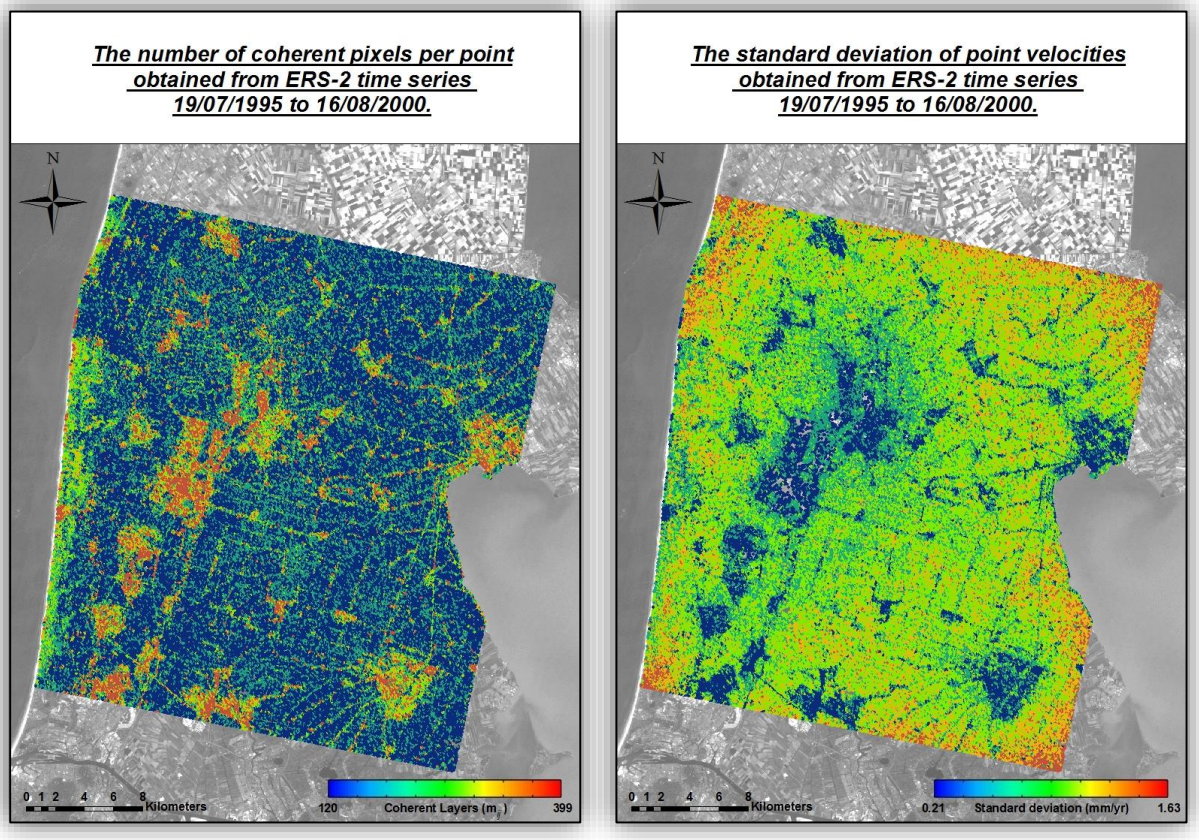


Figure 5.6: *(Left) Coherent pixels per point. (Right) Standard Deviation of point velocities.*

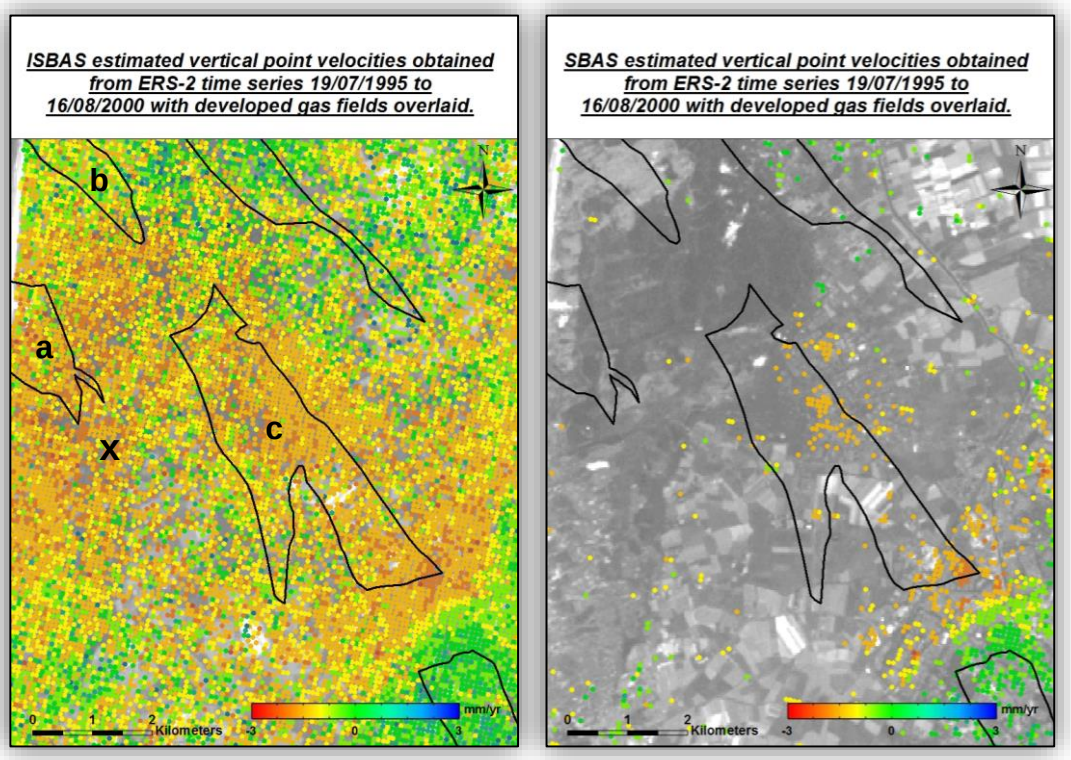


Figure 5.7: *ISBAS (left) and SBAS (right) derived velocities around the Alkmaar and Bergen region, with the developed gas fields overlaid. X marks location of maximum subsidence.*

range than seen in the SBAS points. Lower standard deviations are observed in urban areas, as may be expected due to the likelihood of more coherent pixels per point, m_{ij}. This is depicted visually in Figure 5.6, which shows that the predominant source of error is seen within targets exhibiting intermittent coherence, with a strong correlation in relation to the variance and m_{ij}.

Overall the scene is fairly stable, with the majority of the scene displaying little motion. Where motion does occur it is relatively small ranging up to 3 mm/year. Subsidence here can be attributed to natural gas extraction as the results quite good correlation with the gas reservoirs near Bergen, to the West of Alkmaar. As seen in Figure 5.7 the main area of deformation is around the Bergen (a) and Bergermeer (c) gas reservoirs. The point of maximum deformation (-4.48 ± 0.91 mm/year) is marked X, located just to the South East of the Bergen field. A more accurate correlation with the reservoir boundary may not have been seen at Bergermeer due the complex subsurface geology (Section 3.7.1.1). The 3D structure of the geology could mean the location of subsidence at the surface is offset, and give the impression ISBAS results are less coincident with the reservoir boundary.

The additional coverage of the ISBAS analysis is vital over this area as the conventional SBAS method only produces point velocities of a significant density in the South East over the urban location of Alkmaar, and limited velocities over the Bergermeer reservoir (in the town of Bergen). The ISBAS analysis covers most of the region, extending over woodland and agricultural areas, and ascertains that subsidence occurs across the Bergermeer field, and extends West over the Bergen field.

The stability of scatterers is indicated by the coherence which ranges from 0 to 1. Scatterers are less stable in rural areas due to the changeable nature of vegetation, whereas coherence in urban and rocky areas is higher as targets are stable. ISBAS points are able extend over rural environments by relaxing the need for coherence to be present in every layer; the reduced stability of the scatterers is reflected in the higher standard error of these points. There does not appear to be any notable systematic changes in coherence in the interferograms from season to season, whether they were formed from images acquired in summer, winter or a mixture of both, coherence remains constant.

5.3 ENVISAT

5.3.1 Processing

The study site for the ENVISAT analysis was reduced, to help decrease processing times and complications. Due to the lack of significant motion to the East of the scene the area was focused toward the surrounding area of Alkmaar and Bergen, where most motion was found in the ERS time series. Additionally, levelling campaigns toward the East of the ERS study site are sparser, reflecting the fact that of fewer gas fields in the area necessitate less subsidence monitoring. 750 multi-looked differential interferograms (Figure 5.8) were created from 75 images (Table 5.2), with restrictions of 250m on the perpendicular baseline and four years on the temporal baseline. Multilooking was implemented using a 4 x 20 window size, producing pixels of 100 x 100m in ground range. Points deemed coherent were those which displayed a coherence greater or equal to 0.25. The reference point chosen for unwrapping was located close to Heiloo (52°35'59.2"N 4°41'59.3"E) approximately 2km South-West of Alkmaar. It was chosen due to the lack of nearby gas reservoir and the town's urban land cover which increased the likelihood of a dense network of points in every interferogram. The quantity of coherent points per row and column coordinate, *m,* was calculated, and a threshold of *M*=250 was

Date	$B_{\perp}$(m)	Date	$B_{\perp}$(m)
26th July 2006	0	28th March 2007	-137
19th March 2003	-662	2nd May 2007	-849
2nd July 2003	-1132	6th June 2007	-691
6th August 2003	-1188	11th July 2007	-780
10th September 2003	-450	15th August 2007	-671
15th October 2003	82	19th September 2007	-124
19th November 2003	-1639	24th October 2007	-914
24th December 2003	-459	28th November 2007	-377
28th January 2004	-52	2nd January 2008	-1123
3rd March 2004	-977	6th February 2008	-434
7th April 2004	151	12th March 2008	-741
12th May 2004	-1211	16th April 2008	-332
16th June 2004	-693	21st May 2008	-726
21st July 2004	-464	25th June 2008	-525
25th August 2004	-606	30th July 2008	-614
29th September 2004	-1330	3rd September 2008	-333
3rd November 2004	-594	8th October 2008	-769
8th December 2004	-614	12th November 2008	-575
12th January 2005	-1335	17th December 2008	-910
16th February 2005	-1125	21st January 2009	-498
23rd March 2005	-1549	25th February 2009	-593
27th April 2005	-272	1st April 2009	68
1st June 2005	-861	6th May 2009	-860
6th July 2005	-75	10th June 2009	-491
10th August 2005	-800	15th July 2009	-561
19th October 2005	-623	19th August 2009	-678
23rd November 2005	-410	23rd September 2009	69
28th December 2005	-386	28th October 2009	-769
1st February 2006	-1305	2nd December 2009	-551
8th March 2006	-553	6th January 2010	-778
12th April 2006	-1228	10th February 2010	-236
17th May 2006	-845	17th March 2010	-607
21st June 2006	-571	21st April 2010	-254
30th August 2006	-79	26th May 2010	-756
4th October 2006	-1466	4th August 2010	-943
8th November 2006	-1209	8th September 2010	-614
17th January 2007	-60	13th October 2010	-74
21st February 2007	-594		

Table 5.2: *ENVISAT ASAR image dates and perpendicular baselines B⊥ (m) in reference to the master image on 26th July 2006.*

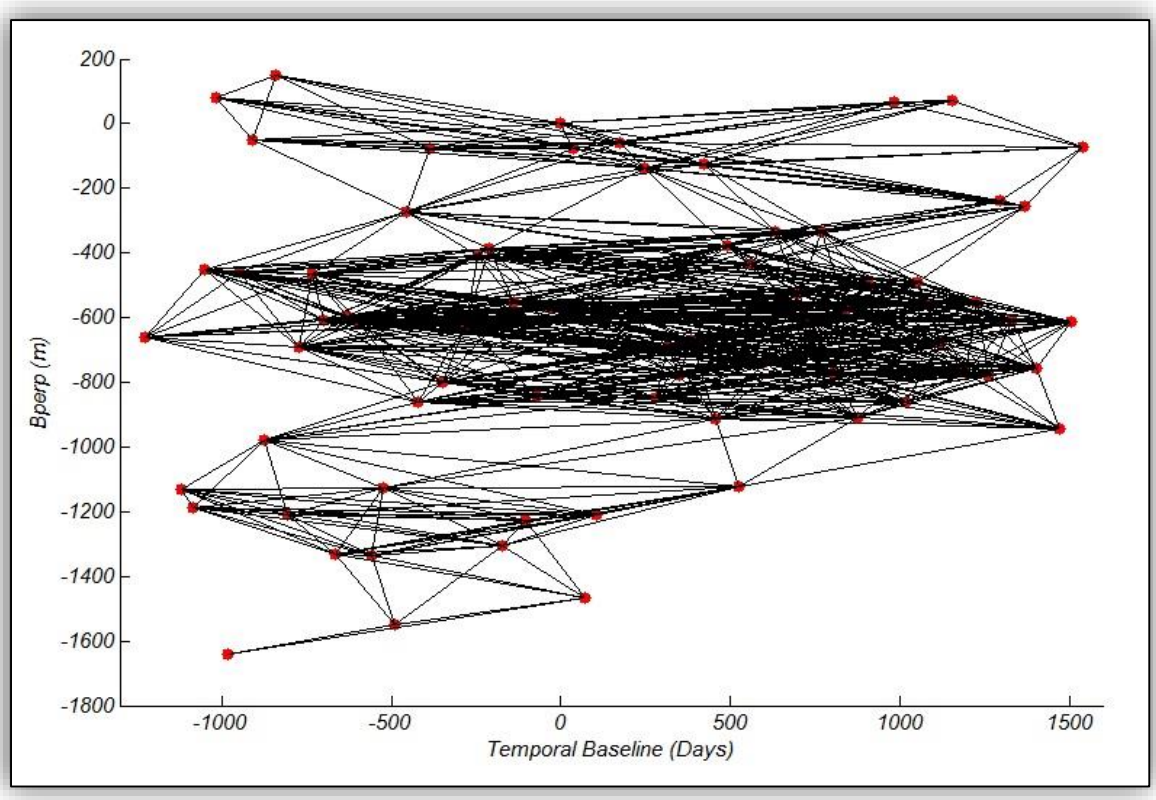


Figure 5.8: *Temporal and perpendicular baselines of the ENVISAT ASAR image data pairs processed over North Holland.*

established, which provided a coverage of over 95% of the scene. Finally point velocities were converted from LOS to vertical velocities, using Equation 5.3 (Section 5.2.1).

5.3.2 Results

The ISBAS analysis returned 34336 point velocities, 6.7 times more than the standard SBAS result, which produced 5142. As mentioned in Section 5.3.1, the standard SBAS returned velocities for those points where the average coherence was greater than 0.25 in all layers, while the ISBAS returned velocities for locations where coherences greater than 0.25 occurred in 250 or more layers. 77% of the SBAS velocities (3944) were located in urban land cover which can be seen in Figure 5.9. This emphasises the correlation of SBAS results with urban land cover. While the SBAS analysis is limited to urban regions, the ISBAS result achieved a wide and even spread across the scene (Figure 5.10).

The ISBAS analysis produced a mean point velocity of -0.17 ± 0.41 mm/year, which ranged from -2.57 ± 0.25 mm/year to 1.8 ± 0.97mm/year. The SBAS velocities were similar with a mean point velocity of -0.11 ± 0.24 mm/year, which ranged from -2.57 ± 0.25

mm/year to 1.08 ± 0.26 mm/year. The ISBAS standard deviation ranged from 0.14 - 0.79 mm/year and as expect the SBAS range of standard deviations was smaller, 0.14 - 0.39 mm/year. Similarly to the ERS results higher standard deviations were seen in rural areas due to the reduced likelihood of coherent pixels per point, m_{ij}. The same correlation is found with regards to the standard deviation and m_{ij}, confirming that the main source of error is found in points encompassing intermittent coherence (Figure 5.11).

Similarly to the ERS data set there was a lack of a strong deformation signal, and therefore a distinct pattern of subsidence. The ENVISAT time series appears to be more stable that of ERS, with little spatial correlation between subsidence and locations of gas reservoirs. The area of maximum subsidence in the scene is located at the West of Alkmaar, marked with an X on Figure 5.12. It is clear when comparing between the ISBAS and SBAS results, although it is evident that there is minimal subsidence in this time series, the coverage where point velocities are achieved is almost identical to the ERS time series. SBAS points are restricted to the South East in Alkmaar, while there is also a limited coverage over the Bergermeer reservoir in the town Bergen. In contrast, the ISBAS analysis covers most of the scene.

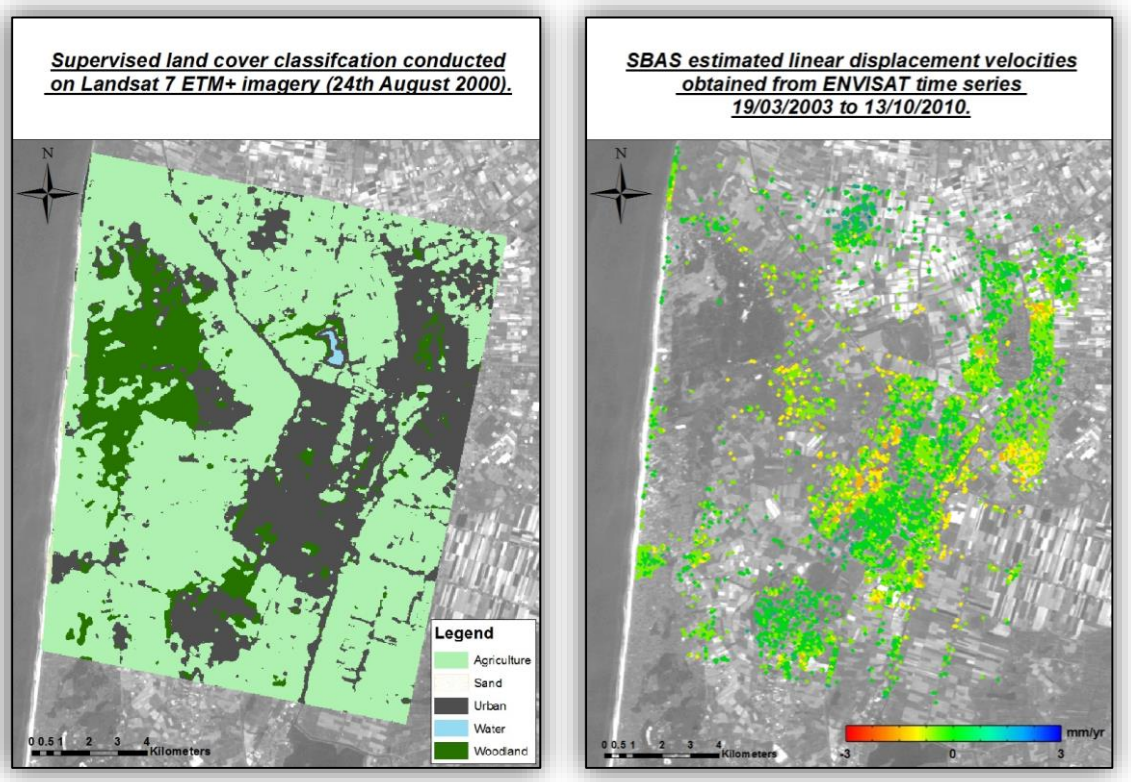


Figure 5.9: *(Left) Supervised land cover classification conducted on Landsat 7 ETM+ imagery (24th August 2000). (Right) SBAS estimated point velocities from ENVISAT time series.*

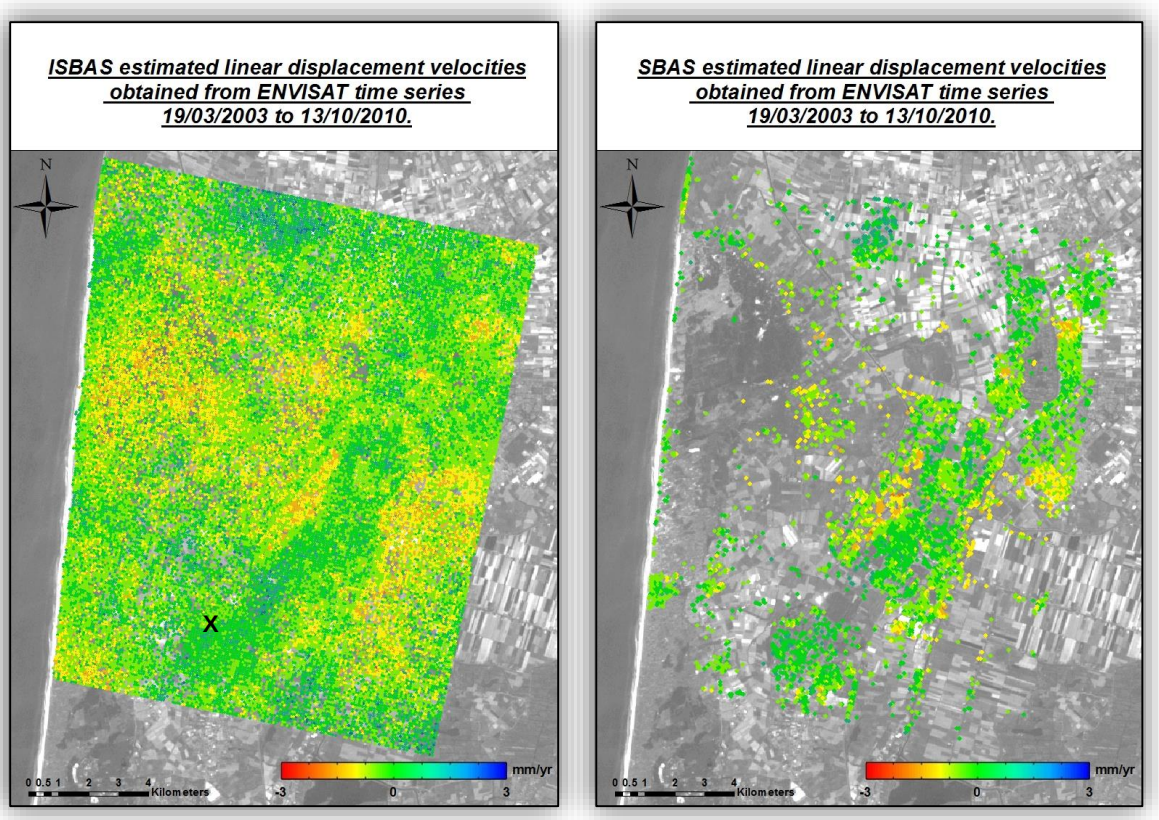


Figure 5.10: *ISBAS (left) and SBAS (right) derived vertical velocities from ENVISAT time series . X represents the unwrapping point.*

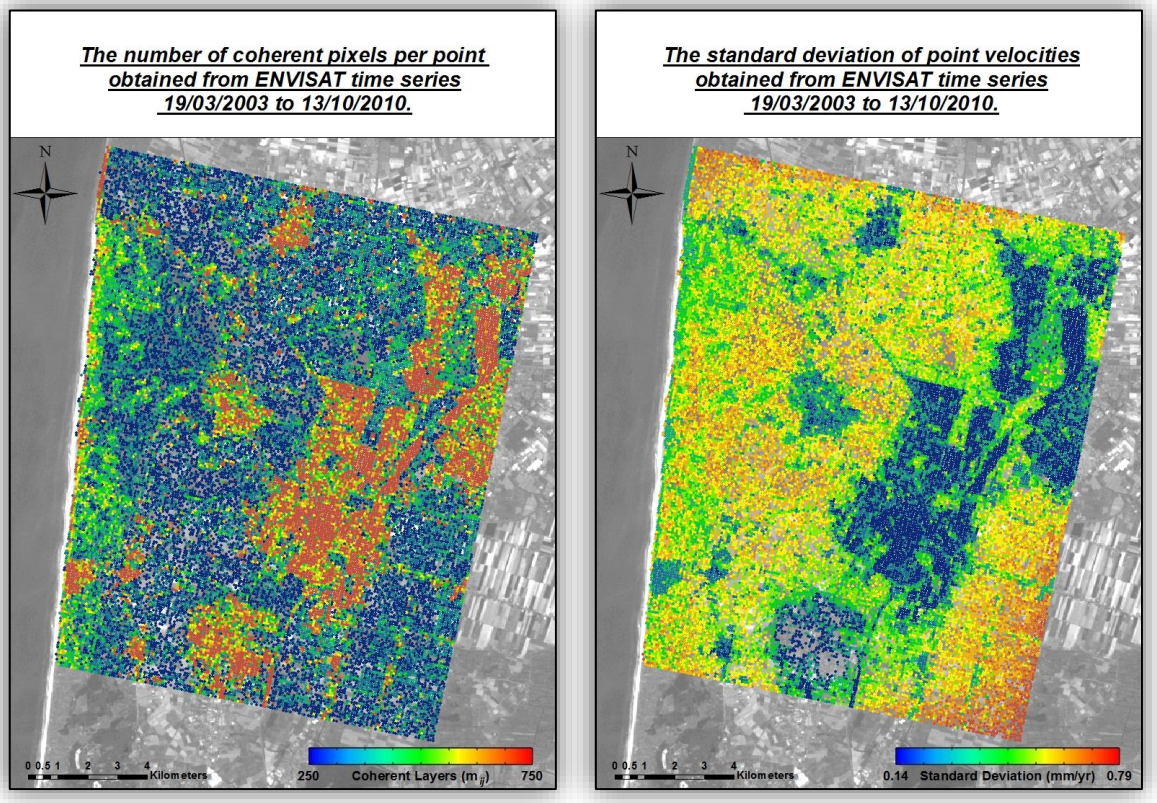


Figure 5.11: *(Left) Coherent pixels per point. (Right) Standard Deviation of point velocities.*

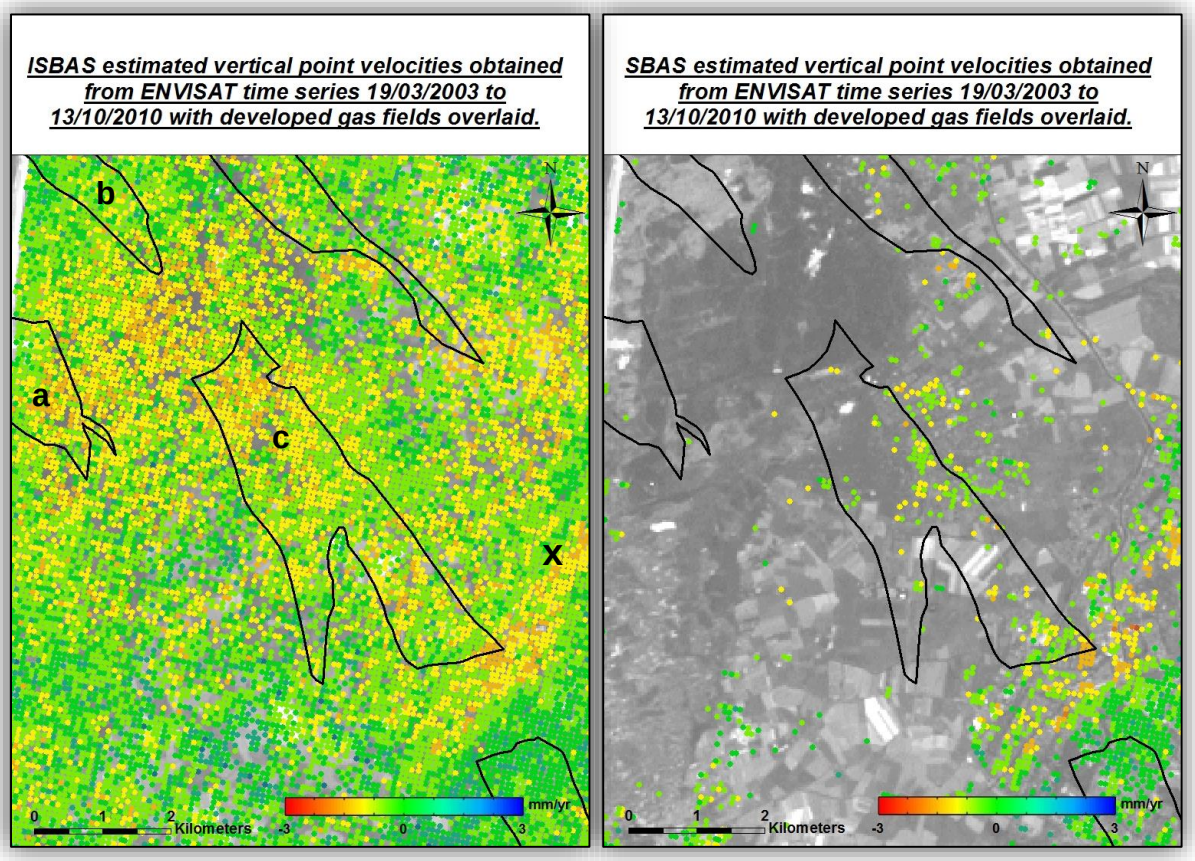


Figure 5.12: *ISBAS (left) and SBAS (right) derived velocities around Alkmaar and Bergen region, with the developed gas fields overlaid. X marks the location of maximum subsidence.*

A potential reason for the lack of motion is the conversion of the Bergermeer gas reservoir into an underground storage facility. Gas production in at Bergermeer commenced in 1972 which continued until depletion in 2006; during this time pore pressures dropped from 23MPa to 1 MPa. Production ceased approximately half way through the ENVISAT time series, with injection commencing shortly after which raised pore pressures back up to 13MPa. Geomechanical analysis performed during the Bergermeer Seismicity Study, TNO report (Muntendam-Bos *et al.,* 2008) predicted uplift during the injection of cushion gas and working gas to be between 4.9cm and 6.0cm. As a result, the linear analysis used could potentially miss a trend of subsidence from 2003-2006, followed by uplift from 2007 onwards. A non-linear analysis was performed on the ENVISAT time series, five-time series verify this. Figure 5.13 displays time series for the selected points, while Figure 5.14 displays the locations of the points in the scene. There is some evidence to suggest a change in behaviour shortly after gas production ceased, the standard error reduces dramatically for Points 30344, 28992 and 22477 after 2007; however, the results

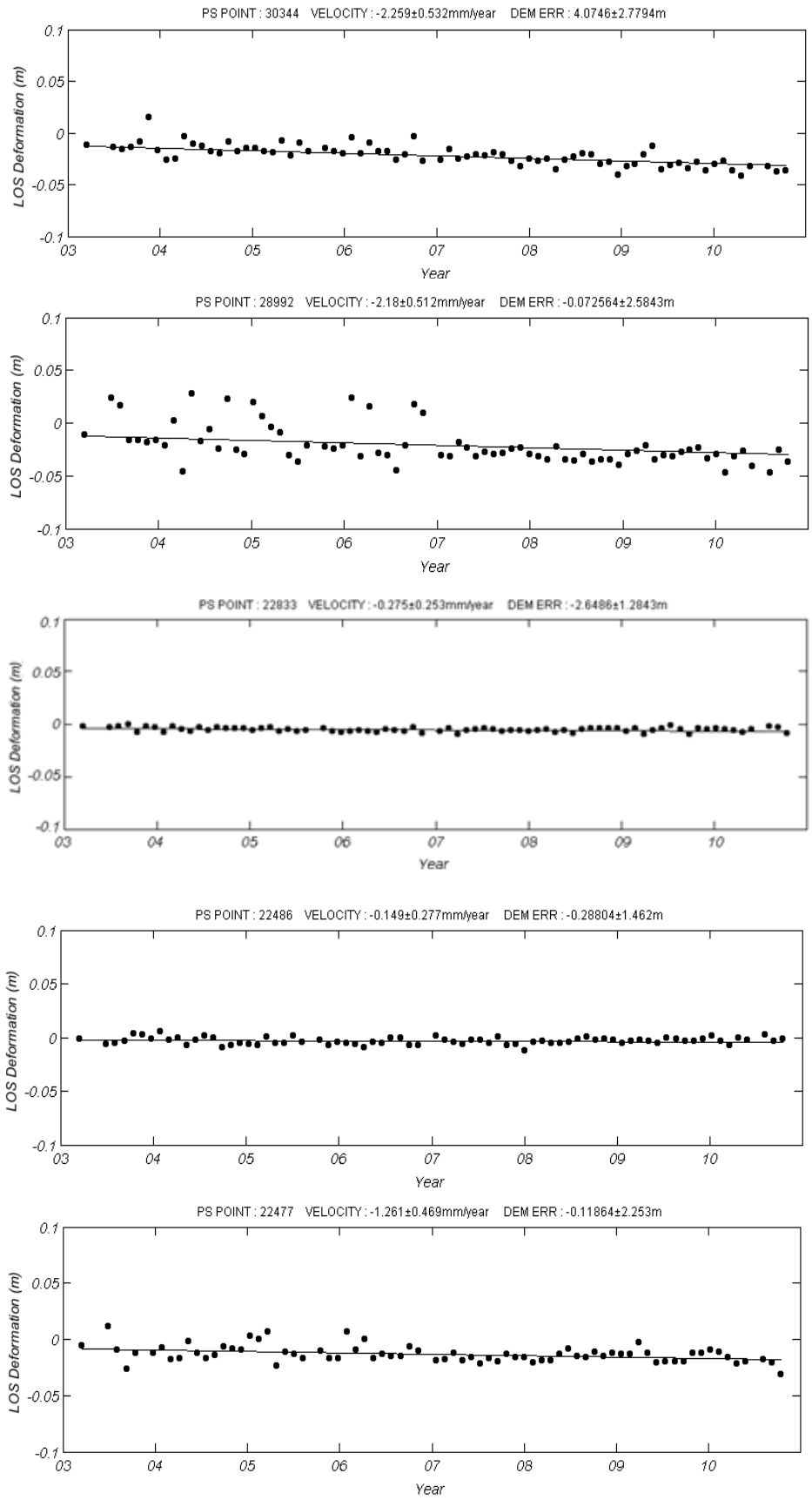


Figure 5.13: *Time series of five selected ISBAS points from ENVISAT non-linear*

indicate that a linear model is a suitable fit. The non-linear analysis of the ENVISAT time series confirms that the area has remained stable over the injection period. It is evident that velocities in urban environments, fit closer to the linear trend than those in non-urban environments, which are less consistent, reflected in the greater standard deviation of non-urban points. Points 30344 and 28992 are located in woodland, while points 22833, 22486 and 22477 are all in urban land cover.

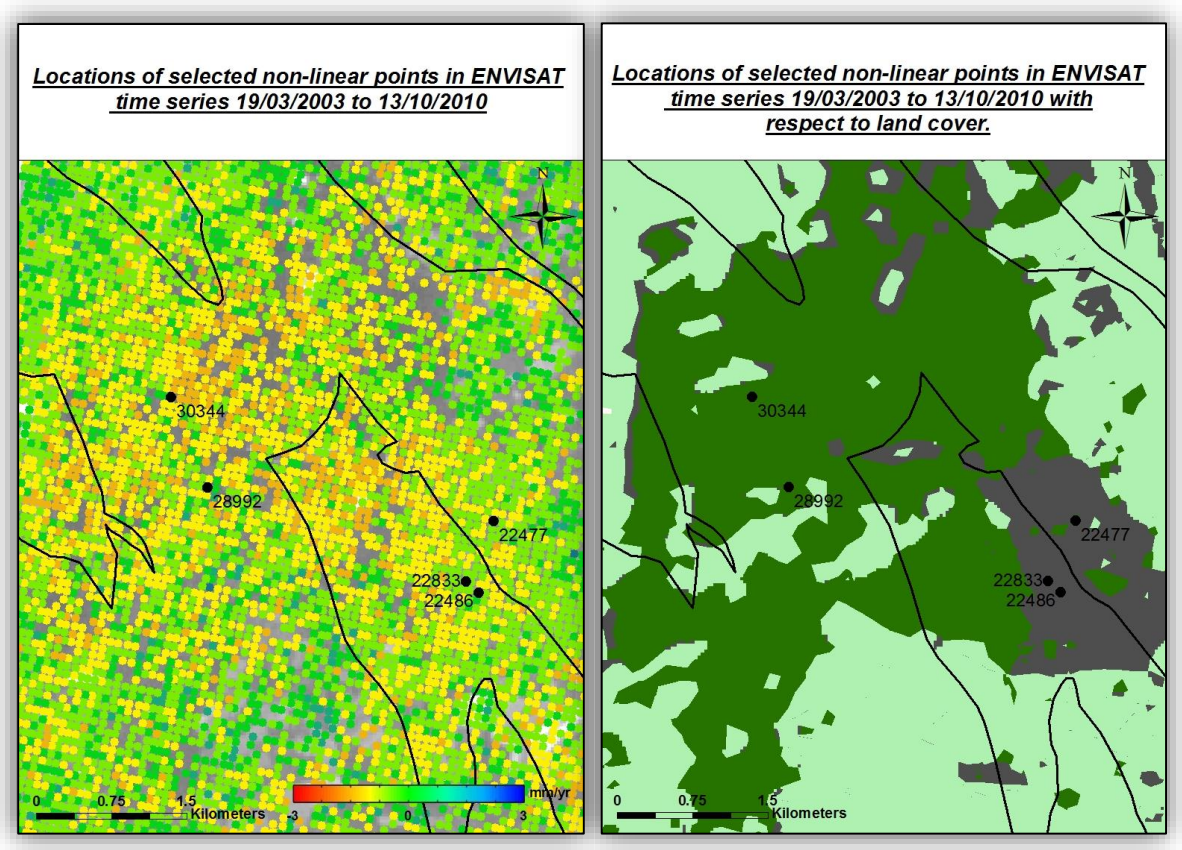


Figure 5.14: *(Left) Locations of the five selected ISBAS non-linear points. (Right) The selected points with respect to land cover.*

5.4 Sentinel

5.4.1 Processing

Additionally, a Sentinel data set was processed, covering the same area as the ENVISAT time series. Only 17 images of were available (Table 5.3), which were processed creating 136 multi-looked differential interferograms (Figure 5.15). There was no restriction on the temporal baseline due to the short time period of study (10 months) and 250m on the perpendicular baseline. Multi-looking was executed employing a 6 x 30 window size,

resulting in approximately 90m x 90m pixels in ground range. Points considered to be coherent were those with a coherence greater or equal to 0.25. The quantity of coherent points per row and column coordinate, *m,* was calculated, and a threshold of *M*=32 was established, which covered the majority of the scene. Similarly to the ENVISAT time series, the reference point chosen for unwrapping was located in Heiloo.

Date	***B⊥(m)***	***Date***	***B⊥(m)***
6th April 2015	0	18th April 2015	7
8th October 2014	0	30th April 2015	33
19th December 2014	50	12th May 2015	-71
31st December 2014	-57	24th May 2015	-76
5th February 2015	-15	5th June 2015	44
17th February 2015	49	17th June 2015	47
1st March 2015	-44	29th June 2015	87
13th March 2015	-124	11th July 2015	-121
25th March 2015	-137		

Table 5.3: *Sentinel-1a SAR image dates and perpendicular baselines B⊥ (m) in reference to the master image on 6th April 2015.*

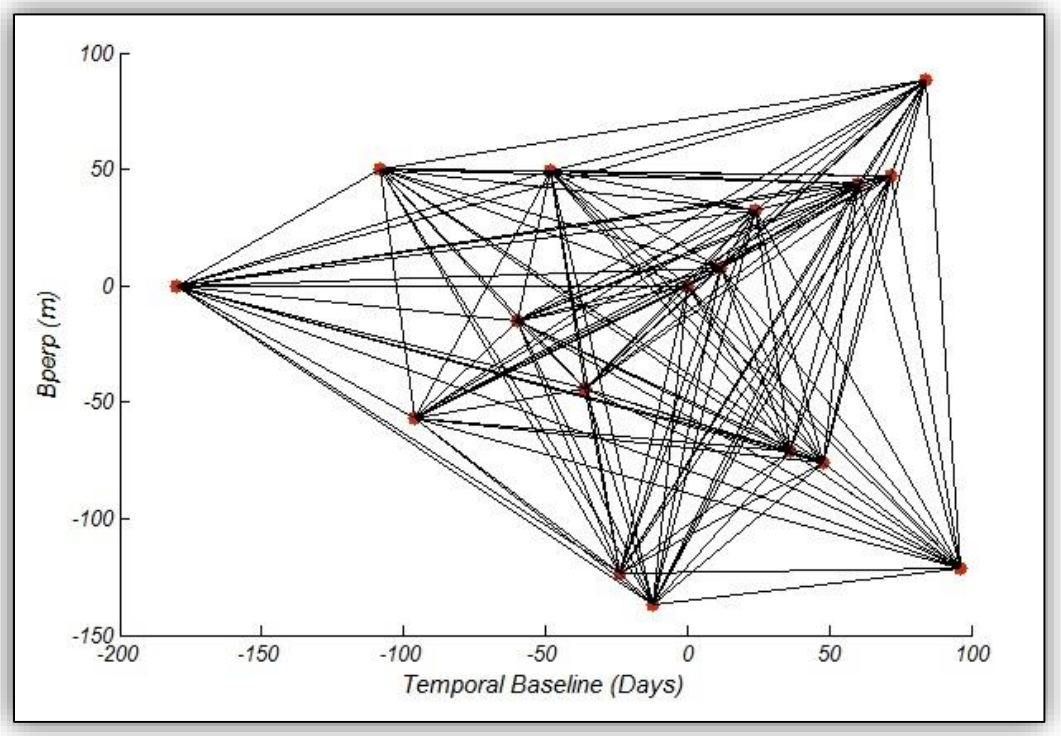


Figure 5.15: *Temporal and perpendicular baselines of the Sentinel-1 SAR image pairs.*

5.4.2 Results

The results were defective because so few images were used, 17 images is not enough for successful SBAS or ISBAS analysis. The production of 136 interferograms from 17 images introduces a significant bias in the results. The point velocities were predominantly noise, with some correlation over urban areas but poor over all other areas of the scene. This is reflected by the standard error which is significantly higher than that for the ERS and ENVISAT time series, by an order of a magnitude (up to 5cm). Two differential interferograms from the analysis are displayed in Figure 5.16, which potentially show some evidence of motion in the proximity of Bergen, where motion was observed in the ERS time series. More images would need to be acquired before this could be explored further.

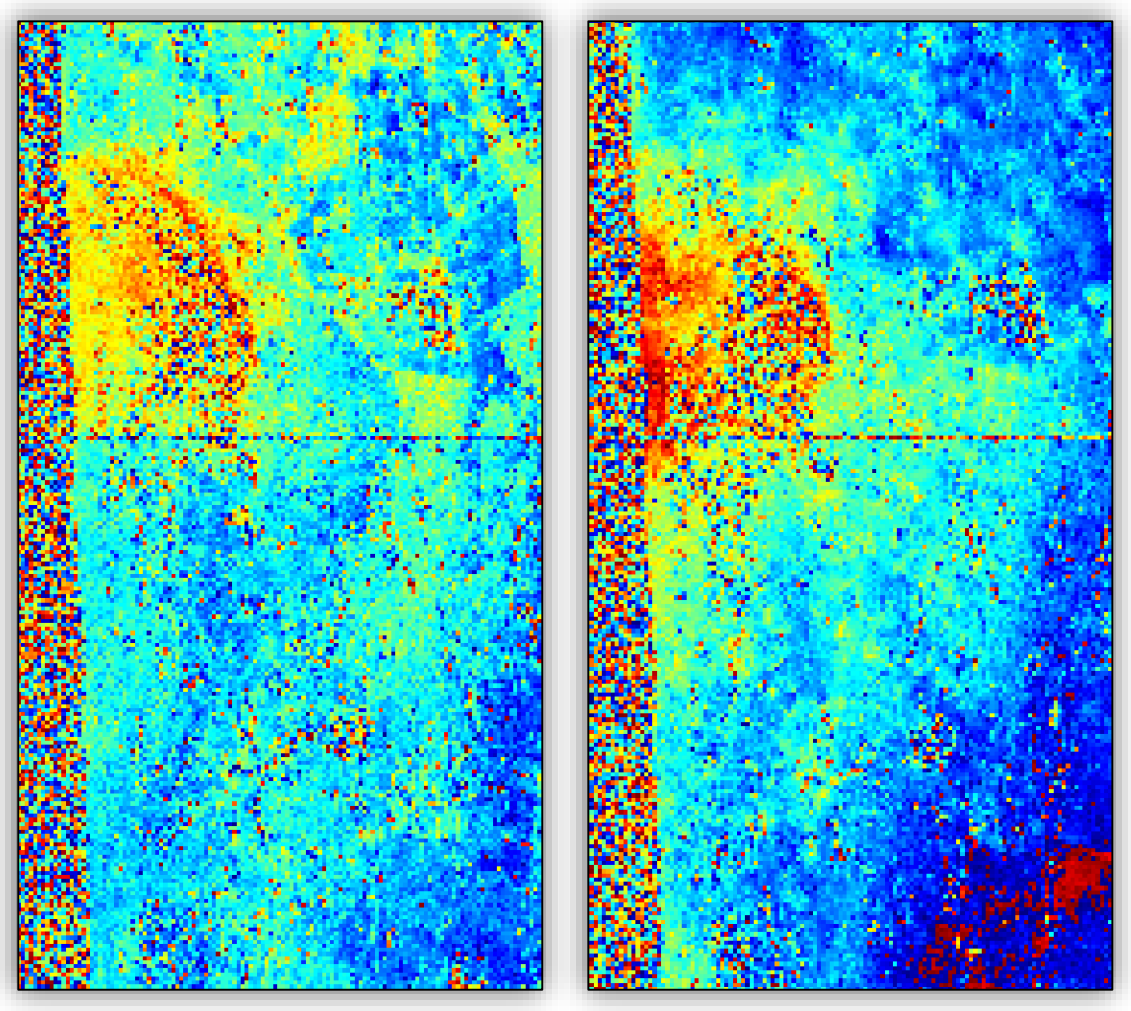


Figure 5.16: *Two interferograms of North Holland where phase displayed as a periodic colour cycle. One colour cycle represents 2π radians. From Sentinel-1 data: (Left) 5th February 2015 and 13th March 2015, B⊥ = -109m. (Right) 1st March 2015 and 13th March 2015, B⊥ = -80m.*

5.5 Summary

The processing for the SAR analysis has been described. An example interferogram processing flow is presented, followed by the details of the ERS, ENVISAT and Sentinel data sets. Where interferometry has been successful, the ISBAS products have achieved a denser coverage of point velocities than SBAS products. Consequentially, the identification of a subsidence pattern to the West of Alkmaar has been aided by the ISBAS analysis and ground motion shows a good correlation with gas reservoirs for the ERS time period. More motion was detected in the ERS data set, with a maximum velocity of -4.48 ± 0.91 mm/year, compared with the more stable ENVISAT data where the maximum velocity was -2.57 ± 0.25 mm/year. The correlation of the motion with the gas reservoirs is far less clear in the ENVISAT time period, which includes a significant period after production stopped and gas storage replaced it. Too few Sentinel-1 images have yet been acquired for the analysis to be definitive.

6 Product Validation

6.1 Levelling Benchmarks

Benchmarks for the ERS and ENVISAT validation were prepared separately, with levelling campaigns approximately four years before and after the radar acquisitions utilized. To enable the validation of ISBAS products, estimated velocities from the levelling data had to be computed. A linear trend was fitted through the levelling heights for every benchmark. Only those benchmarks that had three or more measurements were used in the validation to ensure the accuracy in the calculated velocity. Figure 6.1 displays an example of a levelling benchmark used in the ERS validation where it is evident that a linear model is suitable for the observed subsidence. Once fitted the height of the datum could be predicted at the start and end of the radar acquisitions and consequently a linear velocity could be calculated. Both the levelling and SAR data were converted to the European Datum 1950 coordinate system from the Dutch RD coordinate system (Rijksdriehoeksmeting) and WGS84 respectively. Finally, levelling benchmarks outside of the SAR footprint were eliminated.

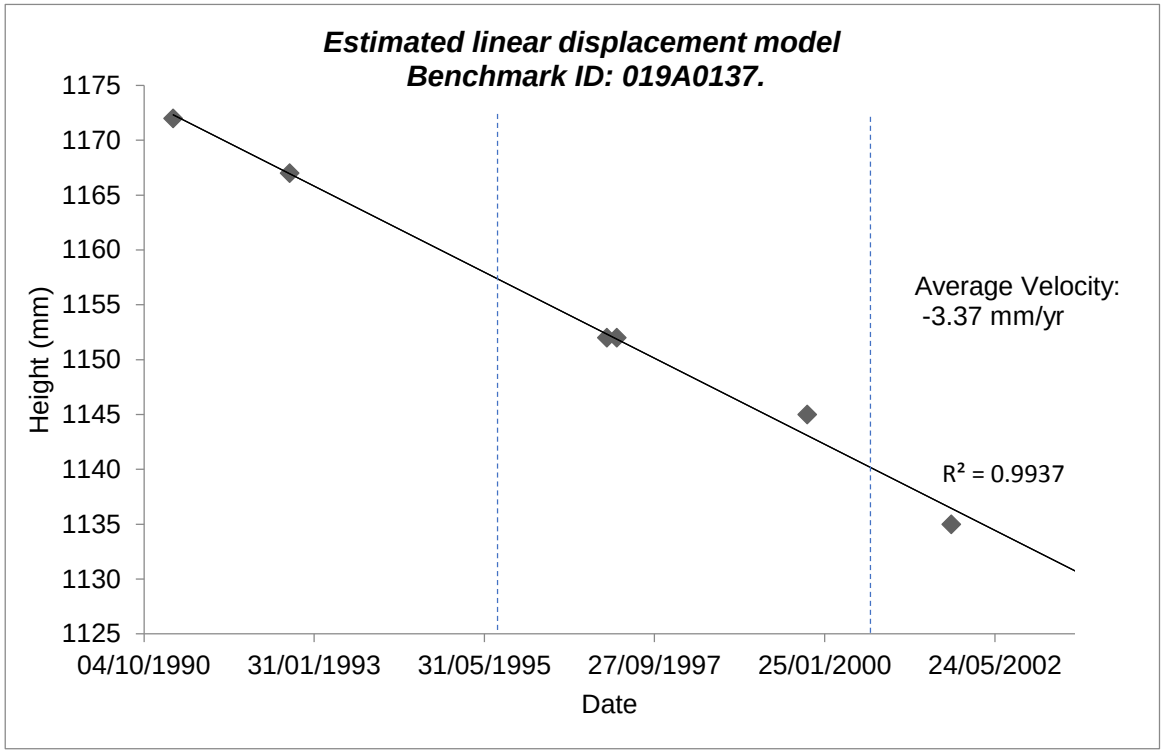


Figure 6.1: *The linear displacement model estimated for Benchmark ID:019A0137 for the ERS time series. The blue dashed lines represent the start and end of the SAR acquisitions.*

6.1.1 ERS

Levelling campaigns spanning a 12 year period were used in the ERS validation, from 27th February 1991 till 22nd July 2003, giving a total of 42 campaigns and a total of 1987 benchmarks. Although this gives the impression of a dense spatial and temporal count, many of these campaigns had only had a limited number of benchmarks. For example, 30 out of the 42 campaigns had less than ten benchmarks measurements. There were five dominant campaigns in the epoch that had upward of 200 benchmarks, displayed in Table 6.1. 356 benchmarks fulfilled the criteria and were consequently available for the validation of ERS data. Figure 6.2 exhibits the estimated linear displacement velocities from the levelling data covering the ERS time span, alongside the number of measurements per benchmark.

Campaign Date	*27/02/1991*	*23/03/1997*	*16/12/1997*	*30/10/1999*	*19/10/2001*
Number of Benchmarks	1313	406	986	638	232

Table 6.1: *Levelling campaigns in the ERS validation with over 200 benchmarks.*

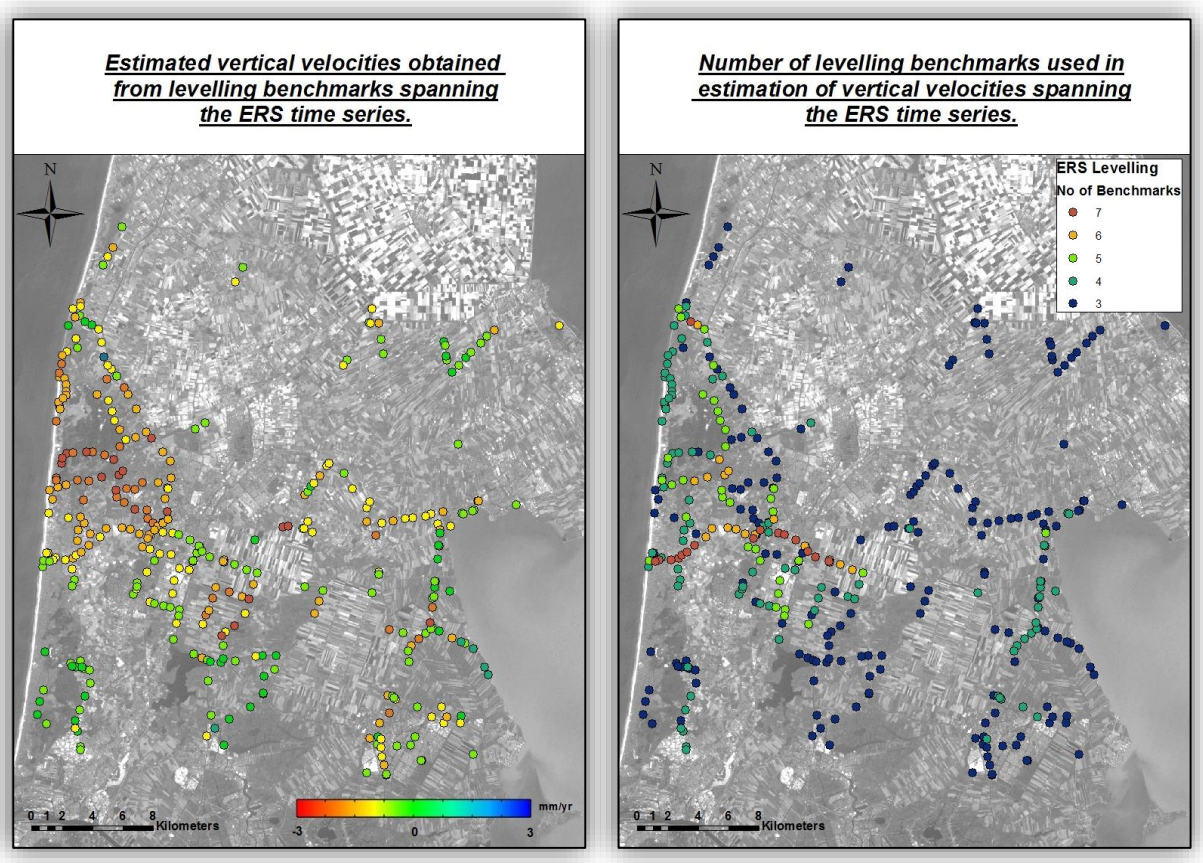


Figure 6.2: *(Left) Estimated linear velocities from levelling benchmarks covering the ERS time span. (Right) Number of benchmarks used in the calculation of linear velocities.*

6.1.2 ENVISAT

For the ENVISAT validation, levelling campaigns traversed a 13 year epoch, from 30th October 1999 till 9th September 2012. 1866 benchmarks were available from 81 campaigns; however similarly to the ERS validation many of these campaigns contained a limited number of measurements, with 70 out of 81 containing less than ten. Four campaigns contained more than 200 benchmarks, which are displayed in Table 6.2. 139 benchmarks satisfied the conditions and were thus available for the validation of ENVISAT data. Figure 6.3 exhibits the estimated linear displacement velocities from the levelling data covering the ENVISAT time span, alongside the number of measurements per benchmark.

Campaign Date	***30/10/1999***	***19/10/2001***	***19/01/2006***	***12/08/2007***
Number of Benchmarks	638	232	319	1525

Table 6.2: *Levelling campaigns in the ENVISAT validation with over 200 benchmarks.*

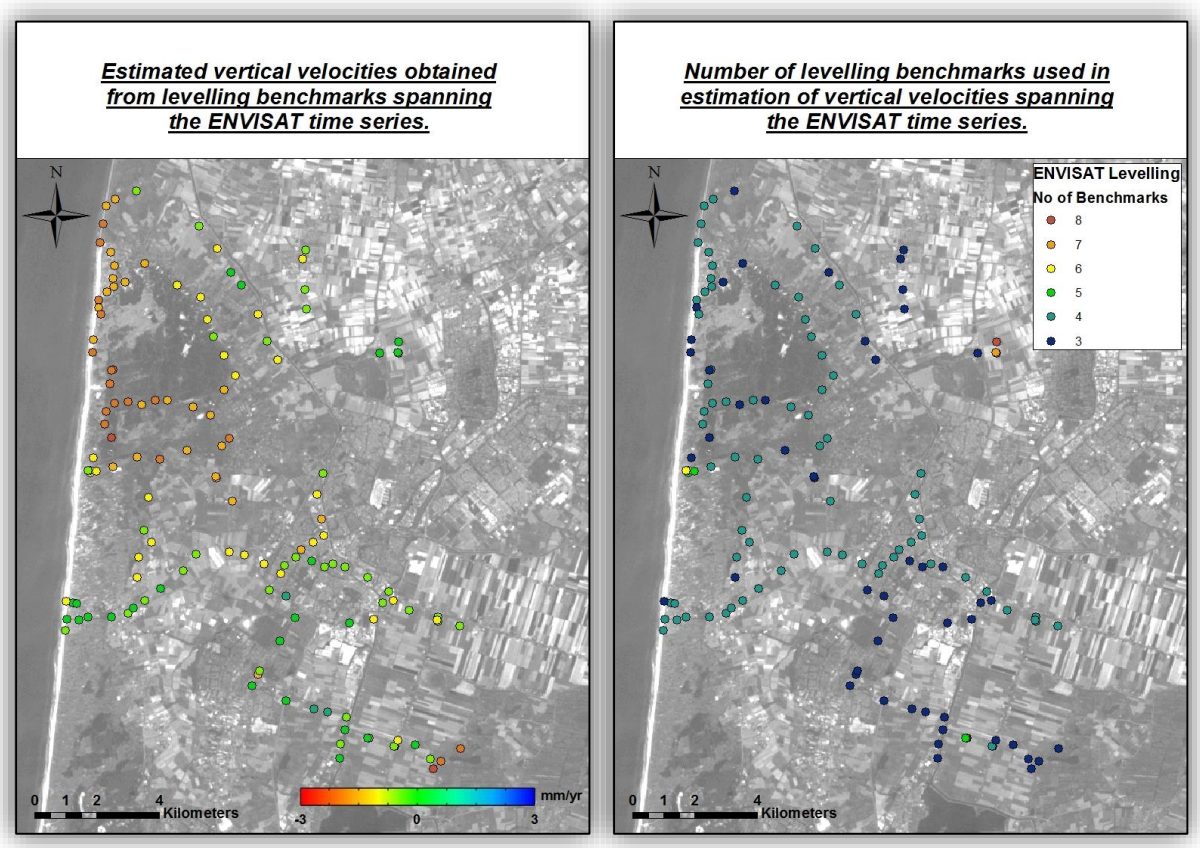


Figure 6.3: *(Left) Estimated linear velocities from levelling benchmarks covering the ENVISAT time span. (Right) Number of benchmarks used in the calculation of linear velocities.*

6.2 Spatial Validation - Kriging

For an investigative comparison between ISBAS products and levelling benchmarks, kriging was performed on the levelling data. Kriging produces an interpolated raster surface from point data. The kriging results should be taken with caution as levelling benchmarks are sparse over the study site, for instance in the Northern section of the ERS study site where places in the scene can be several kilometres from a levelling benchmark. Additionally, the results can vary extensively with the choice of parameters used in its calculation; for example the kriging method, semivariogram model and number of nearest sample points used in the interpolation.

Figure 6.4 displays the kriging produced from levelling next to ERS ISBAS analysis, while Figure 6.5 displays the comparison for the ENVISAT data. Table 6.3 gives a summary of the results. As previously mentioned these comparisons need to be taken with prudence. It is evident that in the ERS-2 data sets both the ISBAS and the kriging techniques have identified an area of subsidence around the Bergen and Bergermeer gas reservoirs, while there is a lack of motion over the city of Alkmaar. The ENVISAT data sets show a similar pattern but that the subsidence rates over the reservoirs have lessened, while Alkmaar remains stable. Crucially there is a consistency between the data; both in the patterns of stability and subsidence identified by the levelling and ISBAS analysis and in the differences between the ERS-2 and ENVISAT data, where higher rates of subsidence area identified in the ERS-2 data. It also needs to be noted that in both ERS and ENVISAT data sets the kriging appears to identify more motion in the area around the Bergen and Bergermeer reservoirs than the ISBAS analyses.

	Minimum velocity (mm/yr)	***Maximum velocity (mm/yr)***	***Average velocity (mm/yr)***
ERS			
Kriging	-3.15	0.16	-0.73
ISBAS	-4.48	3.31	-0.42
ENVISAT			
Kriging	-3.35	2.36	-0.61
ISBAS	-2.57	1.8	-0.17

Table 6.3: A comparison between kriging and ISBAS analyses.

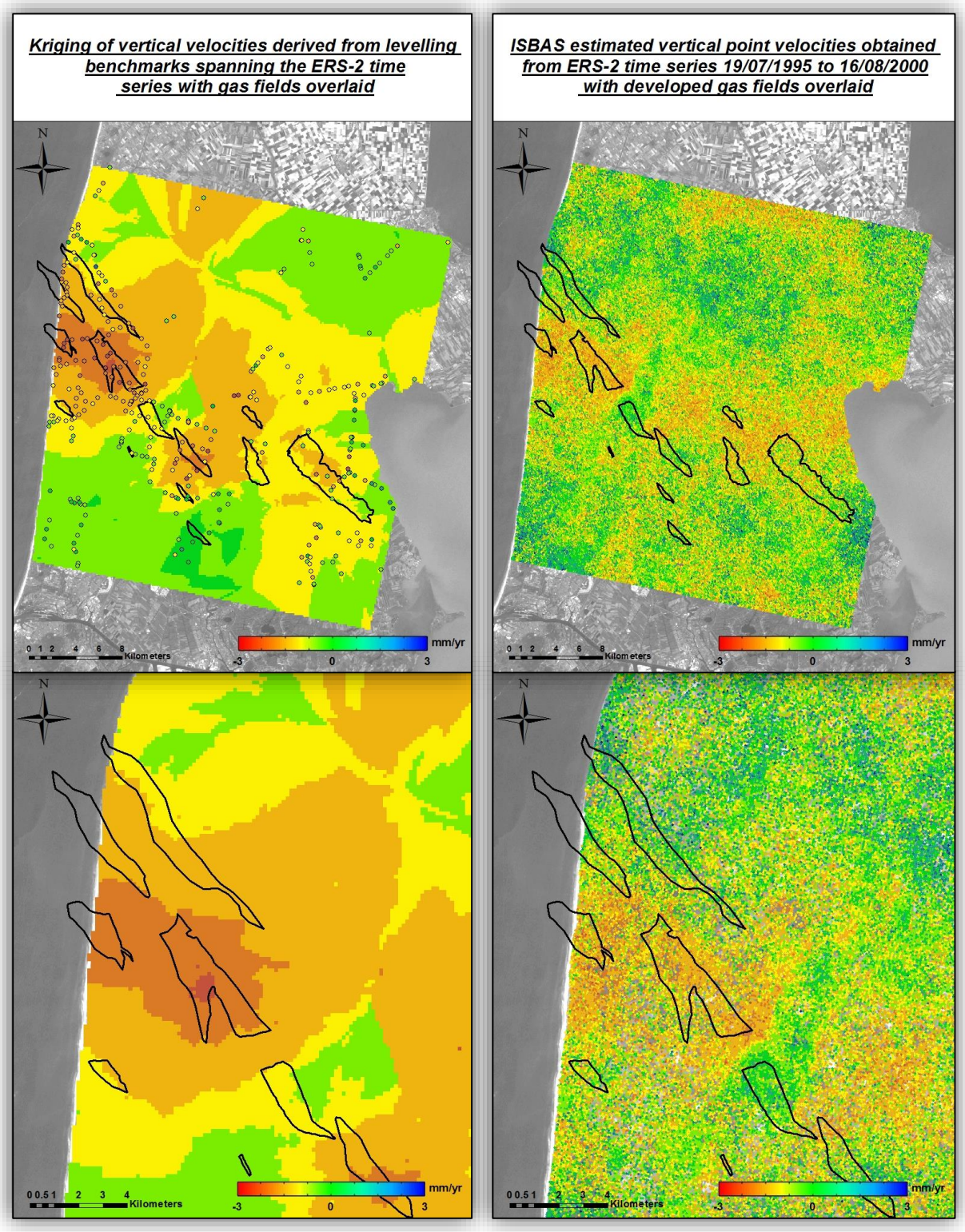


Figure 6.4: *A comparison of kriging produced from ERS levelling benchmarks (left) and the ERS-2 ISBAS analysis (right).*

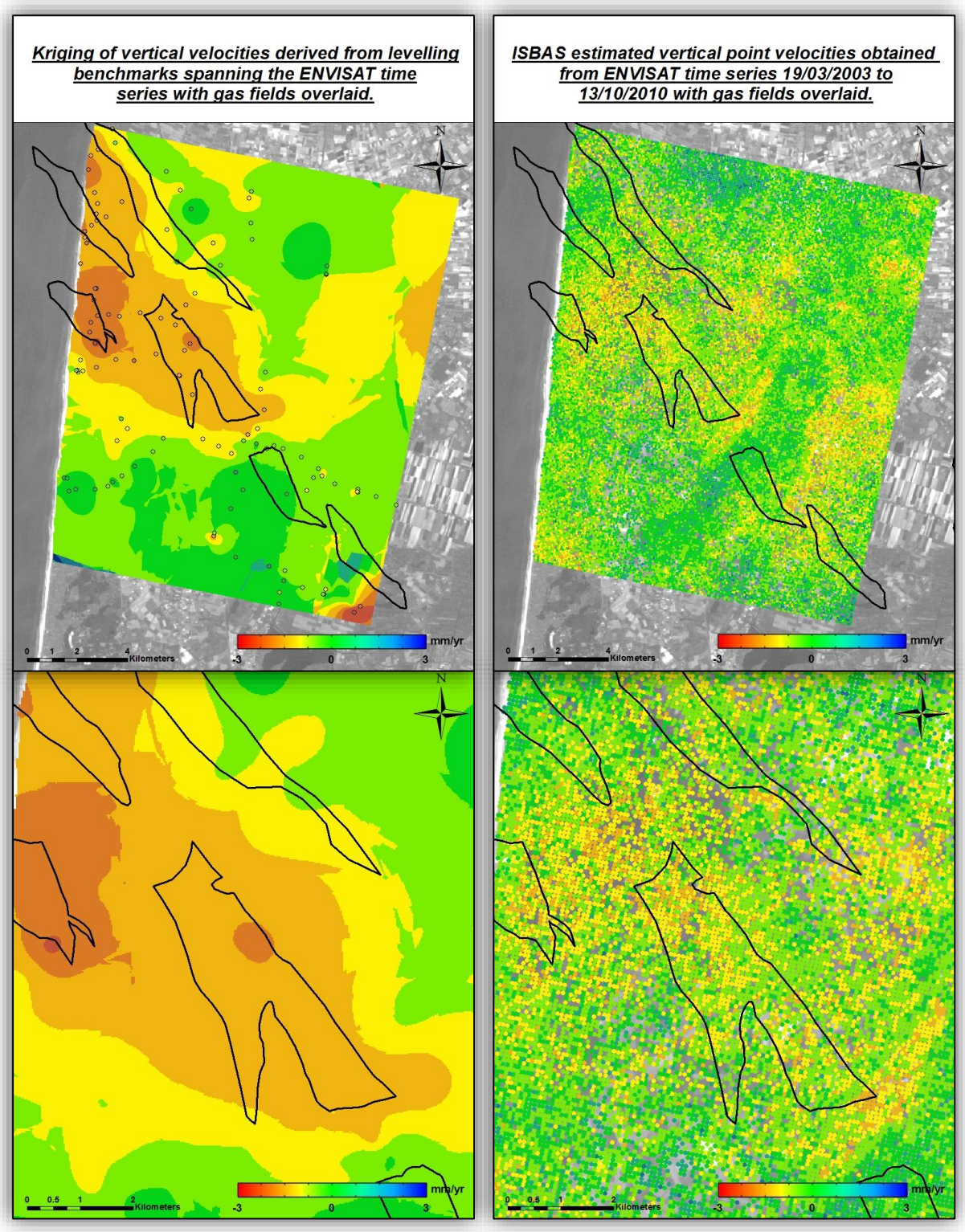


Figure 6.5: *A comparison of kriging produced from ENVISAT levelling benchmarks (left) and the ENVISAT ISBAS analysis (right).*

6.3 Measurement Validation - Linear Displacement Velocities

For a more quantitative analysis ISBAS and SBAS point velocities were directly compared to levelling measurements. At each benchmark, point velocities from the SAR products were selected within a 50 metres radius. If no point fell within 50 metres of the levelling benchmark it was discarded from the analysis, whereas if there was more than one point selected then only the nearest neighbour was retained for analysis. This left each remaining levelling benchmark with a corresponding SAR point velocity, where the differences between levelling and SAR estimates could be measured by calculating the Root Mean Square Error (RMSE). Gravimetric changes in the study are assumed to be negligible and therefore enabled levelling to be directly comparable with the ISBAS outputs because orthometric levelling data can be considered as geometric deformation.

6.3.1 ERS

291 locations fulfilled the criteria for ISBAS-levelling validation, with 36 locations for the SBAS-levelling validation. The RMSE of the ISBAS-levelling was 1.29 mm/year while the SBAS-levelling had a smaller error of 1.08 mm/year. The scatter plots of ISBAS and SBAS results show a lack of an elongated shape as might be expected, which implies low correlation between the measurements (Figure 6.6). However, the limited range on the axis of these plots reflects the relatively stable study site, with only a small area around Bergen found to be meaningfully subsiding.

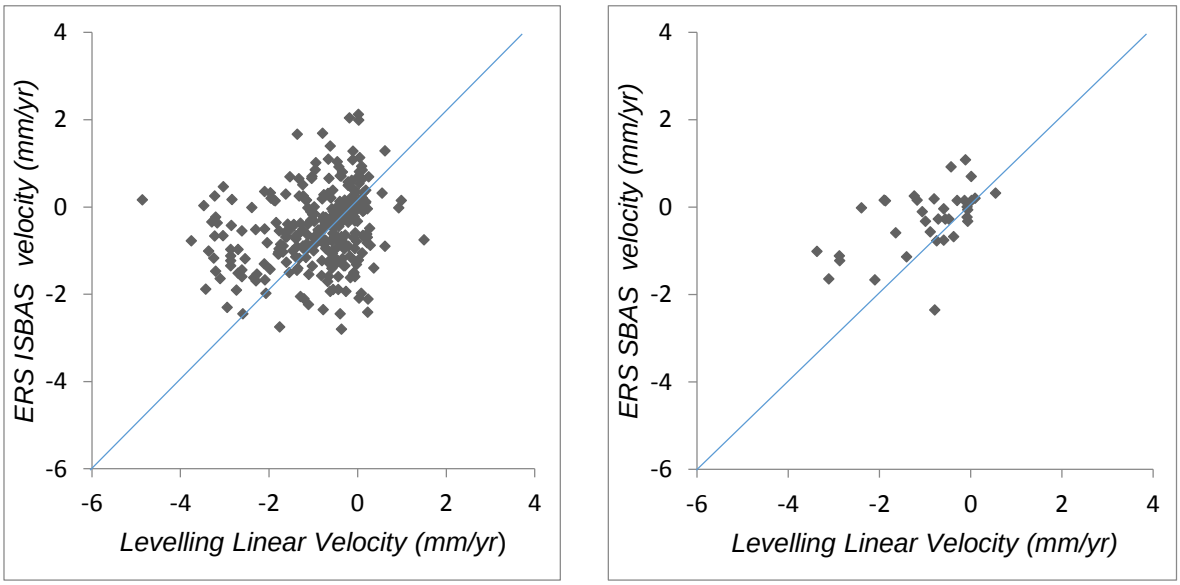


Figure 6.6: *(Left) Scatter plot of ERS ISBAS and levelling velocities. (Right) Scatter plot of ERS SBAS and levelling velocities.*

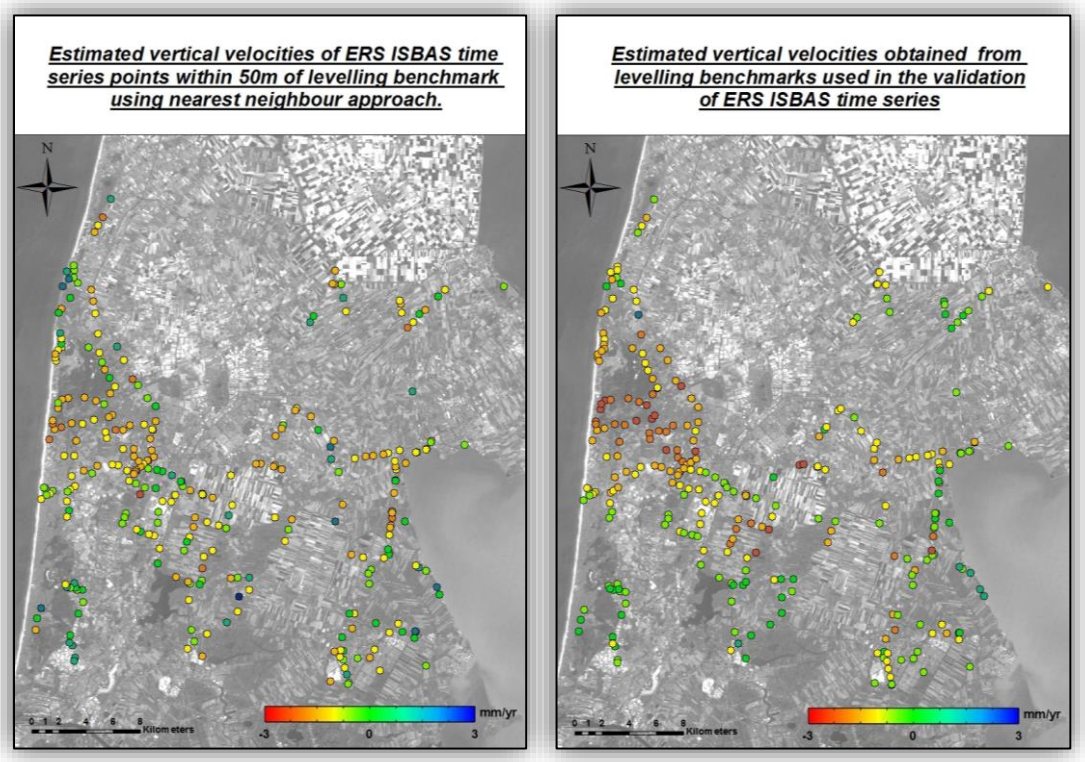


Figure 6.7: *(Left) ERS ISBAS linear displacement velocities (mm/yr) at levelling benchmark locations where nearest neighbour is available within 50m. (Right) Linear displacement velocities derived from levelling (mm/yr).*

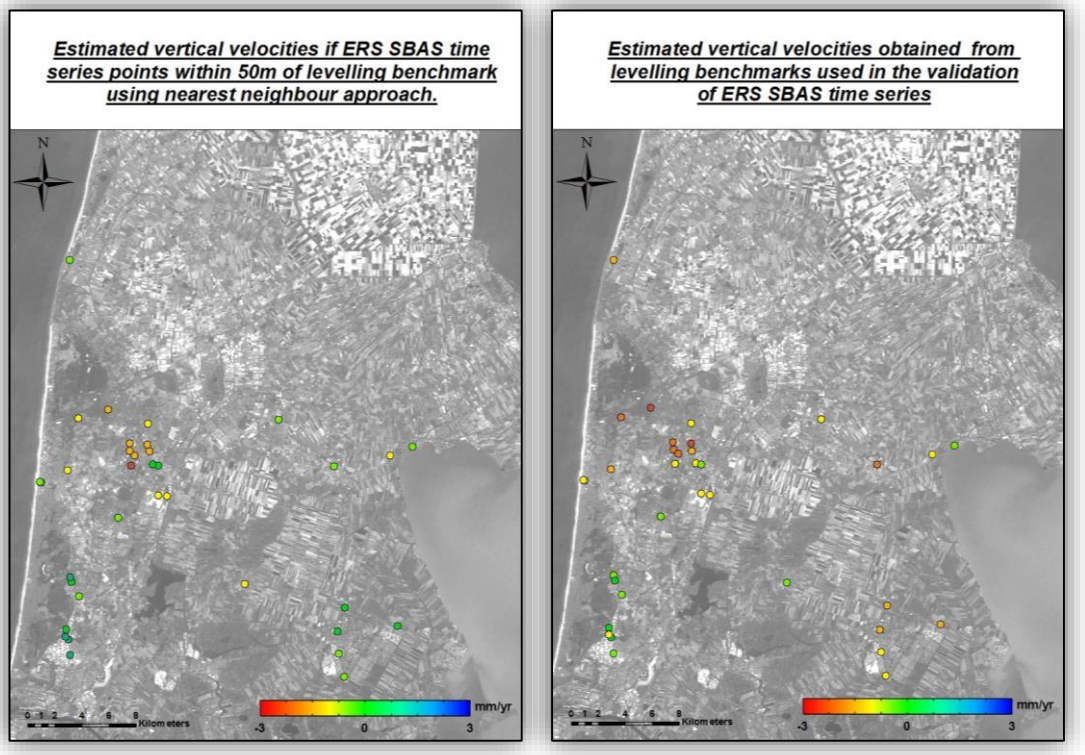


Figure 6.8: *(Left) ERS SBAS linear displacement velocities (mm/yr) at levelling benchmark locations where nearest neighbour is available within 50m. (Right) Linear displacement velocities derived from levelling (mm/yr).*

The plots indicate that there is an absence of a strong deformation signal over the study area due to the lack of an elongate pattern that might be expected; consequently, they should be interpreted as portraying the noise floor (the measure of the signal generated from the summation of all the unsolicited signals and noise sources within a measurement system) of SAR data products and levelling data. The SBAS scatter plot has a more elongated shape and suggests an underestimation of deformation from the SAR data. Figure 6.7 and 6.8 display the ERS linear displacement velocities at the levelling benchmark locations where the nearest neighbour is available within 50m, alongside the respective displacements from levelling for ISBAS and SBAS points respectively. The figures indicate the spatial pattern is more similar than the statistics would suggest.

6.3.2 ENVISAT

There were 116 locations that met the conditions for the ISBAS-levelling validation and 28 for the SBAS-levelling validation (less due to the reduced study site). Similarly to the ERS comparison the RMSE of the ISBAS-levelling was greater than the RMSE of the SBAS-levelling, producing differences of 1.42 mm/year and 1.00 mm/year respectively. The correlation between ENVISAT and levelling results can be seen in Figure 6.9. Similar conclusions from the ERS-levelling appraisal are maintained here, with a lack of a strong deformation signal leading to a low correlation and a potential underestimation from the SAR analysis. Figure 6.10 and 6.11 display the ENVISAT linear displacement velocities at the levelling benchmark locations where the nearest neighbour is available within 50m, alongside the respective displacements from benchmarks for ISBAS and SBAS points respectively. A summary of SAR-levelling comparisons is provided in Table 6.4.

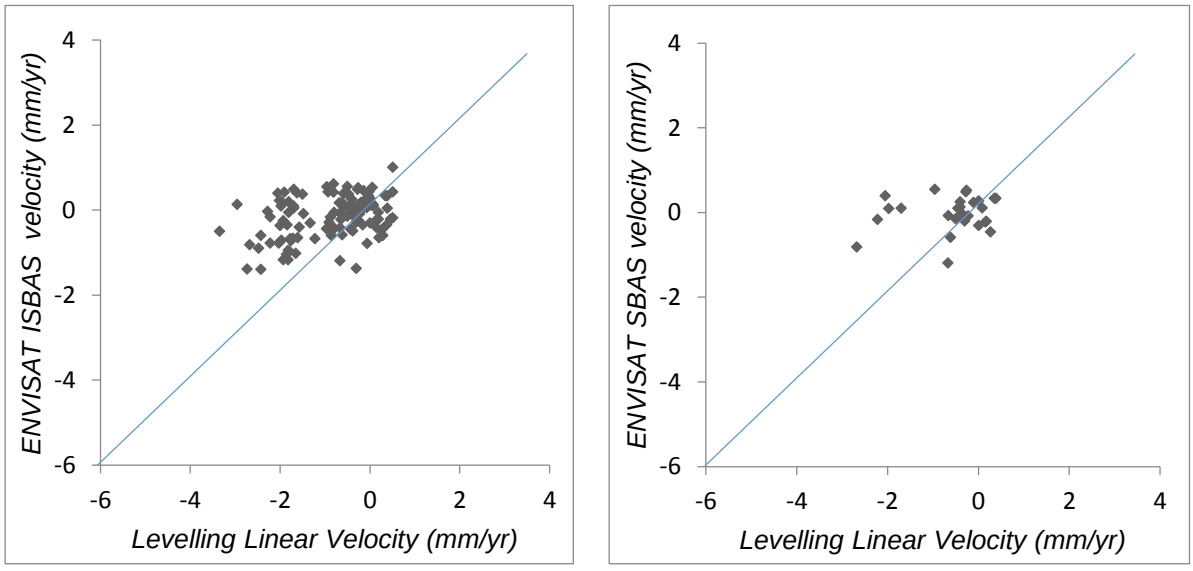


Figure 6.9: *(Left) Scatter plot of ENVISAT ISBAS and levelling velocities. (Right) Scatter plot of ENVISAT SBAS and levelling velocities.*

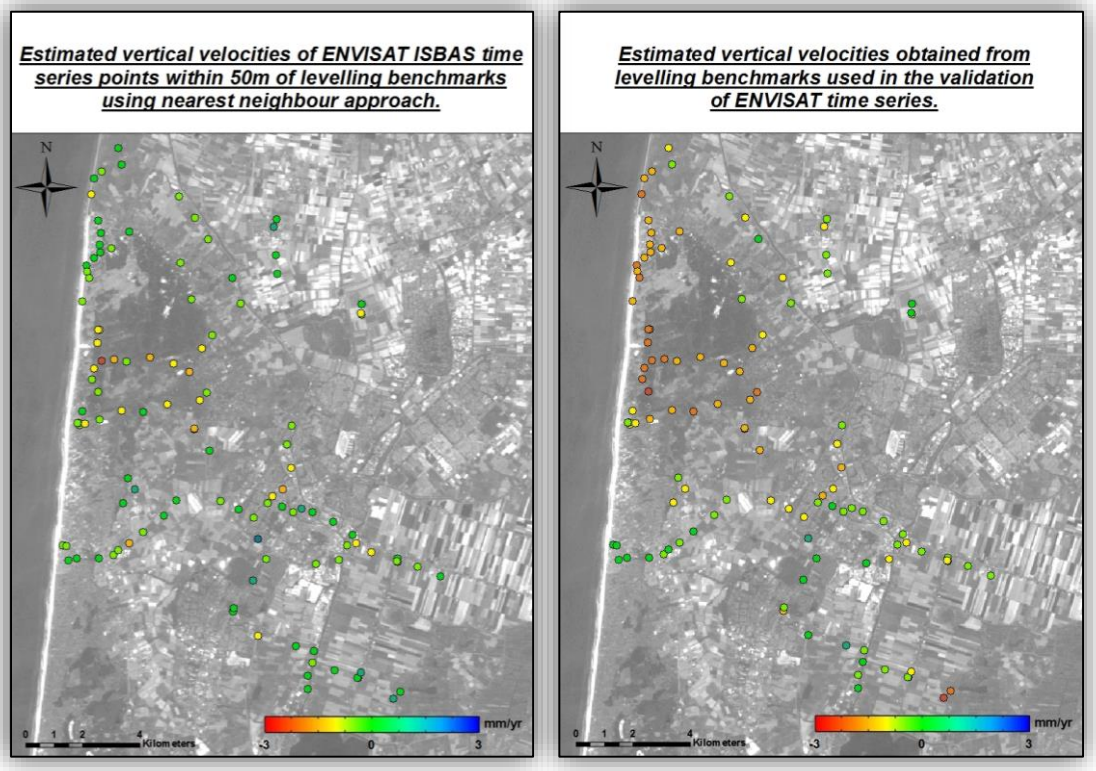


Figure 6.10: *(Left) ENVISAT ISBAS linear displacement velocities (mm/yr) at levelling benchmark locations where nearest neighbour is available within 50m. (Right) Linear displacement velocities derived from levelling (mm/yr).*

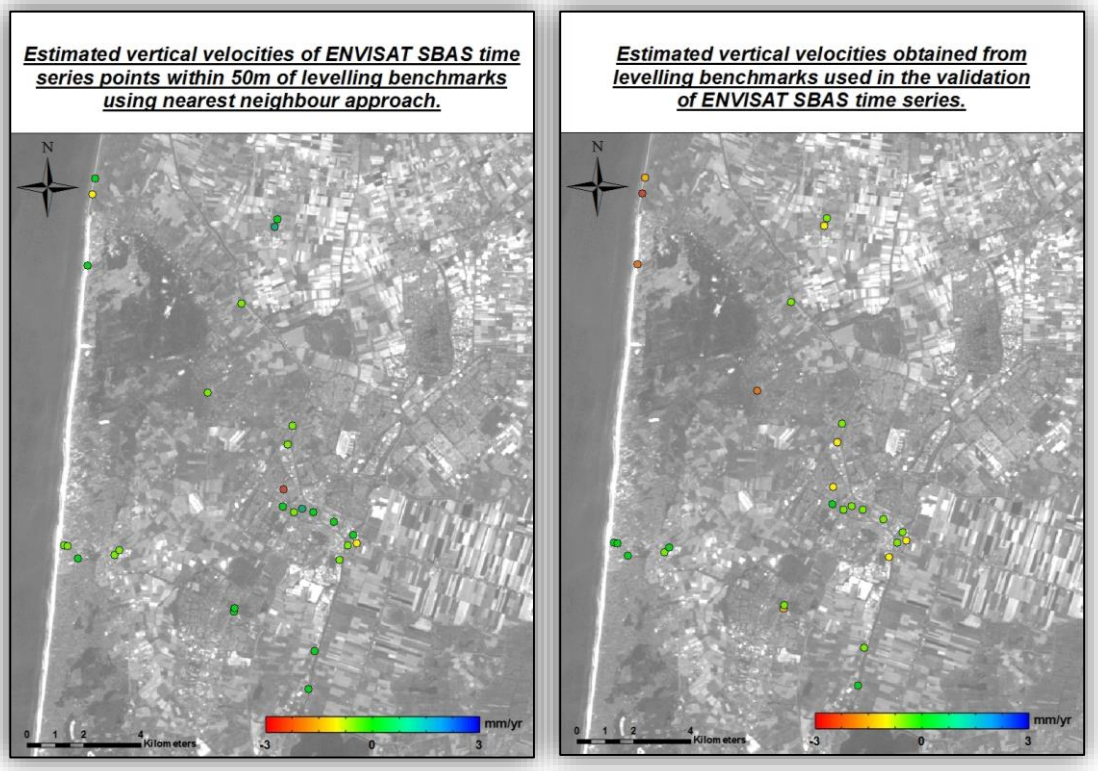


Figure 6.11: *(Left) ENVISAT SBAS linear displacement velocities (mm/yr) at levelling benchmark locations where nearest neighbour is available within 50m. (Right) Linear displacement velocities derived from levelling (mm/yr).*

	Number of Benchmarks	***Mean distance apart SAR-Levelling (m)***	***RMSE SAR-Levelling (mm/yr)***
ERS			
ISBAS	290	31.67	1.29
SBAS	36	30.96	1.08
ENVISAT			
ISBAS	116	30.88	1.42
SBAS	28	28.98	1.00

Table 6.4: *A summary of the RMSE between SAR and levelling data sets.*

6.3.3 Point Quality Correlations

As previously stated in Chapters 5.2.2 and 5.3.2 the predominant source of error is seen within targets exhibiting intermittent coherence, with a correlation between the standard deviation and number of coherent layers (m_{ij}). This is also indicated by the validation results, where the SBAS points proved to be 0.21 mm/year (ERS) and 0.42 mm/year (ENVISAT) more accurate than ISBAS points. This suggests a correlation between the quantity of coherent layers per point m_{ij} and the RMSE of the difference between ISBAS-levelling velocities. To analyse this, all the ISBAS points were divided into five relative categories based on m_{ij}, where the RMSE was subsequently calculated for these categories (Table 6.5).

Relative classification of coherent layers per point velocity	***Bottom 20%***	←	***Middle 20%***	→	***Top 20%***
ERS					
Number of coherent layers m_{ij}	120-176	177-232	233-288	289-344	345-399
RMSE	1.45	1.05	0.73	1.07	1.05
ENVISAT					
Number of coherent layers m_{ij}	250-349	350-449	450-549	550-649	650-750
RMSE	1.63	1.29	1.75*	1.33	0.99

Table 6.5: *RMSE between ISBAS-levelling based on coherent layers. *Only one point velocity in comparison.*

The category which produced the least error in the ERS comparison was surprisingly the middle category, while the biggest error was found in point velocities that had the fewest amount of coherent layers in their formation. The remaining three categories produced similar results. The ENVISAT comparison produced a stronger correlation, with least error found in the top category and greatest error found in the bottom category. A general correlation is seen in both the ERS and ENVISAT data sets, the more layers used in the calculation of point velocities the smaller the error with respect to levelling (Figure 6.12 & 6.13).

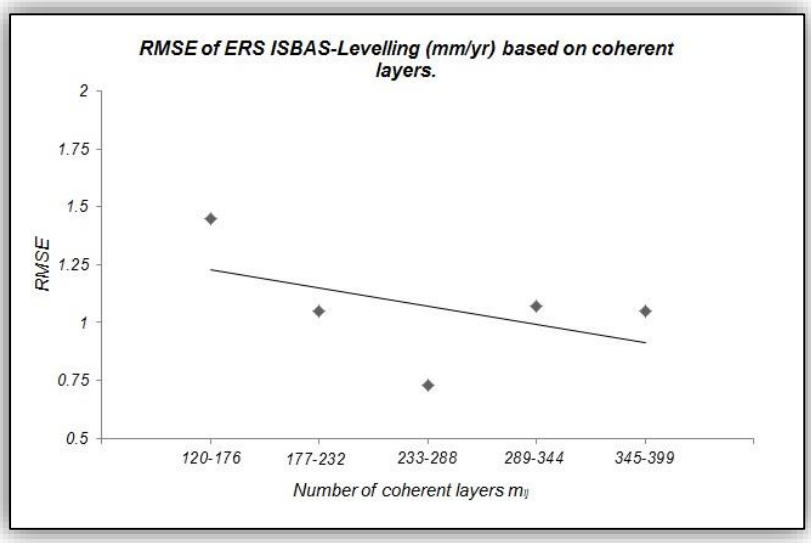


Figure 6.12: *Correlation between the quantity of coherent layers per point m_{ij} and the RMSE of the difference between SAR-levelling velocities for the ERS data set.*

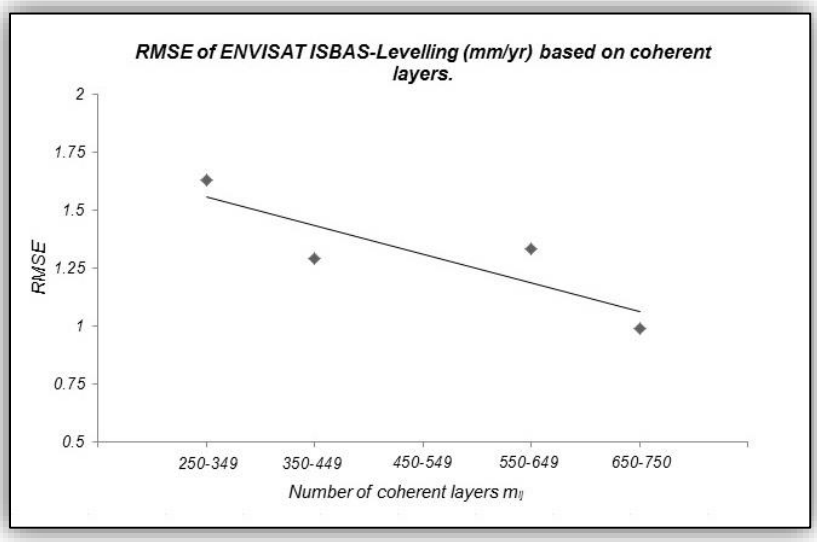


Figure 6.13: *Correlation between the quantity of coherent layers per point m_{ij} and the RMSE of the difference between SAR-levelling velocities for the ENVISAT data set. N.B. Category 450-549 excluded as only one comparison could be made.*

It has been documented that the points with the greatest quantity of coherent layers m_{ij} exist in urban locations. This is reflected by the strong correlation between the standard deviation and m_{ij} (Figure 5.6 & 5.11) and the percentage of SBAS point velocities that are located in urban land cover, 70% for ERS and 77% for ENVISAT. It would therefore suggest a correlation between land cover and the RMSE of the difference between ISBAS-levelling. The RMSE ISBAS-levelling was calculated for points falling in urban and non-urban (agriculture, woodland, sand and water). Differences in the ERS comparison are small; with urban land cover producing an RMSE of 1.18 mm/year and non-urban cover producing a slightly larger RMSE of 1.34 mm/year. The ENVISAT appraisal produced much bigger difference between the land covers. The error was 0.78 mm/year for urban land cover more than double for non-urban points, 1.63 mm/year (Table 6.6).

	Urban		***Non-Urban***	
	RMSE ISBAS-levelling (mm/yr)	***Number of points***	***RMSE ISBAS-levelling (mm/yr)***	***Number of points***
ERS	1.18	103	1.34	188
ENVISAT	0.78	36	1.63	80

Table 6.6: *Correlation between land cover and the RMSE of the difference between ISBAS-levelling.*

6.4 Comparisons with the Terrafirma Validation Project

The Terrafirma validation project compared unidentified PSI outputs from four Operational Service Providers and a result from TU Delft against levelling data for the Alkmaar site. There are some minor differences between the data used in this study and the TVP. For example the TVP used 76 ERS-1 and ERS-2 images in the first time series, whereas this study only utilized the ERS-2 imagery. Additionally, the TVP was conducted in 2007 and therefore imagery and levelling data beyond this point had not yet been acquired, whereas the ENVISAT time series extends to 2010 in this study. Cressetto *et al.* (2008) note that the validation of the ENVISAT time series had to be taken with caution due to the very limited levelling data available; this study has the benefit of levelling campaigns that were conducted up to 2012, which enabled a more reliable validation.

6.4.1 Subsidence Patterns

Both studies identified the same predominant pattern of subsidence to the West of Alkmaar. Figure 6.14 and 6.15 display the linear displacement velocities of two OSP's used in TVP (top left and right) alongside ISBAS (bottom left) and SBAS (bottom right) results for the ERS and ENVISAT time series respectively. The comparison verifies that the majority of the scene is stable and the overall spatial variation in subsidence is similar, with the area around the Bergermeer reservoir the only location to be meaningfully subsiding. In addition, comparing between the two data sets it is evident that OSP's also found greater levels of subsidence in the ERS data. The SBAS points are located in approximately the same locations as the PSI analyses, and are of a similar displacement velocity. They are both restricted to urban expanses, highlighting the ability of the ISBAS product to cover the majority of the scene and therefore reveal a more complete subsidence pattern.

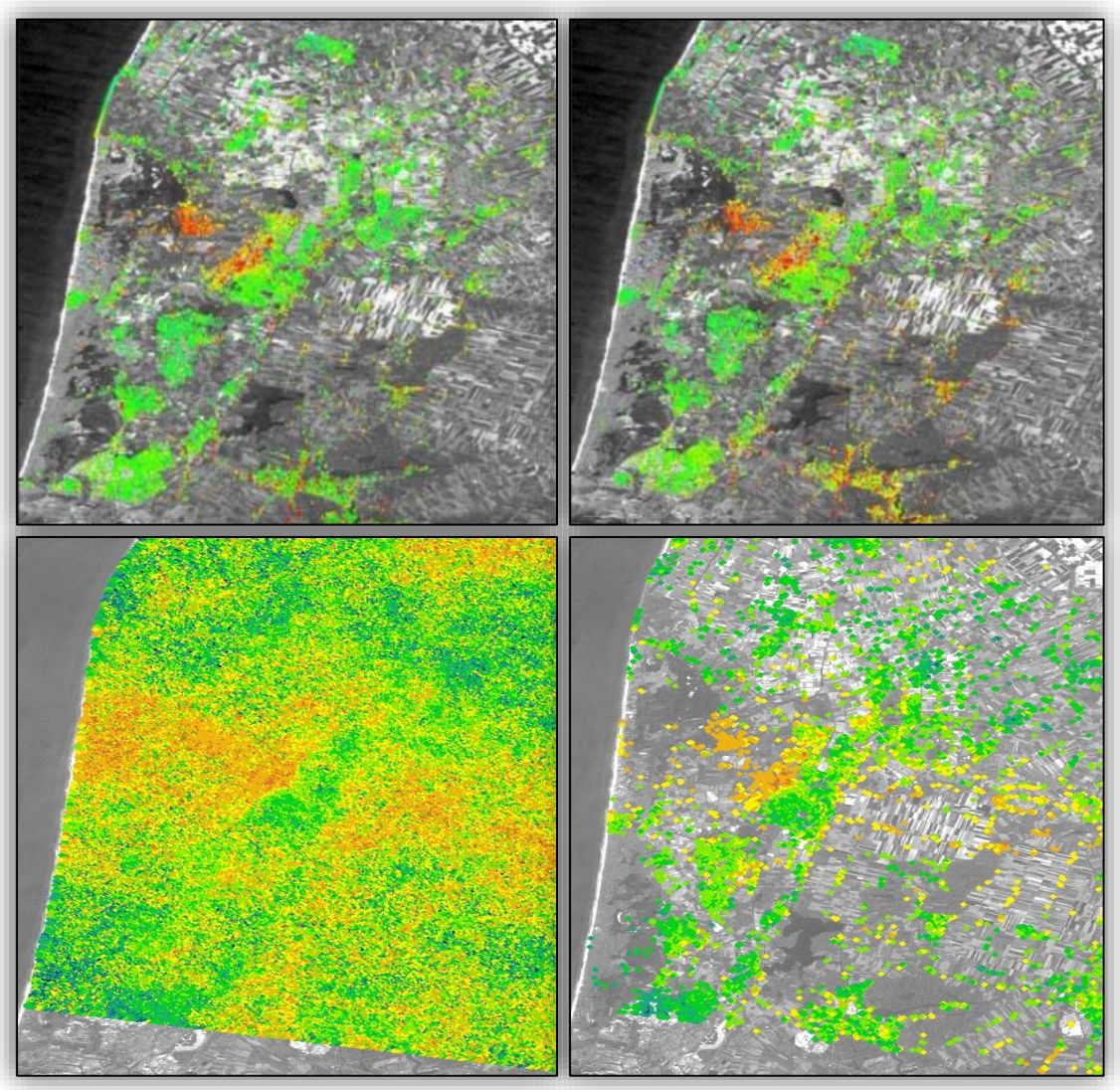


Figure 6.14: *(Top left) ERS PSI result from OSP C. (Top right) ERS PSI result from OSP D. (Bottom left) ERS ISBAS. (Bottom right) ERS SBAS.*

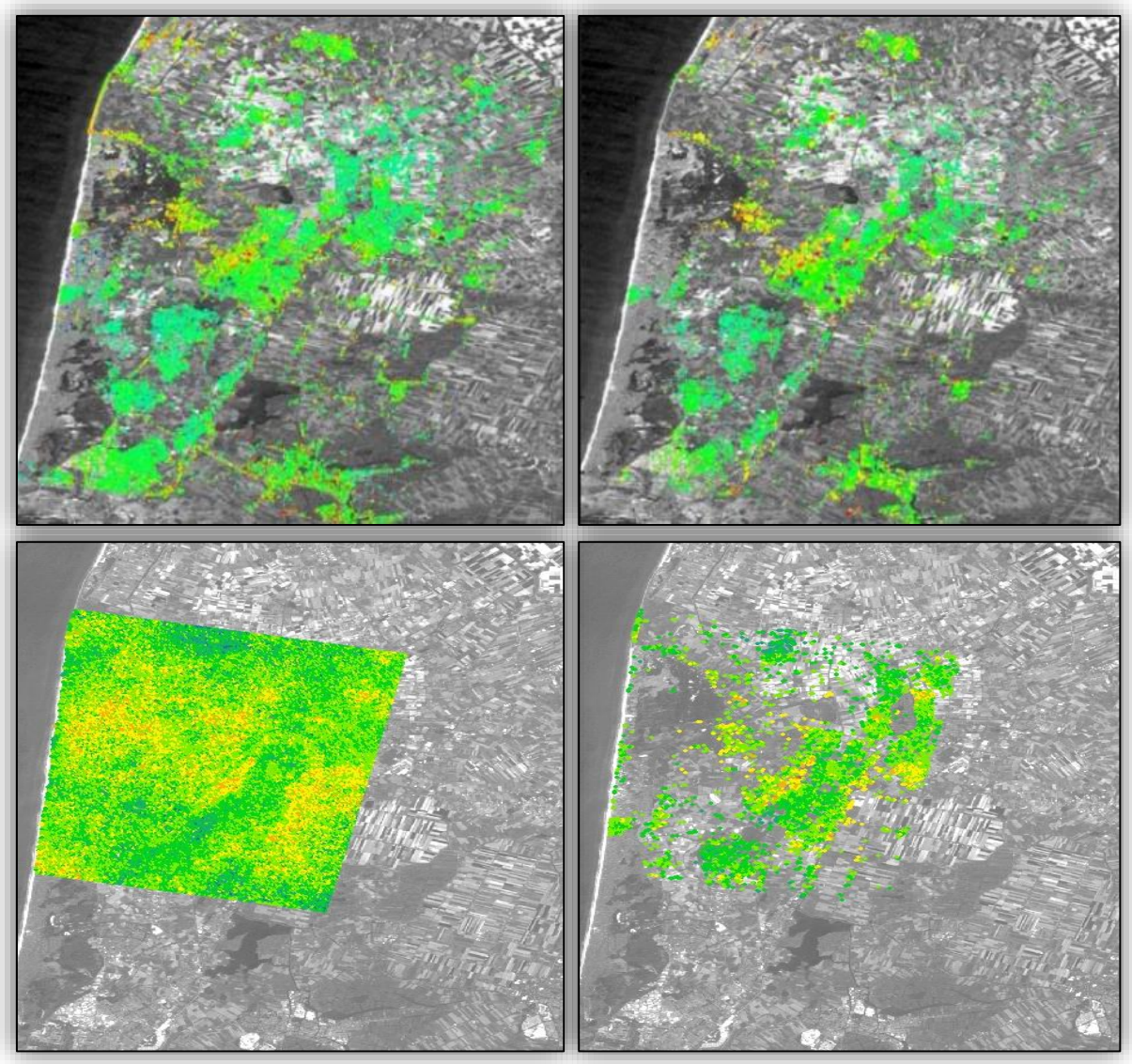


Figure 6.15: *(Top left) ENVISAT PSI result from OSP C. (Top right) ENVISAT PSI result from OSP D. (Bottom left) ENVISAT ISBAS. (Bottom right) ENVISAT SBAS.*

6.4.2 Linear Displacement Velocities

The ISBAS-levelling results ascertained are comparable to those found in the Terrafirma validation project (Crossetto *et al.,* 2008). The TVP concluded that the RMSE of the differences between PSI and levelling were between 1 – 1.5 mm/year for the ERS time series and 1.3 – 1.8 mm/year for ENVISAT. The results of this investigation are similar with RMSE of the difference between ISBAS and levelling being 1.29 mm/year for the ERS time series and 1.42 mm/year for the ENVISAT time series. These results are within the range achieved during the TVP with the significant benefit of an output that covered almost the complete scene. Table 6.7 exhibits a comparison of both sets of results.

	ISBAS	SBAS	TVP A	TVP B	TVP C	TVP D	TVP E
ERS							
No. of Benchmarks	290	36	36	151	58	58	47
RMSE SAR-Levelling (mm/yr)	1.29	1.08	1.07	1.54	1.04	1.23	1.18
ENVISAT							
No. of Benchmarks	116	28	76	118	80	49	90
RMSE SAR-Levelling (mm/yr)	1.42	1.00	1.51	1.79	1.63	1.26	1.54

Table 6.7: *A comparison of the RMSE of ISBAS/SBAS-Levelling (mm/year) and PSI-Levelling (mm/year) from five products used in the TVP.*

6.4.3 Displacement Time Series

An example of one ERS displacement time series is published in the TVP report, for the PS closest to Benchmark ID: 019A0115 (Figure 6.16). The time series published in the TVP shows discrepancy from the linear trend; it would be expected that points from the ISBAS analysis might display a greater discrepancy, as PS points are of a greater quality. ISBAS analysis is tuned for linear motion and therefore making a comparison with the time series from the TVP is not straightforward. Filtering is applied during the ISBAS non-linear analysis and therefore it is most useful to estimate atmospheric phase.

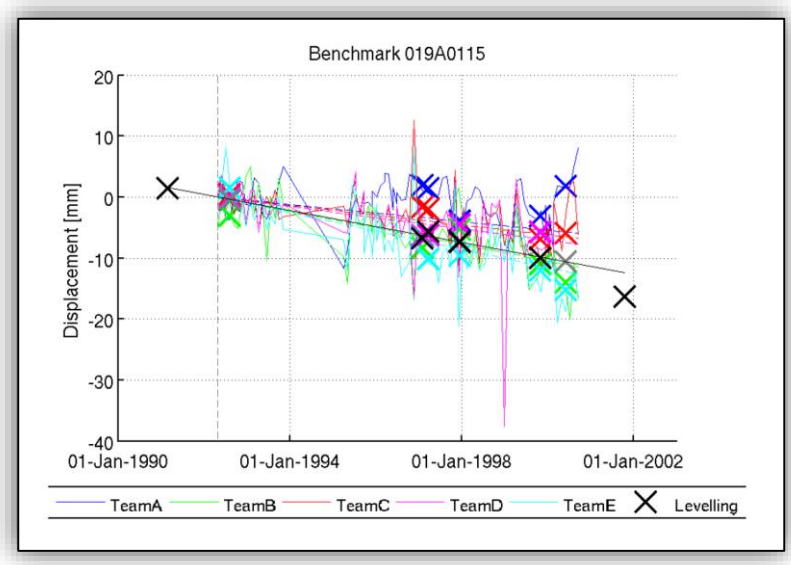


Figure 6.16: *ERS displacement time series published in TVP (Crossetto et al., 2008).*

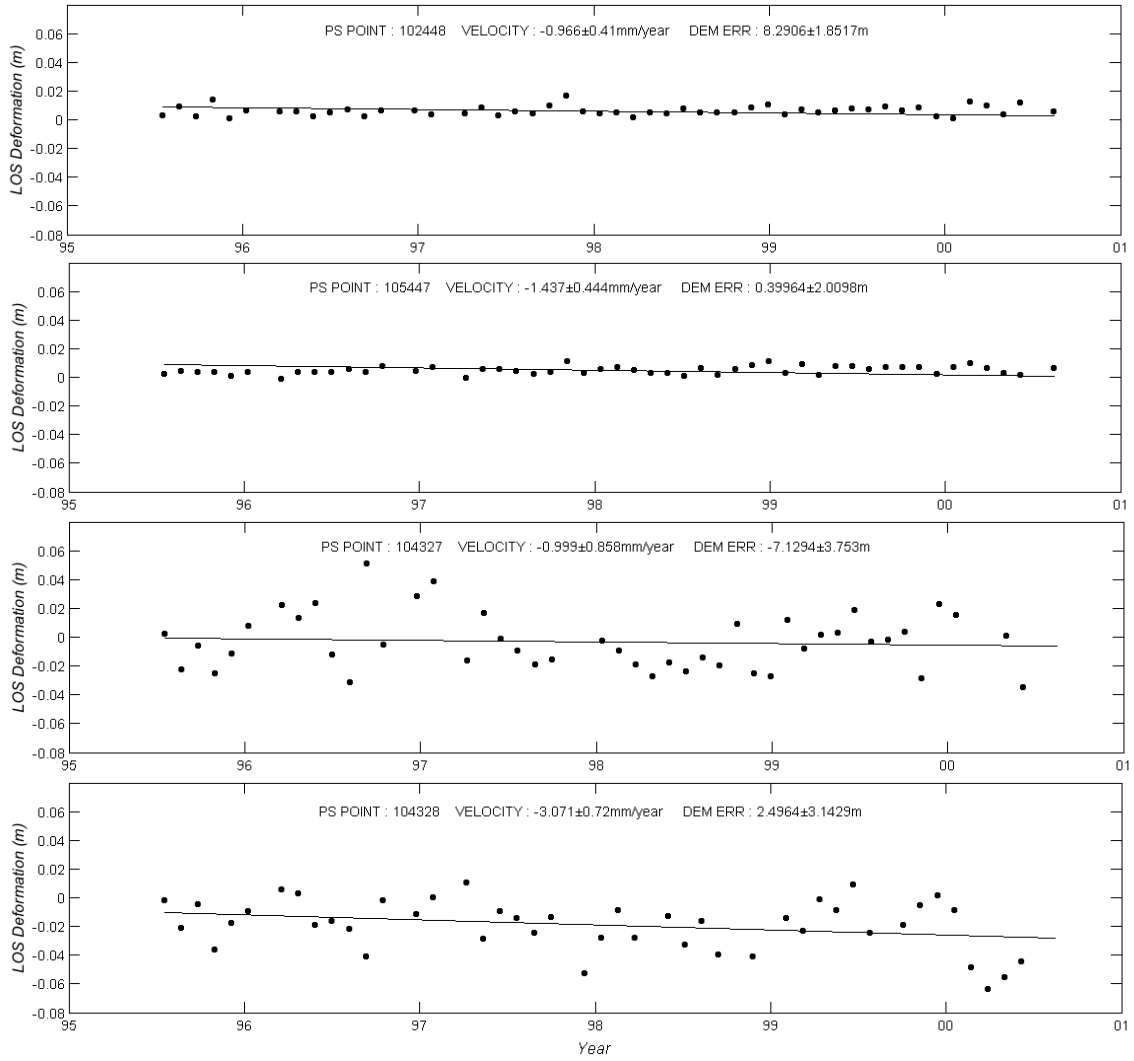


Figure 6.17: *ERS ISBAS time series for selected points near to benchmark 019A0115.*

While a non-linear analysis was performed for both the ERS and ENVISAT time series, results cannot be used for a direct comparison because filtering changes the results. At the location of benchmark 019A0115 there are a limited number of SBAS points; SBAS points produce the most reliable time series as they display coherence in every differential interferogram. If the SBAS point is surrounded by ISBAS points, when filtering is applied noise is introduced into the result. It is acknowledged that, if correctly weighted, adding more points improves the estimate; however, it would not be known whether adding more points of a lower quality would improve or degrade the result. The reduced variability of SBAS points is evident in Figure 6.17 which displays four time series in close proximity to benchmark 019A0115. The top two time series are SBAS points (ID: 102448 (m_{ij} = 399) and 105447 (m_{ij} = 399)), while the bottom two are ISBAS points (ID: 104327 (m_{ij} = 144) and 104328 (m_{ij} = 146)). SBAS points within the time series locate closer to the linear trend, whereas ISBAS points are more noisy, which is reflected in their greater standard deviation.

In addition, it has been previously observed that filtering can change the results depending on the filter being applied, therefore when any filter is applied there is an amount of ambiguity in the result (Sowter, 2016, pers. comm, April 2016).

6.5 Summary

ISBAS products have been validated with respect to levelling benchmarks, where an initial spatial comparison has confirmed the presence of a subsidence pattern to the West of Alkmaar. A validation of linear displacement velocities has shown that ISBAS products are comparable to levelling benchmarks, where the RMSE between data sets was found to be 1.29 mm/year and 1.42 mm/year for ERS and ENVISAT respectively. A negative correlation was found between the mij and RMSE, as mij increased the RMSE reduced. Targets that have intermittently coherent often situate in rural areas, as a consequence the quality of points is better in urban locations. The accuracy of ISBAS products are compared with results ascertained in the Terrafirma validation project. Results are found to concur, falling well within the error budgets of PSI products generated when previously studying the site by five other InSAR processing chains.

7 Discussion

7.1 DInSAR Performance

7.1.1 SBAS

The ground coverage of the SBAS point velocities was inhomogeneous and could only identify small isolated sections of deformation over the study site. They were most significantly identified over the Bergermeer reservoir, just to the West of Alkmaar. Subsidence was identified by some points located over the gas reservoir footprint and located in the town of Bergen, while points situated in Alkmaar were predominantly stable. This was most evident in the ERS time series, with the ENVISAT result proving to be more stable. However, due to the sparse point densities a clear pattern of deformation could not be formed. The SBAS technique, despite the spatial and temporal baseline constrictions, still suffers from some of the limitations associated with DInSAR technology. The densities of the coherent pixels are habitually inhomogenous, with the technique favouring urban areas where decorrelation is less prominent. 70% of the ERS and 77% of the ENVISAT point velocities were located in urban land cover. Coherence is highly dynamic in vegetated areas because fluctuations in soil moisture, land cover, meteorological conditions and agricultural activity all modify the physical characteristics of the surface (Ferretti *et al.,* 2003). As a consequence, the density of point velocities in rural areas is sparse, which inhibits the identification of ground motion patterns over differing land covers (Lanari *et al.,* 2007a).

7.1.2 ISBAS

In contrast, the ISBAS analysis covered almost the entire scene. It was most dense in urban regions but it also managed to extend over agricultural fields, forested areas, and sand dunes. The identification of subsidence around Alkmaar and Bergen was abetted by the increase in point density. This is best depicted in Figure 5.7 where almost the entire surface within the boundaries of the Bergermeer gas reservoir returned velocities, which are subsiding. Coherent points were achieved in the area between the Bergen, Groet and Bergermeer reservoirs which is covered by forest. Muntendam-Bos *et al.* (2008) note that the area which has experienced the most subsidence is above the Groet, Bergen and Bergermeer gas reservoirs. The ISBAS analysis corroborates this observation, something which the conventional SBAS analysis cannot achieve as point velocities in this area are inadequate. As previously mentioned coherence is highly dynamic in rural settings and often only preserved seasonally. Image pairs or subsets will remain coherent only for

short temporal epochs, intermittently coherent, not for the entire sequence of imagery. Consequently, although there may be highly coherent interferometric measurements within the SAR data stack, they are not considered in the standard SBAS algorithm. The ISBAS technique is optimized for such conditions, where there is a regular data set without large discontinuities in the temporal arrangement (Sowter *et al.,* 2013).

It has been previously demonstrated that the ISBAS algorithm can produce point dense deformation maps whilst achieving accurate ground motion rates. The ISBAS methodology has successfully been used over coal mining areas of the UK, showing significant improvements to the original SBAS technique. Sowter *et al.* (2013) displayed the technique's proficiency over the South Derbyshire and North West Leicestershire coalfields. Significant subsidence has been recognised over a wide region as a consequence of longwall mining extraction techniques. Subsidence has affected infrastructure and buildings, modified drainage patterns and altered surface topography. Over the predominantly rural land cover, ISBAS produced a widely distributed and denser network of velocity locations achieving 35032 point velocities compared with 5162 from SBAS. This covered almost the whole scene, densest in urban areas but also providing velocities over forest stands, agricultural fields and some water bodies. ISBAS velocities displayed a good spatial correlation with the coal measures, showing uplift. Similar outcomes were achieved by Bateson *et al.* (2015) who applied the ISBAS technique to the South Wales coalfield. Results mirrored that of Sowter *et al.* (2013) with the SBAS algorithm outputting 54815 coherent pixels, predominantly in the urban cities of Swansea, Cardiff and Newport. The ISBAS analysis returned 190161 coherent pixels extending the analysis into rural localities and as a result ISBAS covered 29% of the scene compared with the 8% achieved with a standard SBAS analysis. Large uplift to the North of Cardiff was newly identified and attributed to mine water rebound.

The ISBAS method has also been implemented in other application areas aside from mineral extraction. Cigna *et al.* (2014) conducted an ISBAS analysis to detect peat volume changes in North Wales. Over the predominantly rural land cover, conventional SBAS achieved only 4% coverage; implementing ISBAS a coverage of around 99% was achieved. By considering the intermittent coherence of rural scatterers the point density increased by a factor of 25. It was shown that the quality of ISBAS pixels were also of a good quality, with the standard deviation of points predominantly less than 1.0-1.5mm/year.

The results concur with conclusions found by Sowter *et al.* (2013), Bateson *et al.* (2015) and Cigna *et al.* (2014); the ISBAS algorithm is proficient in detecting surface motion over a variety of land covers. It has provided near complete coverage of the scene, extending over different land covers in a predominantly rural setting. The algorithm addresses the principle limitation of DInSAR, decorrelation. Noise effects on the interferograms are particularly problematic over rural environments, as the reflectivity of the land cover is not stable and can alter quickly. It has been shown that coverage can be achieved over these land covers using ISBAS which can assist in identifying subsidence patterns. The validation of ISBAS products has proved that the additional coverage does not come at the expense of accuracy, with error budgets comparable to PSI analysis in the most extensive validation undertaken to date for the Terrafirma project.

7.2 Limitations

7.2.1 SAR Data Continuity

As mentioned in Chapter 2.4.5.1 SAR, data availability can restrict interferometric analysis. There is a notable time gap between the ERS and ENVISAT data sets, 945 days. In this time period, seismic events in the Bergermeer and Bergen gas fields took place and therefore could not be directly analysed with either of the SAR data sets. It is established that these events were the result of gas extraction (Chapter 3.7), which caused further subsidence; however, they could not be directly observed in either the ERS or ENVISAT time series. This continuity gap is a significant weakness of SAR and it is hoped Sentinel-1 will prevent it reoccurring.

7.2.2 Reference Data

The measured movements of the benchmarks are adjudged to be an aggregate of movement caused by settlement, autonomous geological movement and movement triggered by hydrocarbon extraction. Autonomous geological movement in North Holland is a consequence of isostatic motion, tectonics and the compaction of deep seated clay layers. The summation of these processes produces regional subsidence of approximately -0.5 to -1 mm/year with regard to the average subsidence over the whole of the Netherlands. The first order system of benchmarks is established on Pleistocene sand deposits, approximately 30 metres below the surface, which forms the Dutch ordinance level. The vertical ground movement of these benchmarks can be seen in Figure 7.1.

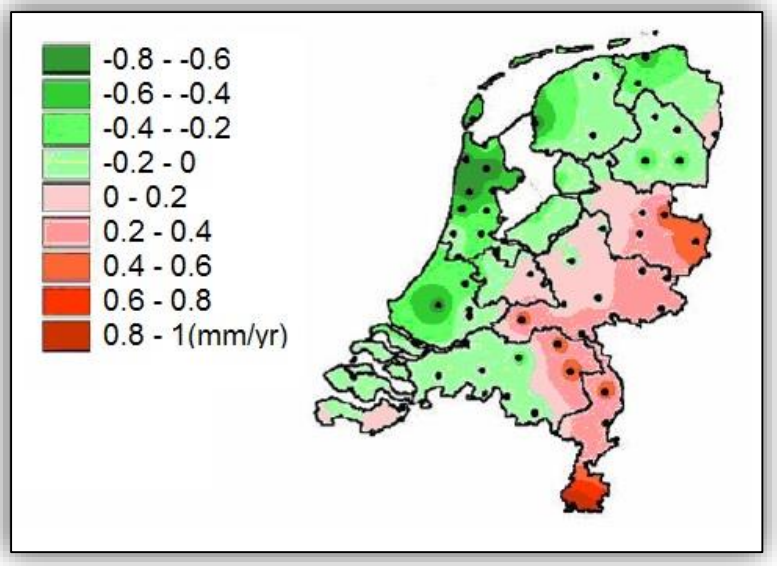


Figure 7.1: *Ground movement of the Netherlands, obtained from first order benchmarks (RWS-DID, 1997).*

Benchmark effects are anticipated to be present over substantial distances because levelling campaigns are closed on the Dutch ordinance level. However, over the relatively small scale of North Holland, these effects can be assumed to be slight, with a maximum difference of 0.2 mm/year across the province. This difference in velocity is predominantly attributed to shallow phenomena (i.e. the settlement of constructions where second order benchmarks have been situated) or gas production. Shallow phenomena are associated with the characteristics of the shallow geological deposits in the region; explicitly the region has a thick deposit of Fluvio-marine and Holocene marine material. With the exception of dune areas along the West coast, much of the province is prone to settlement, which is associated with the presence of peat and clay deposits, portrayed in Figure 7.2. Settlement will contribute to the total movement, to varying extents, depending on the foundation of the construction.

Precision information about levelling benchmarks is not available and therefore the quality can only be estimated. While the precision of the original levelling data is 0.7 mm/km^2, because the adjustment procedures and the network design are unknown it is not possible to reconstruct the variance-covariance matrix of the heights. Consequently, it is assumed that the levelling heights are uncorrelated with a standard deviation of 1 mm/year. Future work on the validation of ISBAS products would benefit from ground truth data of a greater accuracy, where a good quality description is available. In addition, ground truth that is more abundantly available in time and space wound also facilitate a superior validation.

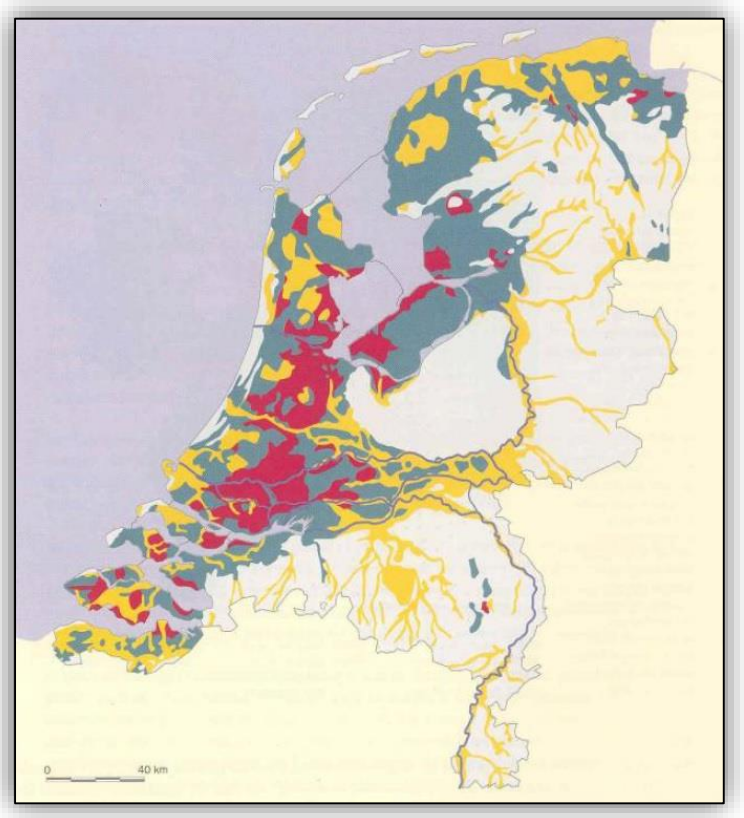


Figure 7.2: *The distribution of settlement prone locations in the Netherlands. Red areas are predominantly peat, green areas are predominantly clay and orange areas are predominantly sandy clay (Crosetto et al., 2008).*

7.2.3 Limited Deformation

The ISBAS validation has been limited to some extent by the lack of a strong deformation signal over the area. ISBAS products have been seen to be accurate with respect to levelling benchmarks, within error budgets of PSI products used in the TVP. Maximum subsidence rates were -4.48 ± 0.91 mm/year for the ERS time series and -2.57 ± 0.25 mm/year for the ENVISAT time series, in approximate agreement with other studies. However, a future validation would benefit from a greater deformation signal so error budgets found in this study could be scrutinized and compared. The results were found to be accurate to 1.29 mm/year and 1.42 mm/year for the ERS and ENVISAT time series respectively, which are small error budgets, even if there is a limited amount of deformation. Investigating an area that has higher rate of deformation would be valuable to see if the errors achieved here are comparable.

7.3 Recommendations for Further Research

7.3.1 Rural ISBAS Validation

The innovative ISBAS algorithm is still in its infancy and is therefore somewhat unproven and unverified. It has previously been validated with geology, aligning accurately with coal measures over the South Derbyshire and Leicestershire coalfields (Sowter *et al.,* 2013), Lancashire and Staffordshire coalfields (Novellino *et al.,* 2014a) and the South Wales coalfield (Bateson *et al.,* 2015). By the algorithms nature, results are difficult to verify, so further research is required into the validation of ISBAS products to corroborate the algorithm's proficiency. PSI techniques and other SBAS methods examine hard targets that are stable over time, such as urban areas and rocky expanses; validation data for these areas is relatively easy to acquire, for instance with continuous GPS measurements. ISBAS analyses extend into rural environments, over agricultural land and forest stands, where acquiring and recording validation data is much more challenging. Further work providing a rural validation would be useful, which could potentially lead to important results, consequently placing confidence in the technique's accuracy. This is somewhat related to the properties C-band SAR imagery. Explicitly, the utility of C-band SAR for monitoring forested expanses is supposed to be limited by the restricted transmittance of microwave energy through forest canopy. There are many constituents in rural environments that can add noise to the radar signal; for example, moisture effects and shrink swell. However, point velocities have been generated over forested areas, with deformation identified in these areas. A better understanding of how C-band radar interacts with rural surfaces would help to understand why results have been achieved in these locations and opens up some basic work on SAR signals that appears to be a research gap.

7.3.2 Sentinel-1 Time Series

The Sentinel-1 mission is poised to produce a wealth of radar data, optimised for delivering information for numerous services, including land subsidence monitoring. It is ideally suited and optimised for InSAR. Data over North Holland is relatively sparse because of the satellite mission's relative early stage, although in the coming years large data sets will be archived and made freely available by ESA. The repeat coverage is greatly increased with respect to the ERS and ENVISAT missions and due to be improved again with the launch of Sentinel-1B in 2016, when the two satellite constellation will be fully operational. Sentinel data is suited ISBAS analysis, as the shorter revisit times in tandem with the algorithms consideration of intermittent coherence will help to negate decorrelation and produce dense point velocities. When more images are available of the

province an ISBAS analysis will be achievable which will allow the continued monitoring of motion associated with gas production and further validation of ISBAS.

7.4 Summary

A discussion of the work in this thesis has been presented. The results of the SAR analysis are explored in relation to current published literature, with agreement found in the capabilities of ISBAS analysis to extend into rural environments. The discussion concludes by acknowledging the limitations of the study, which leads to suggestions for improvements and the identification of several new areas of research on SAR signals in rural settings, ISBAS validation and Sentinel-1 analysis.

8 Conclusions

8.1 Review of Aim and Objectives

As mentioned in Chapter 1.5 the aim of this investigation was to provide a quantitative validation the Intermittent SBAS algorithm. This was to be achieved by the following objectives:

- Identify a suitable study site that has been subjected to ground motion where SAR and validation data are available.
- Use Punnet to process data sets, computing linear velocity deformation maps.
- Compare the point densities of SBAS and ISBAS products.
- Validate ISBAS products with levelling benchmarks.
- Test conclusions and compare the results to published literature.
- Explore the limitations of the project and suggest areas for further research.

These objectives are now discussed to review what has been accomplished.

8.1.1 North Holland

North Holland was identified as an appropriate study site. ERS and ENVISAT SAR imagery were available, and validation data was obtainable in the form of levelling benchmarks. There is a history of natural gas production in the province, which has produced ground motion and induced seismic events in recent history. Furthermore, the province had previously been studied using PSI in a major validation project, Terrafirma, which provided a reference for ISBAS results. It is for these reasons North Holland was chosen.

8.1.2 ISBAS Analysis

Two data sets were successfully processed, an ERS-2 time series (1995-2000) and an ENVISAT time series (2003-2010); however not enough Sentinel-1 images are currently available for successful ISBAS analysis. The conclusions brought about by this research have shown that the ISBAS method is an effective solution in the identification of subsidence patterns over a variety of land covers. The SBAS analysis favoured urban land covers and was limited by decorrelation in non-urban areas; consequently it could only identify isolated sections of the subsidence pattern. The consideration of intermittent coherence in the ISBAS technique has crucially allowed the derivation of point velocities

in rural locations and therefore has extended the analysis so that near complete coverage of the study site could be achieved. It overcomes decorrelation and therefore has abetted the identification of the subsidence pattern over the entire region.

8.1.3 Product Validation

The overall conclusion from the comparison between ISBAS products and levelling is that they are similar. The measurement validation of linear velocities produced a RMSE of 1.29 mm/year and 1.42 mm/year for the ERS and ENVISAT time series respectively. The corresponding RMSE of SBAS points was 1.08 mm/year and 1.00 mm/year. The ISBAS analysis produced slightly larger differences with respect to levelling benchmarks than the SBAS points, but the accuracy was still high and, given the vastly denser distribution of point velocities, promising. It was also found that the RMSE was less for point velocities of a better quality (i.e. that had more coherent layers) and, related to this, the RMSE was less in urban land cover than rural land cover.

8.1.4 Comparisons with the Terrafirma Validation Project

The findings of this thesis are comparable to those found in the TVP. Subsidence patterns from PSI are similar to the SBAS points, but predominantly restricted to urban areas. The ISBAS products identify the same area of subsidence but returned point velocities at almost every location in the scene and hence revealed the overall pattern. The error budgets of ISBAS products (1.29 mm/year for ERS and 1.42 mm/year for ENVISAT) fall within the range of the error budgets achieved using PSI (1-1.5 mm/year for ERS and 1.3-1.8 mm/year for ENVISAT).

8.1.5 Limitations and Further Research

Future work in the validation of ISBAS products would benefit from precise information of levelling benchmarks, in addition to studying a site with a stronger deformation signal. Additional research is needed in the validation of ISBAS products to further substantiate the technique, especially in rural environments. Future validations could utilize the increasing amount of data that the Sentinel-1 mission is currently procuring.

8.2 Outlook

The production of natural gas is set to continue for some years as the global economy continues to expand and require energy for development. It is widely acknowledged that there is a need to move towards a more sustainable method of energy production, as

fossil fuels deplete and environmental awareness increases. Natural gas is a stepping stone in this process as we move towards hydrogen based energy production. As gas extraction continues there is an ever increasing need to monitor the effects it has on the surface and subsurface, made more significant as populations continue to rise and expand into non-urban areas. DInSAR techniques can assist in subsidence appraisals, efficiently monitoring wide areas over long periods. With the launch of new satellite missions, for example the Sentinel-1, radar satellite imagery will become ever increasingly available, with better coverage and less user restrictions, so new InSAR techniques are set to become more important. This thesis has contributed a quantitative validation for the ISBAS algorithm, proving that it can provide accurate deformation velocities over a variety of land covers, whilst also achieving unrivalled point densities. In future investigations using the algorithm, confidence can be placed in the results even where little or no ground truth is available.

8.3 Summary

A review of the work conducted in this thesis has been provided, re-examining the aim of the study by analysing the objectives set to achieve it. The levels to which the objectives have been achieved are stated and the thesis concludes by examining the implications ISBAS analyses has for subsidence monitoring and how the study has helped contribute to future research.

References

Askne, J. I., Dammert, P. B., Ulander, L. M., & Smith, G. (1997). C-band repeat-pass interferometric SAR observations of the forest. Geoscience and Remote Sensing, IEEE Transactions on, 35(1), 25-35.

Adamska, L. M. (2012). *Use of persistent scatterer interferometry for the enhancement of vertical land movement measurement at tide gauges around the British Coast* (Doctoral dissertation, University of Nottingham).

Allison, I.S., & Palmer. (1980). *Geology.* 7th Ed. New York: McGraw-Hill.

Bamler, R., & Hartl, P. (1998). Synthetic aperture radar interferometry. *Inverse problems*, *14*(4), R1.

Bateson, L., Cigna, F., Boon, D., & Sowter, A. (2015). The application of the Intermittent SBAS (ISBAS) InSAR method to the South Wales Coalfield, UK. International Journal of Applied Earth Observation and Geoinformation, 34, 249-257.

BBL. (2015). *Connecting Energy Markets.* [online] Available at:< http://www.bblcompany.com/> [Accessed 9th September 2015].

Berardino, P., Fornaro, G., Lanari, R., & Sansosti, E. (2002). A new algorithm for surface deformation monitoring based on small baseline differential SAR interferograms. Geoscience and Remote Sensing, IEEE Transactions on, 40(11), 2375-2383.

Biot, M. A. (1941). General theory of three-dimensional consolidation. Journal of applied physics, 12(2), 155-164.

Blanco-Sanchez, P., Mallorquí, J. J., Duque, S., & Monells, D. (2008). The coherent pixels technique (CPT): An advanced DInSAR technique for nonlinear deformation monitoring. Pure and Applied Geophysics, 165(6), 1167-1193.

Born, M., & Wolf, E. (1959). *Principles of optics: electromagnetic theory of propagation, interference and diffraction of light*. Cambridge university press.

Bremmer, C.N., Lange, G, Linden, W., Veling, E., & Veldkamp, J.G. (2003). Bodemdaling en integraal Waterbeheer: Eindrapport Delft Cluster Project 06.03.02. TNO-NITG report, 03-200-A.

Cao, L., Zhang, Y., He, J., Liu, G., Yue, H., Wang, R., & Ge, L. (2008). Coal mine land subsidence monitoring by using spaceborne insar data: A case study in fengfeng, hebei province, China. Int. Arch. Photogramm. Remote Sens. Spat. Inf. Sci, 37, 255-261.

Cascini, L., Fornaro, G., & Peduto, D. (2010). Advanced low-and full-resolution DInSAR map generation for slow-moving landslide analysis at different scales. Engineering Geology, 112(1), 29-42.

Casu, F. (2009). The Small BAseline Subset technique: performance assessment and new developments for surface deformation analysis of very extended areas (Doctoral dissertation, PhD thesis).

CGIAR-CSI. (2015). *SRTM 90m Digital Elevation Data.* [online] Available at:< http://srtm.csi.cgiar.org/index.asp> [Accessed 25th August 2015].

Chen, C. W., & Zebker, H. A. (2001). Two-dimensional phase unwrapping with use of statistical models for cost functions in nonlinear optimization. JOSA A, 18(2), 338-351.

Chilingarian, G. V., Sawabini, C. T., & Rieke III, H. H. (1983). Comparison between compressibilities of sands and clays. Journal of Sedimentary Research, 43(2).

Chisholm, M. (2015). *Subsidence in North Holland.* [image online] Available at:<http://idiotic-hat.blogspot.co.uk/2015/02/postcard-from-amsterdam-2.html> [Accessed 11th August 2015].

Cigna, F., Rawlins, B. G., Jordan, C. J., Sowter, A., & Evans, C. (2014). Intermittent Small Baseline Subset (ISBAS) InSAR of rural and vegetated terrain: a new method to monitor land motion applied to peatlands in Wales, UK. EGU General Assembly.

Circuit Design Inc. (n.d.). *Horizontally polarized waves / Vertically polarized waves.* [image online] Available at:<http://www.cdt21.com/parts/zu/zu_12.gif> [Accessed 20th April 2016].

Costantini, M., & Rosen, P. (1999). A generalized phase unwrapping approach for sparse data. In Geoscience and Remote Sensing Symposium, 1999. IGARSS'99 Proceedings. IEEE 1999 International (Vol. 1, pp. 267-269). IEEE.

Crosetto, M., Monserrat, O., & Agudo, M. (2008). Validation of existing processing chains in Terrafirma stage 2. Process Analysis Report, IG Inter-comparison, GMES TERRAFIRMA Project, ESRIN/Contract No. 19366/05/IE (Institute of Geomatica).

Curlander, J. C., & McDonough, R. N. (1991). *Synthetic aperture radar*. John Wiley & Sons.

Davies, R., Foulger, G., Bindley, A., & Styles, P. (2013). Induced seismicity and hydraulic fracturing for the recovery of hydrocarbons. Marine and Petroleum Geology, 45, 171-185.

Deltares. (2015). *Land subsidence dossier.* [pdf]. Deltares. Available at:< https://www.deltares.nl/app/uploads/2015/02/Dossier-Subsidence-Delta-Life-3.pdf> [Accessed 11th August 2015].

Deltawerken. (2004). *Geology of the Netherlands.* [online] Available at:< http://www.deltawerken.com/Geology-of-the-Netherlands/112.html> [Accessed 25th August 2015].

Del Ventisette, C., Ciampalini, A., Manunta, M., Calò, F., Paglia, L., Ardizzone, F., ... & Guzzetti, F. (2013). Exploitation of large archives of ERS and ENVISAT C-band SAR data to characterize ground deformations. Remote Sensing, 5(8), 3896-3917.

Ding, X. L., Li, Z. W., Zhu, J. J., Feng, G. C., & Long, J. P. (2008). Atmospheric effects on InSAR measurements and their mitigation. Sensors, 8(9), 5426-5448.

Discovery Center of Idaho. (2015). *Constructive and destructive interference*. [image online] Available at:< http://www.dcidaho.org/wp-content/uploads/2015/10/Fizzy-Ed-Resource-BWv31.pdf> [Accessed 4th March 2016].

Dost, B., Goutbeek, F., van Eck, T., & Kraaijpoel, D. (2012). Monitoring induced seismicity in the North of the Netherlands: status report 2010. KNMI Scientific report, 2012-03.

Duin, E. J. T., Doornenbal, J. C., Rijkers, R. H. B., Verbeek, J. W., & Wong, T. E. (2006). Subsurface structure of the Netherlands-results of recent onshore and offshore mapping. Netherlands Journal of Geosciences, 85(4), 245.

Economides, M. J., Demarchos, A. S., & Saputelli, L. (2002). Energy Sources and Energy Intensity for the Twenty-First Century. In SPE Annual Technical Conference and Exhibition. Society of Petroleum Engineers.

ESA. (2015a). *ASAR.* [online] Available at:< https://earth.esa.int/web/guest/missions/esa-operational-eo-missions/envisat/instruments/asar> [Accessed 11th August 2015].

ESA. (2015b). ERS-1 ERS-2. [online] Available at: <https://earth.esa.int/web/guest/missions/esa-operational-eo-missions/ers> [Accessed 11th August 2015].

ESA. (2015c). *Sentinel-1.* [online] Available at :< http://www.esa.int/Our_Activities/Observing_the_Earth/Copernicus/Sentinel-1/Facts_and_figures> [Accessed 11th August 2015].

Ferretti, A., Colesanti, C., Perissin, D., Prati, C., & Rocca, F. (2003). Evaluating the effect of the observation time on the distribution of SAR permanent scatterers. In Proc. Fringe (pp. 1-5).

Ferretti, A., Prati, C., & Rocca, F. (2000). Nonlinear subsidence rate estimation using permanent scatterers in differential SAR interferometry. Geoscience and Remote Sensing, IEEE transactions on, 38(5), 2202-2212.

Ferretti, A., Prati, C., & Rocca, F. (2001). Permanent scatterers in SAR interferometry. Geoscience and Remote Sensing, IEEE Transactions on, 39(1), 8-20.

Ferronato, M., Gambolati, G., Janna, C., & Teatini, P. (2010). Geomechanical issues of anthropogenic CO 2 sequestration in exploited gas fields. Energy Conversion and Management, 51(10), 1918-1928.

Franceschetti, G., & Lanari, R. (1999). *Synthetic aperture radar processing*. CRC press.

Gabriel, A. K., Goldstein, R. M., & Zebker, H. A. (1989). Mapping small elevation changes over large areas: differential radar interferometry. Journal of Geophysical Research: Solid Earth (1978–2012), 94(B7), 9183-9191.

Gatelli, F., Monti Guamieri, A., Parizzi, F., Pasquali, P., Prati, C., & Rocca, F. (1994). The wavenumber shift in SAR interferometry. Geoscience and Remote Sensing, IEEE Transactions on, 32(4), 855-865.

Ghiglia, D. C., & Pritt, M. D. (1998). Two-dimensional phase unwrapping: theory, algorithms, and software (Vol. 4). New York: Wiley.

GISwiki. (2015). *Synthetic Apreture radar (SAR).* [image online] Available at:< http://gis.wiki.fau.de/mediawiki/index.php/radar_mit_synthetischer_Apertur_(SAR)> [Accessed 11th August 2015].

Goldstein, R. M., & Werner, C. L. (1998). radar interferogram filtering for geophysical applications. Geophysical Research Letters, 25(21), 4035-4038.

Goldstein, R. M., Zebker, H., & Werner, C. L. (1988). Satellite radar interferometry- Two-dimensional phase unwrapping. Radio science, 23(4), 713-720.

Guo, B., & Ghalambor, A. (2014). Natural gas engineering handbook. Elsevier.

Haak, H.W., Dost, B., & Goutbeek, F.H. (2001). Seismic analysis of the earthquakes in Alkmaar on 9 and 10 September and Bergen aan Zee on October 10, 200. Royal Dutch Meteorological Institute.

Hager, B. H., & Toksöz, M. N. (2008). *Technical review of bergermeer seismicity study TNO report 2008-U-R1071/B 6 November 2008.* [pdf] Massachusetts Institute of Technology. Available at: <https://www.sodm.nl/sites/default/files/redactie/20091012briefTK_MITrapport.pdf> [Accessed 15th August 2015].

Hanssen, R. F. (2001). *Radar interferometry: data interpretation and error analysis* (Vol. 2). Springer Science & Business Media.

Hanssen, R., & Bamler, R. (1999). Evaluation of interpolation kernels for SAR interferometry. IEEE Transactions on Geoscience and Remote Sensing, 37(1), 318-321.

Hanssen, R., & Feijt, A. (1997). A first quantitative evaluation of atmospheric effects on SAR interferometry. In ERS SAR Interferometry (Vol. 406, p.277).

Hariharan, P. (2010). Basics of interferometry. Academic Press.

Hooper, A., Segall, P., & Zebker, H. (2007). Persistent scatterer interferometric synthetic aperture radar for crustal deformation analysis, with application to Volcán Alcedo, Galápagos. Journal of Geophysical Research: Solid Earth (1978–2012), 112(B7).

Hooper, A. (2008). A multi-temporal InSAR method incorporating both persistent scatterer and small baseline approaches. Geophysical Research Letters, 35(16).

JARS. (1999). *Relation between real aperture and synthetic aperture radar.* [image online] Available at:< http://wtlab.iis.u-tokyo.ac.jp/~wataru/lecture/rsgis/rsnote/cp4/4-3-1.gif> [Accessed 25th March 2015].

Just, D., & Bamler, R. (1994). Phase statistics of interferograms with applications to synthetic aperture radar. Applied optics, 33(20), 4361-4368.

Kampes, B. M., & Adam, N. (2006). The STUN algorithm for persistent scatterer interferometry. In Fringe 2005 Workshop (Vol. 610, p.16).

Lanari, R., Casu, F., Manzo, M., Zeni, G., Berardino, P., Manunta, M., & Pepe, A. (2007a). An overview of the small baseline subset algorithm: A DInSAR technique for surface deformation analysis. Pure and Applied Geophysics, 164(4), 637-661.

Lanari, R., Casu, F., Manzo, M., & Lundgren, P. (2007b). Application of the SBAS-DInSAR technique to fault creep: A case study of the Hayward fault, California. Remote Sensing of Environment, 109(1), 20-28.

Lee, J. S., Hoppel, K. W., Mango, S., & Miller, A. R. (1994). Intensity and phase statistics of multilook polarimetric and interferometric SAR imagery. Geoscience and Remote Sensing, IEEE Transactions on, 32(5), 1017-1028.

Leighton, J. M. (2010). GPS and PSI integration for monitoring urban land motion (Doctoral dissertation, University of Nottingham).

Lillesand, M. T., Kiefer, W. R., & Chipman, W. J. (2008). Digital Image Interpretation and Analysis. *Remote Sensing and Image Interpretation*, *6*, 545-81.

Lu, D., Mausel, P., Brondízio, E., & Moran, E. (2004). Change detection techniques. *International Journal of Remote Sensing*, 25(12), pp.2365-2401.

Lu, Z., Kwoun, O., & Rykhus, R. (2007). Interferometric synthetic aperture radar (InSAR): its past, present and future. *Photogrammetric engineering and remote sensing*, *73*(3), 217.

Lundgren, P., Usai, S., Sansosti, E., Lanari, R., Tesauro, M., Fornaro, G., & Berardino, P. (2001). Modelling surface deformation observed with synthetic aperture radar interferometry at Campi Flegrei caldera. Journal of Geophysical Research, 106 (B9), 2001.

Massonnet, D., & Feigl, K. L. (1998). radar interferometry and its application to changes in the Earth's surface. *Reviews of geophysics*, *36*(4), 441-500.

Massonnet, D., & Rabaute, T. (1993). radar interferometry: limits and potential. Geoscience and Remote Sensing, IEEE Transactions on, 31(2), 455-464.

Massonnet, D., Rossi, M., Carmona, C., Adragna, F., Peltzer, G., Feigl, K., & Rabaute, T. (1993). The displacement field of the Landers earthquake mapped by radar interferometry. Nature, 364(6433), 138-142.

Mather, P. M. (2004). *Computer processing of remotely sensed images: An introduction.* 3rd ed. Chichester: Wiley.

Mulders, F. M. M. (2003). Modelling of stress development and fault slip in and around a producing gas reservoir. TU Delft, Delft University of Technology.

Muntendam-Bos, A.G., Wassing, B.B.T., Geel, C.R., Louh, M., & van Thienen-Visser, K. (2008). *TNO report. Bergermeer Seismicity Study.* [pdf] Available at:<

http://www.gasopslagbergermeer.nl/wp-content/uploads/2015/06/pdf/mer/achtergronddocumenten/22.%20TNO%20Geo%202008,%20Geomechanisch%20onderzoek%20BGM%20veld,%2017-11-2008%20web.pdf> [Accessed 15th August 2015].

Nagel, N. B. (2001). Compaction and subsidence issues within the petroleum industry: From Wilmington to Ekofisk and beyond. Physics and Chemistry of the Earth, Part A: Solid Earth and Geodesy, 26(1), 3-14.

Natural Gas Europe. (2012). *Bergermeer Gas Storage Project Receives Approval.* [online] Available at:< http://www.naturalgaseurope.com/bergermeer-gas-storage-project-receives-approval-6196> [Accessed 9th September 2015].

NaturalGas.org. (2013). *Processing Natural Gas.* [online] Available at:< http://naturalgas.org/naturalgas/processing-ng/> [Accessed 15th August 2015].

Novellino, A., Athab, A. D., bin Che Amat, M. A., Syafiudin, M. F., Sowter, A., Marsh, S., ... & Bateson, L. (2014a). Intermittent SBAS Ground Motion Analysis in Low Seismicity Areas: Case Studies in the Lancashire and Staffordshire coal-fields, UK. Seismology from Space: Geodetic Observations and Early Warning of Earthquakes. Royal Astronomical Society, Burlington House, Piccadilly, London, UK.

NLOG. (2015). *Welcome to the NL Oil and Gas Portal.* [online] Available at:< http://www.nlog.nl/en/home/NLOGPortal.html> [Accessed 25th August 2015].

Noord Holland. (2015). *Province of Noord-Holland.* [online] Available at:< http://www.noord-holland.nl/web/English-3/English.htm> [Accessed 25th August 2015].

Novellino, A., Athab, A. D., bin Che Amat, M. A., Syafiudin, M. F., Sowter, A., Marsh, S., Cigna, F. & Bateson, L. (2014a). Intermittent SBAS Ground Motion Analysis in Low Seismicity Areas: Case Studies in the Lancashire and Staffordshire coal-fields, UK. Seismology from Space: Geodetic Observations and Early Warning of Earthquakes. Royal Astronomical Society, Burlington House, Piccadilly, London, UK.

Novellino, A., Cigna, F., Jordan, C., Sowter, A., & Calcaterra, D. (2014b). Monitoring large-scale landslides and their induced hazard with COSMO-SkyMed Intermittent SBAS (ISBAS): a case study in north-western Sicily, Italy. In EGU General Assembly Conference Abstracts (Vol. 16, p. 9621).

Pennington, W. D., Davis, S. D., Carlson, S. M., DuPree, J., & Ewing, T. E. (1986). The evolution of seismic barriers and asperities caused by the depressuring of fault planes in oil and gas fields of South Texas. Bulletin of the Seismological Society of America, 76(4), 939-948.

Plank, S. (2014). Rapid damage assessment by means of multi-temporal SAR. A comprehensive review and outlook to Sentinel-1. Remote Sensing, 6(6), 4870-4906.

Ramsey, E., Rangoonwala, A., & Bannister, T. (2013). Coastal Flood Inundation Monitoring with Satellite C-band and L-band Synthetic Aperture radar Data. JAWRA Journal of the American Water Resources Association, 49(6), 1239-1260.

Roest, J.P.A., & W. Kuilman. (1994). Geomechanical analysis of small earthquakes at Eleveld gas reservoir, Eurock '94, 573 – 580.

Rosen, P., Hensley, S., Joughin, I. R., Li, F. K., Madsen, S. N., Rodriguez, E., & Goldstein, R. M. (2000). Synthetic aperture radar interferometry. Proceedings of the IEEE, 88(3), 333-382.

RWS-DID. (1997). *Speed of vertical ground movements in mm / year.* [online] Available at:< http://www.kwaad.net/NAP-niveau.htm> [Accessed 9th September 2015].

Segall, P. (1985). Stress and subsidence resulting from subsurface fluid withdrawal in the epicentral region of the 1983 Coalinga earthquake. Journal of Geophysical Research: Solid Earth (1978–2012), 90(B8), 6801-6816.

Segall, P., & Fitzgerald, S.D. (1998). A note on induced stress changes in hydrocarbon and geothermal reservoirs, Tectonophysics, 289, 117–128.

Sowter, A., Bateson, L., Strange, P., Ambrose, K., & Syafiudin, M. F. (2013). DInSAR estimation of land motion using intermittent coherence with application to the South Derbyshire and Leicestershire coalfields. Remote Sensing Letters, 4(10), 979-987.

Staatsblad 542. (2002). *542. Law of October 31, 2002 , on rules concerning the investigation and the production of minerals and regarding with mining related activities (Mining Act).* [pdf] Available at:< http://www.eerstekamer.nl/behandeling/20021114/publicatie_wet> [Accessed 15th August 2015].

Statistics Netherlands. (2015). *Agriculture; crops, livestock and land use by general farm type, region.* [online] Available at:< http://statline.cbs.nl/Statweb/publication/?DM=SLEN&PA=80783eng&D1=2,4-5,18,28,33,45,81,118&D2=0-2,4&D3=1,12-13,15,20,23,26,34,44,46,49-53,63,65,132,135&D4=0,13-14&LA=EN&VW=T> [Accessed 25th August 2015].

Suckale, J. (2009). Induced seismicity in hydrocarbon fields. Advances in geophysics, 51, 55-106.

Sykes, L. R., & Sbar, M. L. (1973). Intraplate earthquakes, lithospheric stresses and the driving mechanism of plate tectonics. Nature, 245, 298-302.

Talwani, M., Feldman, W. K., & Schweitzer, M. (2002). U.S. Patent No. 6,467,543. Washington, DC: U.S. Patent and Trademark Office.

TAQA. (2014). *Gas Storage Bergermeer: Tomorrow's Energy. Today.* [video online] Available at:<https://www.youtube.com/watch?v=uqN8wbpx9yg> [Accessed 10th September 2015].

Teatini, P., Castelletto, N., Ferronato, M., Gambolati, G., Janna, C., Cairo, E., Marzorati, D., Colombo, D., Ferretti, A., Bagliani, A., & Bottazzi, F. (2011). Geomechanical response to seasonal gas storage in depleted reservoirs: A case study in the Po River basin, Italy. Journal of Geophysical Research: Earth Surface (2003–2012), 116(F2).

Terzaghi, K. (1923). The calculation of the durchlassigkeitsziffer tones from the course of hydrodynamic stress phenomena. Proceedings of the Academy of Sciences in Vienna, Mathematics and Natural Sciences Class, Division IIa , 132 , 125-138.

TNO. (2012). *Natural resources and geothermal energy in the Netherlands.* [pdf] TNO. Available at: <http://www.nlog.nl/resources/Jaarverslag2012/Delfstoffen_2012_UK_final_NLOG.pdf> [Accessed 11th August 2015].

University of Colorado Boulder. (2012). *The electromagnetic spectrum.* [image online] Available at:< http://lasp.colorado.edu/home/cassini/files/2012/12/Electromagnetic_Spectrum_noUVIS.jpg> [Accessed 25th March 2015].

U.S. Energy Information Administration. (2015). *Schematic geology of natural gas resources.* [image online]. Available at:< http://www.ucsusa.org/clean_energy/our-energy-choices/coal-and-other-fossil-fuels/shale-gas-unconventional-sources-natural-gas.html#.Vc9ieflViko> [Accessed 15th August 2015].

U.S. Geological Survey. (2013). *About USGS.* [online] Available at: < http://www.usgs.gov/aboutusgs/> [Accessed 8 May 2014].

Usai, S. (2000). An analysis of the interferometric characteristics of anthropogenic features. IEEE Transactions on Geoscience and Remote Sensing, 38 (3).

Usai, S. (2001). A New Approach for Long term Monitoring of Deformations by Differential SAR Interferometry. TU Delft, Delft University of Technology.

Van Eck, T., Goutbeek, F., Haak, H., & Dost, B. (2006). Seismic hazard due to small-magnitude, shallow-source, induced earthquakes in The Netherlands. Engineering Geology, 87(1), 105-121.

Van Lith, J. G. J. (1983). Gas Fields of Bergen Concession, The Netherlands. In Petroleum Geology of the South-eastern North Sea and the Adjacent Onshore Areas (pp. 63-74). Springer Netherlands.

Vos, D. D. (2010). Probabilistic Seismic Hazard Assessment for the Southern part of the Netherlands.

Washing, B., & Dost, B. (2012). *Seismic hazard of induced earthquakes. Integration of different studies.* [pdf] KNMI / TNO. Available at:< http://www.nlog.nl/resources/Seismic_Risk/TNO-KNMI_integratie-studie_2012_final.pdf> [Accessed 9th September 2015].

Werner, C., Wegmüller, U., Strozzi, T., & Wiesmann, A. (2003). Interferometric point target analysis for deformation mapping. In Geoscience and Remote Sensing Symposium, 2003. IGARSS'03. Proceedings. 2003 IEEE International (Vol. 7, pp. 4362-4364). IEEE.

Woodhouse, I. H. (2005). Introduction to microwave remote sensing. CRC press.

Zebker, H., & Villasenor, J. (1992). Decorrelation in interferometric radar echoes. Geoscience and Remote Sensing, IEEE Transactions on, 30(5), 950-959.

Zebker, H., Werner, C. L., Rosen, P., & Hensley, S. (1994). Accuracy of topographic maps derived from ERS-1 interferometric radar. Geoscience and Remote Sensing, IEEE Transactions on, 32(4), 823-836.

Zebker, H., Rosen, P., & Hensley, S. (1997). Atmospheric effects in interferometric synthetic aperture radar surface deformation and topographic maps. Journal of Geophysical Research: Solid Earth (1978–2012), 102(B4), 7547-7563.